Assessment of Adhesive Bonded Repairs

A thesis submitted in fulfilment of the requirements for the degree of Master of Engineering

Mildred Ching Ling Lee

B. Eng (Mechanical)

School of Aerospace, Mechanical and Manufacturing Engineering

College of Science, Engineering and Health

RMIT University

March 2013

Declaration

I certify that except where due acknowledgement has been made, the work is that of the author alone; the work has not been submitted previously, in whole or in part, to qualify for any other academic award; the content of the thesis is the result of work which has been carried out since the official commencement date of the approved research program; any editorial work, paid or unpaid, carried out by a third party is acknowledged; and, ethics procedures and guidelines have been followed.

Mildred Ching Ling Lee

1 March 2013

Acknowledgements

I take this opportunity to express my gratitude and thanks to Prof. C. H. Wang for taking a chance on my research capabilities and offering me the opportunity to undertake this project. I could not ask for a better supervisor who was always there to provide me with his expertise and wisdom to solve my (seemingly insurmountable) research problems. I would also like to thank Dr. Stefanie Feih who had always given me very helpful pointers on numerical analyses related issues and her critical review of my work. A big 'THANK YOU' to Ms. Eudora Yeo in DSTO (my unofficial supervisor), who had given me sound advice and suggestions on the bonding of my experimental joints and the provision of hands-on specimen bonding tutorials, materials and equipments.

I appreciate the funding from DGTA and am grateful to Dr. Madabhushi Janardhana for developing this research topic. I would also like to thank Dr. Alan Baker and Dr. Andrew Rider in DSTO for their invaluable suggestions for this project. I acknowledge the help from the technical staffs in DSTO and RMIT University in the manufacturing and testing of my specimens.

Lastly, I thank my family consisting of my sister, Ardo, Paul and my mother for their support, encouragement and assurance that it is not the end of the world when I was stuck in the ruts of research. Not forgetting my friends from the Sir Lawrence Wackett Aerospace Research Centre who has helped in some parts of my research and spent many '*Friday Nights*' entertainments with, thank you.

Abstract

Airworthiness certification of bonded repairs to aircraft primary structures remains unresolved due to the lack of non-destructive inspection techniques to detect weak bonds (manufacturing flaw or service-induced damage) or a potential deterioration in bond strength caused by environmental degradation from moisture ingress. An alternative approach to the direct detection of weak bonds is to develop a data-driven approach for certification of bonded repairs. Compliance to certification standards can be demonstrated if the probability of a bonded repair failing due to weak bond strength is found to be sufficiently low such that the reliability is not affected. The Adhesive Bonded Repair Assessment Program (ABRAP) was initiated to quantify the environmental durability of adhesive bonded repairs on retired aircraft parts using the Pneumatic Adhesion Tensile Testing Instrument (PATTI).

The aims of this research are to (i) interpret the shear strength of the bond from the measured flatwise tensile strength, (ii) to establish the causes for the variation in strength measurements and failure modes observed from the bonds tested and (iii) develop a predictive model to account for the effects of adherend thickness and taper on the pull-strength.

Adhesive bonded scarf and single lap-shear joints were used to verify the yielding behaviour of the FM300 adhesive resulting from pure cohesive, mixed cohesive-interfacial and purely interfacial failure modes. Three types of surface preparation techniques and two types of environmental conditioning were used to produce the different mode of failures. Finite element analyses of the scarf and lap-shear joints were conducted to determine the ratio of shear and tensile stress components affecting their failure. These experiments allowed the effects of the failure mode on the measured pull-off strength to be investigated.

Pull-tests were performed on a bonded panel whereby the edges of one of the adherend were milled to form a 3° taper. The purpose of this experiment is to generate the strength measurements for pull-tests performed on tapering and constant thickness sections. Numerical models of the pull-test configuration were constructed to evaluate the causes for the variation in strength and fracture mode from the aspect of the loading configuration. The adhesive layers of these models were assigned with two types of material models: an elastic-plastic stress-strain material model and cohesive elements.

The plastic yielding behaviour of the FM300 adhesive shows a strong sensitivity to hydrostatic pressure and can be described by the linear Drücker-Prager yield criterion. The shear strength of the joints can be inferred from the y-intercept of the yield curves and was found to be less susceptible to the effects of surface treatment and environmental degradation as the tensile strength. This means that a low pull-off strength does not necessarily indicate a low shear strength.

The application of small off-normal load to the pull-stub and the deflection of thin underlying substrate over which the PATTI pull-tests are performed both reduced the tensile pull-off strength.

Two predictive models were developed: the strain-based failure and the cohesive element approach. The use of the cap-plasticity material along with the maximum principal strain failure criterion at a characteristic distance gives accurate prediction for the strength of the joints and PATTI tests. When using cohesive elements, the best correlation with the experimental results is obtained through the use of a non-softening cohesive law.

Publications

The work in this thesis has been peer-reviewed and published through the following conference papers and journal:

1. M. Lee, E.Yeo, M. Janardhana, C.H. Wang, *'Effects of Off-Normal Loading on the Bond Strength Measurement of Bonded Repairs'* in the 28th International Congress of the Aeronautical Sciences, Brisbane, 2012
2. M. Lee, C.H. Wang, E. Yeo, M. Janardhana, '*Effects of Adherend Thickness on the Bond Strength Measurement of Adhesive Bonded Repairs*' in the 7th Australasian Congress on Applied Mechanics, Adelaide, 2012.

   (This paper has been awarded 3rd Place for the Postgraduate Student Best Paper Award)
3. M. Lee, E. Yeo, C.H. Wang, '*Influence of Adherend Deformation on Adhesive Bond Strength Measured by Portable Pull-Off Tests*', International Journal of Adhesion and Adhesives, 44 (2013) 259-268.

Table of Content

Declaration I

Acknowledgements II

Abstract III

Publications V

Table of Content VI

List of Figures X

List of Tables XVI

1 Introduction 1

1.1 Background 1

1.1.1 Motivation for Research 1

1.2 Gaps in Available Knowledge 5

1.2.1 Inferring Shear Strength from Pull-Off Strength 5

1.2.2 Variation in Fracture Modes 6

1.2.2.1 Inadequate Surface Preparation 6

1.2.2.2 Bond Degradation 6

1.2.3 Loading Configuration 7

1.3 Aims 8

1.4 Methodology 9

1.4.1 Inferring the Shear Strength of the Bond 9

1.4.2 Effects of Bond Degradation on Pull-Off Strength 11

1.4.3 Effects of Loading Configuration on Pull-Off Strength 12

1.5 Thesis Outline 13

2 Literature Review 15

2.1 Yielding behaviour of the adhesive 15

2.2 Influence of Surface Preparation Methods 17
2.3 Influence of Environmental Degradation 18
2.4 Failure Criteria for Strength Prediction 21
2.5 Numerical Analyses with Cohesive Models 22

3 Experiments 24
3.1 Scarf Joint Experiment 25
3.1.1 Pristine (Dry) Conditions 25
3.1.2 Hot/Wet Conditioning 28
3.2 Tapered Edge Panel Experiments 31
3.3 Fracture Toughness Measurements 34
3.3.1 Mode I – Double Cantilever Beam 34
3.3.2 Mode II – End Notched Flexural Test 35

4 Results 37
4.1 Scarf Joint Results 37
4.1.1 Pristine (Dry) Conditions 37
4.1.2 Hot and Wet Conditions 46
4.2 Tapered Edge Panel PATTI Results 51
4.3 Fracture Toughness Measurements 53
4.3.1 Mode I Fracture Toughness 53
4.3.2 Mode II Fracture Toughness 54

5 Finite Element Modelling 55
5.1 3D Scarf Joint Models 56
5.1.1 Geometry and Meshing 56
5.1.2 Single Lap-Shear Joint Model 61
5.1.3 Elastic Stress Analysis 63
5.2 Axisymmetric Tensile Butt Joint Models 69
5.3 Uniform Panel Models 71
5.4 Tapered Edge Panel Models 75

6 Constitutive Materials for the Adhesive 77
6.1 Von Mises Material 77

6.2 Linear Drücker-Prager Yield Criterion 80
6.2.1 Pristine (Dry) Condition Joints 81
6.2.2 Hot and Wet Conditioned Joints 82
6.2.3 Influence of Surface Preparation and Environmental Conditioning on Joint Strength 83
6.2.4 Modified Drücker-Prager / Cap Plasticity Material 85
6.3 Summary of Material Models 89

7 Bond Strength Prediction 90
7.1 Failure Criterion 91
7.2 Prediction with the von Mises Yield Criterion 93
7.2.1 Calibration of Characteristic Length 93
7.2.2 Panel Strength Prediction 95
7.3 Prediction with the Cap Plasticity material 96
7.3.1 Calibration of Characteristic Length 96
7.3.2 Scarf Joint Strength Prediction 98
7.3.2.1 Effects of Off-Normal Loading on Pull-Strength 100
7.3.3 Panel Strength Prediction 102
7.3.3.1 Effects of Adherend Thickness and Taper on the Pull-Strength 106

8 Cohesive Element Model 114
8.1 Cohesive Element Formulation 114
8.1.1 Linear Damage Evolution 114
8.1.2 Non-Linear Damage Evolution 120
8.2 Panel Strength Prediction 125
8.2.1 Linear Damage Evolution Profile 125
8.2.2 Non-Linear Damage Evolution Profile 128

9 Discussion 135
9.1 Predicting Pull-Strength for Panels with Non-Optimum Bond 135
9.2 Generating Interfacial Fracture Modes 137
9.3 Comparison between using the Cap Plasticity material and the Cohesive Models 138

10 Conclusion 143

References 145

Appendix I – DSTO Gritblast Silane Process for Aluminium Substrates 151

Appendix II – Alternative Surface Preparation Techniques for Aluminium Substrates (Methods B and C) 152

Appendix III – Curing Procedures for Bonded Joints 154

Appendix IV – Example of Tabular Data in ABAQUS CAE 155

List of Figures

Figure 1-1: PATTI test configuration as used a) to test the adhesion of surface coatings and b) to obtain the residual flatwise tensile strength of bonded repairs on retired aircraft structures 3

Figure 1-2: Off-normal loading caused by over-shimming. 8

Figure 3-1: Joints with scarf angles of 0°, 15°, 30°, 60° and 75°. 26

Figure 3-2: Fixture to align and maintain contact of scarf joints during curing 28

Figure 3-3: Dual-staged Fickian diffusion curve fitting for FM300 adhesive discs. 29

Figure 3-4: Estimating moisture saturation level within bonded joints 30

Figure 3-5: PATTI test configuration on bonded panels. 32

Figure 3-6: a) Partial plan view from the non-tapered side of the bonded panels showing the layout of the circular grooves cut through the panel and the adhesive layer. b) Cross sectional view showing a typical circular groove cut through the non-tapered side of the bonded panel. 32

Figure 3-7: Test configuration of the ENF specimens 35

Figure 4-1a: Typical fracture surfaces of the 0° scarf joints 38

Figure 4-2: Failure mode of dry scarf and lap-shear joints and percentage voids on fracture surfaces. 42

Figure 4-3: Effective fracture strength of scarf and single lap-shear joints after applying the void correction method 44

Figure 4-4a: Typical fracture surfaces of the conditioned 0° and 15° scarf joints 46

Figure 4-5: Failure mode of conditioned scarf and lap-shear joints and percentage voids on fracture surfaces. 49

Figure 4-6: Comparison between the fracture strength of conditioned (wet) and dry joints with a) surface preparation Method A and b) surface preparation Method C. 50

Figure 4-7: Nominal pull-off strength across different underlying panel thickness..... 52

Figure 4-8: Typical fracture surfaces on the stub-side and panel side of the (a) 3.0 mm uniform section and (b) 1.7 mm (c) 1.3 mm (d) 0.7mm tapered sections of the bonded tapered..... 52

Figure 5-1: Cross sectional mesh for the tensile butt joint 57

Figure 5-2: Three-dimensional model of the tensile butt joint. (The adhesive layer is represented by the blue section in between) 58

Figure 5-3: Vertical cross-sectional view of the a) 15° and b) 60° scarf joint models..... 59

Figure 5-4: The origins for the maximum and minimum radial lengths of the elements due to scaling of the circular mesh in Figure 5-1 to the major diameters formed by the ellipses of each scarf angle 60

Figure 5-5: Boundary conditions applied to the a) single lap-shear model and b) thick adherend lap-shear model 62

Figure 5-6: Stress distribution within the tensile butt joint where *r* represents the radial stresses and *Theta* represents the circumferential stresses in the cylindrical coordinate system 63

Figure 5-7**:** Orientation of stress vectors within adhesive of scarf joints. 65

Figure 5-8: Normalised von Mises and hydrostatic stress components versus scarf angle..... 67

Figure 5-9: Stress gradient of the edge and central regions at the midlayer of the adhesive for different scarf angle 68

Figure 5-10: Typical axisymmetrical model for the tensile butt joint with three different meshing at the radial edge region of the adhesive layers..... 70

Figure 5-11: Typical radial slice model of the pull-test configuration with uniform underlying panel thickness 71

Figure 5-12: Typical uniform model with refined mesh at the edge of the adhesive for analyses with the von Mises material 72

Figure 5-13: Typical uniform panel model with a layer of Hysol adhesive between the "Test-Disc" and "Pull-Stub" section..... 74

Figure 5-14: Typical uniform panel model with a 0.2 mm overcut 75

Figure 5-15: Typical three-dimensional model of the halved PATTI test configuration with finer mesh at the edge of the stub's adhesive and variation in underlying substrate thickness..... 75

Figure 6-1: Equivalent von Mises data converted from the Cytec datasheet [56] and the scaled values to match the experiments. 77

Figure 6-2: 'Corrected' linear Drücker-Prager fit for dry joints. 81

Figure 6-3: Linear Drücker-Prager fit for conditioned joints. 83

Figure 6-4: Linear Drücker-Prager plots of all the scarf and lap-shear joints 84

Figure 6-5: Yield surfaces of the FM®300 adhesive specified by ABAQUS 6.10 Modified Drücker-Prager/Cap model in the deviatoric-hydrostatic plane. 87

Figure 7-1: Comparison of the behaviour of the critical element in each mesh. 95

Figure 7-2: Plot of the experimental pull-off strength and the prediction by the uniform panel FE models with von Mises material versus the underlying panel thickness. 96

Figure 7-3: Predicted strength for the scarf and single lap-shear joints using the modified Drücker-Prager/Cap Plasticity material. 98

Figure 7-4: Plot of shear yield strength of joints after removing off-normal loading effect 102

Figure 7-5: Plot of experimental and FE prediction of the PATTI pull-off strength versus the underlying panel thickness and their reduction from the fracture strength of the tensile butt joint. 103

Figure 7-6: Strain distribution within the adhesive layer modelled with the modified Drücker-Prager/Cap Plasticity material for a) 0.7 mm b) 1.3 mm c) 1.7 mm and d) 3.0 mm uniform panels at failure. 104

Figure 7-7: Maximum principal stress distribution across the adhesive when modelled through the modified Drücker-Prager/cap plasticity material 105

Figure 7-8: Supported and unsupported areas of the bonded panel during pull-tests. 106

Figure 7-9: View of the PATTI test during loading showing the deflection and the strain distribution causing mixed cohesive-interfacial failure at the thin underlying panel section. 107

Figure 7-10: View of the PATTI test during loading showing the deflection and the strain distribution causing cohesive failure at the thick underlying panel section. 108

Figure 7-11: Strain distribution of the adhesive layer at the lower interface of the a) 0.7 mm and b) 1.7 mm tapered models 109

Figure 7-12: Comparison between the difference in deflection at the *'thin'* and *'thick'* regions for the a) 0.7 mm and b) 1.7 mm tapered edge panel. (Deformation in figures have been scaled by 10× for ease of visualisation) 110

Figure 7-13: Scaling parameter, *k* for different panel thickness 112

Figure 7-14: Comparison of calculated shear strengths for different panel thicknesses with adhesive shear strength. 113

Figure 8-1: Typical loading behaviour of a cohesive element (*i=I, II, III; denotes the loading modes in pure normal, 2nd shear and 3rd shear respectively)* 115

Figure 8-2: Constitutive response of a cohesive element under mixed-mode loading 117

Figure 8-3: Elliptical curve describing the quadratic stress failure criterion for damage initiation 118

Figure 8-4: Comparison of damage evolution profiles produced by varying *n* 121

Figure 8-5: Graphical representation of the mixed-mode ratio ϕ_1 and ϕ_2 122

Figure 8-6: Maintaining G_C and calculating the effective displacement for all order of *n* 123

Figure 8-7: Strength prediction from uniform panel FE models with linear degradation cohesive elements 126

Figure 8-8: Length of damage zone at failure for a) 0.7 mm b) 1.33 mm c) 1.7 mm and d) 3.0 mm panel thickness 127

Figure 8-9: Stress gradient along radius of the model for each panel thickness 128

Figure 8-10: Strength predictions for uniform panel models using cohesive elements with non-linear damage evolution profiles 129

Figure 8-11: Variation in predicted strength for each panel thickness 130

Figure 8-12: Variation in damage zone length for each panel thickness 130

Figure 8-13: Comparison of stress gradient across the radius of cohesive elements with $n = 0.1$ and $n = 3$ for the 0.7 mm model 131

Figure 8-14: Effects of a) $n = 0.1$ and b) $n = 3$ on the flexure of the 0.7 mm panel 132

Figure 8-15: Comparison of stress gradient across the radius of cohesive elements with n = 0.1 and 3 for the 3.0 mm model 133

Figure 8-16: Maximum principal stress distribution across the adhesive when modelled with cohesive elements ($n = 0.1$) 134

Figure 9-1: Strength threshold for generated from the yield envelopes of joints with different surface preparation methods and environmental conditioning 136

Figure 9-2: Comparison between the prediction by the modified Drücker-Prager/cap plasticity material and cohesive elements 139

Figure 9-3: Comparison of stress distribution across the damage zone lengths of the cohesive models with n = 0.1 and across the adhesive when modelled by the cap plasticity material 140

Figure 9-4: Vectors of the principal stresses within the adhesive layers of the 0.7 mm uniform panel model with a) cap plasticity material and b) cohesive model with n = 0.1 141

List of Tables

Table 3-1: Surface preparation method for the bond area of the joints. 27

Table 4-1: Shear strength measured from single lap-shear joints according to different surface preparation technique 45

Table 4-2: Mode I fracture toughness of adhesives 54

Table 4-3: Mode II fracture toughness of adhesives 54

Table 5-1: Maximum length for the edge elements of the scarf joints 61

Table 5-2: Material properties for linear elastic analysis [66, 68] 64

Table 6-1: Parameters for the von Mises material model in ABAQUS 79

Table 6-2: Modified Drücker-Prager/Cap plasticity parameters for the FM®300 adhesive layer. 88

Table 6-3: Modified Drücker-Prager/Cap plasticity parameters for the Hysol EA 9309.3NA adhesive layer 88

Table 7-1: Comparison of failure strengths from FE prediction and experimental measurement for the tensile butt joint. 97

Table 8-1: Material properties specified in ABAQUS for the cohesive elements with linear damage evolution 120

1 Introduction

1.1 Background

1.1.1 Motivation for Research

Airworthiness certification of bonded repairs to aircraft primary structures remains unresolved due to the lack of non-destructive inspection techniques to detect weak bonds (manufacturing flaw or service-induced damage) or a potential deterioration in bond strength caused by environmental degradation from moisture ingress. According to the Federal Aviation Regulations [1], structures must be able to withstand the design ultimate load in the presence of detectable damage and the design limit load when disbond has reached the maximum possible size. The latter requirement effectively assumes that adhesively bonded repairs are completed disbonded. As a result, bonded repairs are limited to maintenance critical structures [2, 3] and flight-critical structures that are still able to sustain the full flight envelope in the absence of the repair [4]. In other words, bonded repairs are currently given no structural credit in the case of primary structures.

One approach to overcome the certification difficulty is through the use of test coupons to assess the strength of the actual bonded repair, which has been patented by Airbus [5]. The rationale of this technique is that the strength of the satellite test coupons can represent the bonded repair because it was bonded using the same material, at the same time, under the same conditions and are subjected to the same loading conditions as the bonded repair. The patent requires the test coupons to withstand multifold of the flight critical load endured by bonded repair which should ideally be less than the fracture strength of the bond. Through the use of satellite test coupons, the strength of the repair could be interrogated without

interference or introduction of defects into the actual bonded repair. The practicality of implementing such test coupons as a proof test to monitor the bond integrity on aircraft structures were demonstrated in the works of Baker *et. al.* [6]. The test coupons provide a means to discern non-existent bonds formed between the repair adhesive and the structures that are otherwise undetectable by conventional NDI techniques.

An alternative approach to the direct detection of weak bonds is to develop a data-driven approach for certification of bonded repairs. Compliance to certification standards can be demonstrated if the probability of a bonded repair failing due to weak bond strength is found to be sufficiently low such that the reliability is not affected. In this context, the Defence Science and Technology Organisation (DSTO) has undertaken an Adhesive Bonded Repair Assessment Program (ABRAP) [7] sponsored by the Royal Australian Air Force (RAAF). The main purpose of the ABRAP is to quantify the environmental durability of adhesive bonded repairs by characterising the residual strength of bonded patch repairs on retired aircraft parts using the Pneumatic Adhesion Tensile Testing Instrument (PATTI), as illustrated in Figure 1-1. The aims are to demonstrate the durability of bonded repairs, as appraised from the shear strength of the adhesive bond, by testing coupons cut from retired aircraft components. The reliability of bonded repairs can be demonstrated if the probability of these coupons failing below the intended repair design allowable shear strength is sufficiently low. Majority of the pull-tests were performed on repairs bonded with Cytec FM300 and FM300-2K.

The test, when conducted in a laboratory environment, is capable of producing reliable results. However, the variability in measured test strength that occurs in field conditions, where the loading geometry and substructure may vary considerably, has not been quantified. The PATTI test was originally designed to test the adhesion of coating systems on metal substrates [8] by measuring the amount of pressure required to detach the pull-stub along

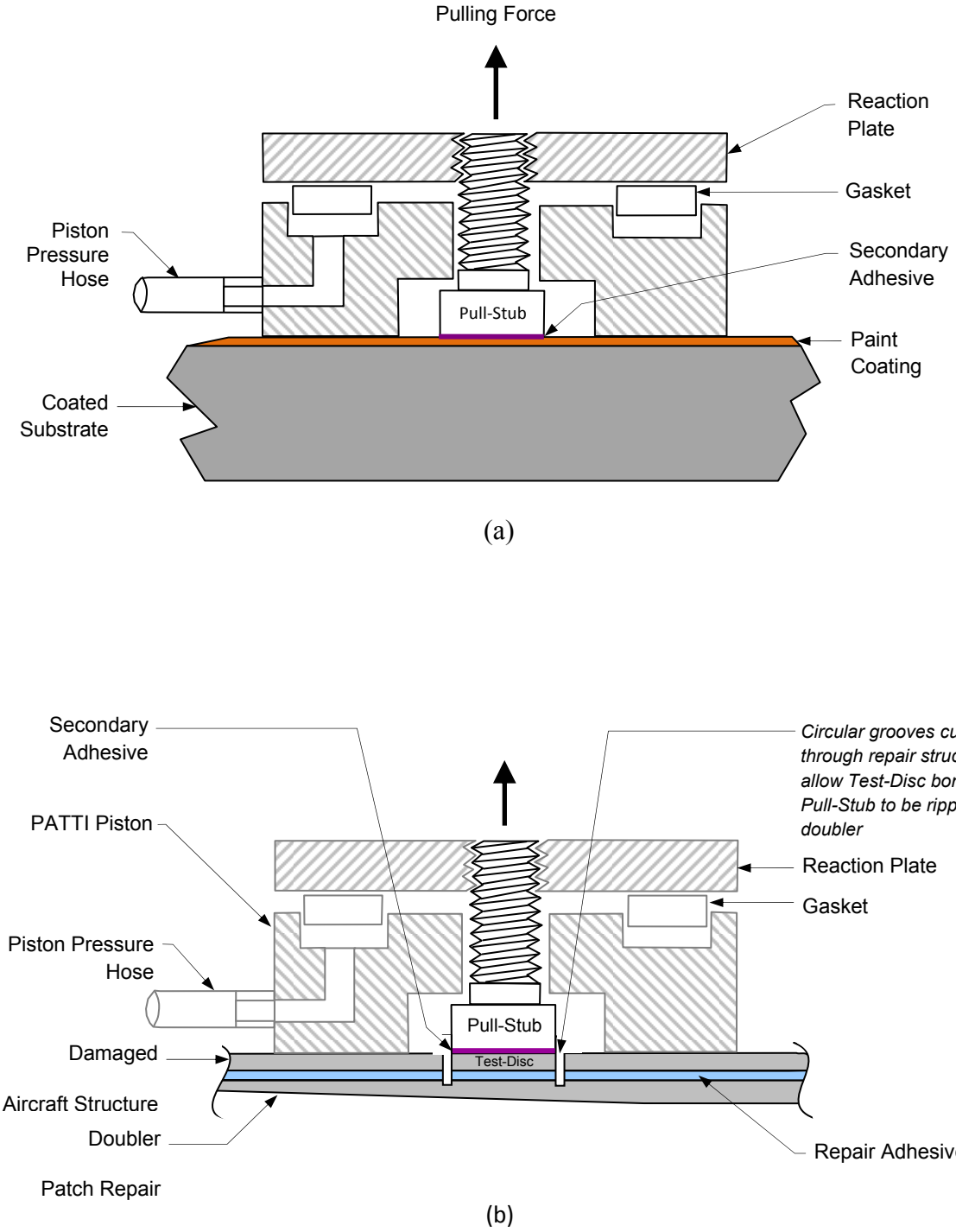

Figure 1-1: PATTI test configuration as used a) to test the adhesion of surface coatings and b) to obtain the residual flatwise tensile strength of bonded repairs on retired aircraft structures

with the coating off the substrate as shown in Figure 1-1a. The PATTI test was adapted to the configuration shown in Figure 1-1b to measure the flatwise tensile strength of bonded repairs in the assessment program.

To set up the test configuration for bonded repairs, a circular groove is first bored through one side of the bonded repair panel and the adhesive to create a '*Test-Disc*' which remains bonded to the underlying panel. It is worth to mention that the test-discs could also be created from the repair patch instead of the damaged structure shown in Figure 1-1b. A pull-stub is then bonded onto the test disc with a secondary adhesive. After the secondary adhesive has cured, the piston housing is fitted over the pull-stub and the reaction plate tightened onto the threaded portion of the pull-stub. When the gasket within the piston housing is inflated by pressurised gas, it exerts a force on the reaction plate which in turn causes the plate to be lifted from the housing. After sufficient pressure is supplied, the rising reaction plate fractures the bonded repair. Sometimes the secondary bond between the stub and the test-disc is unintentionally fractured.

In a recent study [3], PATTI tests performed on a composite patch repair bonded on a fatigue-cracked F-111C wing with Cytec FM73 adhesive exhibited predominantly cohesive failure which is defined when residues of adhesive are left on both sides of the fracture surface. Most of the mixed cohesive-interfacial failure occurred at the tapered edge of the patch repair. A mixed cohesive-interfacial failure shows a combination of cohesive failure and interfacial failure. The fracture mode is classified as interfacial failure when residues of the adhesive are only found on one side of the fracture surface and the metallic adherend is exposed on the other. It was interesting to note that the cohesive failure strength near the tapered-edges of the patch were lower than those in the central region. Nevertheless, the pull-off strengths in the central region of the patch were still lower than the strength specified in the FM73 material datasheet [9]. Some of the mixed cohesive-interfacial failures observed

along the patch edges had pertinent strength far less than the average cohesive failure strength of the repair patch.

The possible reasons for the lowered failure pull-strengths at the edge of the patch were suspected to be significant bond degradation during aircraft operation and/or the reduced adherend thickness at the tapered region.

1.2 Gaps in Available Knowledge

1.2.1 Inferring Shear Strength from Pull-Off Strength

While torsion testing allows a direct measurement of the shear strength of bonded repair, local buckling of the thin unsupported aluminium skin has been reported as an unresolved problem [6] resulting from the application of large torsional loads. On the other hand, the load required to fracture the adhesive bonds in tension is relatively low.

The PATTI test loads the bonded repair in tension to measure the flatwise tensile strength of the bond. This measurement only gives an indication of the integrity of the bond but not the shear strength which governs the effectiveness of the repair. Consequently, a method is required to relate the PATTI tensile strength to the shear strength of the bond.

The adhesive bond experiences tensile and shear stresses when a butt joint is loaded in tension [10-12]. The PATTI pull-test is expected to have similar stress distribution to the tensile butt joint because both joints appear to have comparable loading configuration. The tensile and shear yielding behaviour of structural adhesives are generally related via the von Mises criterion or the linear Drücker-Prager criterion [13, 14].

1.2.2 Variation in Fracture Modes

1.2.2.1 Inadequate Surface Preparation

Improper surface preparation was suspected to be one of the causes for the partial and full interfacial mode failure observed in the PATTI pull-tests. It is known that the strength of the interfacial bond depends on the cleanliness, roughness and chemical treatment of the bonding surfaces [15]. Improper surface treatments will also promote interfacial bond degradation.

The bonding surfaces of the repairs performed on the F-111 aircraft were documented to be prepared to the standard technique employed by the Royal Australian Air Force (RAAF). This technique has been shown to produce robust repair joints under laboratory environment [15, 16]. Nevertheless, it is possible for the bonded repairs in the assessment program to have inferior strength because they were installed under field conditions which are a far cry from the pristine conditions of a laboratory. The effects of surface preparation, which in turn affects the fracture modes of the bond, on the yield envelope(s) of the adhesive (or the joint) are yet to be established.

1.2.2.2 Bond Degradation

Bond degradation was suspected to be another cause for the variation in pull-strength measurements and failure modes because the ABRAP pull-tests were performed on bonded repairs that were subjected to service conditions; i.e. flight loads and environmental weather. Although bond degradation can be caused by a myriad of factors, the work in this thesis focuses on the effects of hot-wet environmental conditioning.

Bond degradation can occur as adhesive degradation, interfacial degradation or a combination of both. Adhesive degradation is defined as a weakening of the adhesive that

results in cohesive failure and interfacial bond degradation is the weakening of the adhesion between the adhesive to the interface that results in interfacial failure.

The effect of moisture diffusion on bond degradation was expected to be prominent along the edges of the adhesive in the metallic bonded repair patches tested in the assessment program. The moisture diffusion to the bonded repairs occurs through exposure to the relative humidity of the environment they were kept and at the worst-case scenario exposure to rain. The effects of bond degradation on the measured pull-strength from the bonded repair are yet to be determined.

1.2.3 Loading Configuration

When testing the adhesion of surface coating with the PATTI, the substrate does not deflect significantly as the pull-stub is lifted because the adhesion strength of most coating systems is relatively low compared to structural adhesives and the substrates are sufficiently thick. However, repairs bonded to aircraft skin structures are generally made of thin-gauge metallic or composite materials, either supported by stringers or honeycomb core. As such, the underlying substrate of the bonded test disc has the potential to deflect during PATTI testing if its thickness is sufficiently thin. The effect of this deflection on the measured pull-strength and stress distribution within the bond is yet to be studied.

One of the issues encountered when using the PATTI tester in field application is the possibility of applying an off-normal loading on the pull-stub during testing. An off-normal load can result when performing the pull-test on a curved structure which does not allow the entire area of the PATTI piston to make full contact with the curved surface. As a result, when the reaction plate is tightened onto the threaded pull-stub, there is still room for movement between the piston and the structure. In order to stabilize the tester, packer plates are shimmed between the gap of the piston and the structure as shown in Figure 1-2. However, over-

shimming induces an off-normal load on the pull-stub. Introducing an off-normal load onto the pull-stub changes the ratio of tensile and shear stress component causing the bond to yield.

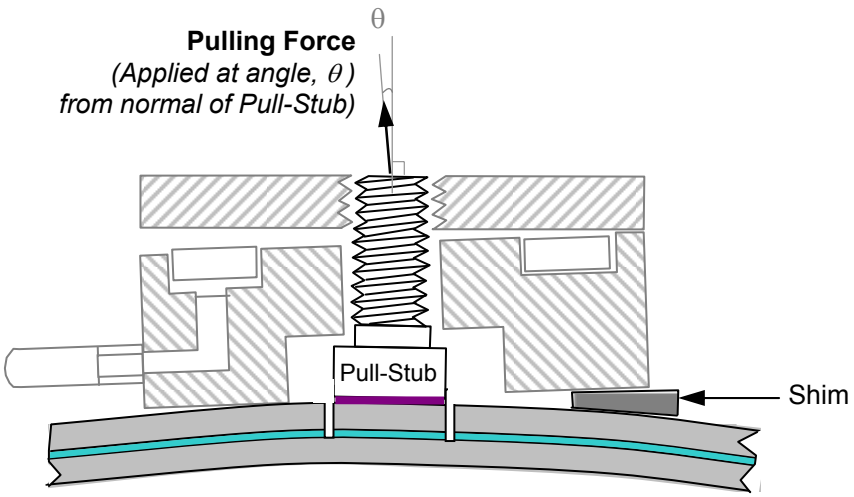

Figure 1-2: Off-normal loading caused by over-shimming.

1.3 Aims

The pull-test measures the flatwise tensile strength of the bonded repair, not the shear strength of the bond. The constitutive relationship relating the tensile and shear strength of the adhesive needs to be established before the shear strength of the bond can be inferred from the measured pull-strength. Application of the PATTI on curved surfaces makes it possible to unintentionally induce an off-normal loading on the bond during testing. The variation in the pull-off strength and modes of failure for the bonded repairs suggests that there could be geometrical configuration and bond degradation affecting the measurements. The following questions formed the basis for the work in this thesis:

i)) Is it possible to infer the shear strength of joints bonded with the FM300 adhesive from the tensile pull-off strength through the constitutive relationship of the adhesive?

ii) How do the strengths and failure modes of joints bonded with the FM300 adhesive compare when

a) bonded under pristine conditions (newly bonded joints; not subjected to environmental aging)?

b) prepared with inadequate surface treatment?

c) subjected to the environmental weather of field conditions (hot-wet conditioning in the environmental chamber)?

iii) How is the pull-off strength affected by the loading configuration

a) of an off-normal load?

b) when the PATTI test is performed on the tapered edges of the bonded repair?

The aims of this research are to (i) develop a method to infer the shear strength of bonded joints from their tensile pull-off strength, (ii) investigate and quantify the effects of surface preparation, environmental aging and loading configurations on the plastic yielding and fracture behaviour of film adhesive and (iii) develop a predictive model to account for the effects of adherend thickness and taper on the PATTI pull-off strengths.

1.4 Methodology

1.4.1 Inferring the Shear Strength of the Bond

Scarf angled joints and single lap-shear joints can be used to generate the failure envelope of the adhesive as the proportion of tensile and shear stress component varied. The failure envelope provides the constitutive properties of the adhesive when the joints fail cohesively. The proportion of tensile and shear stress components affecting the yield of each joint and their corresponding fracture strength are required to obtain the failure envelope for the adhesive. The strength of the joints are then recorded when they are loaded to failure in tension.

Finite element models of the scarf and lap-shear joints need to be constructed and assigned with linear elastic properties to determine the proportion of tensile and shear stress components for each joint angle when they are loaded in tension. The tensile and shear stress components can then be normalised by the load applied to produce them.

The experimental fracture strength is then multiplied with the normalised stress components of the corresponding scarf angle to generate the surface for the yield envelope. The adhesive is verified to obey the modified linear Drücker-Prager yield criterion if the plot forms a linear curve in the tensile-shear stress plane.

By plotting the constitutive relationship of the adhesive as a linear Drücker-Prager yield envelope in the tensile-shear stress plane, the shear strength of the adhesive is determined by taking the intercept of the curve when the tensile stress component is zero. However, the fracture strength and the failure mode of the joint also depend on the surface preparation techniques and the environmental conditioning. Consequently, the shear strength of joints exhibiting non-cohesive fracture surfaces cannot be inferred from the yield envelope representing the inherent properties of the adhesive.

However, yield envelopes for inadequate surface bonding can be generated for interfacial failure or mixed cohesive-interfacial failure from joints exhibiting those fracture surfaces. This can be done in the similar manner to which the constitutive relationship of the FM300 adhesive was generated from joints with cohesive failure. It should be noted then that such yield envelopes represent the behaviour of the bonds on the joints instead of the constitutive relationship of the adhesive. Again, the shear strength of the joint can be inferred from the yield envelopes by taking the intercept of the shear-axis. A total of five failure envelopes are generated according to the surface preparation methods employed and the environmental aging they are subjected to.

Additional empirical methods to infer the shear strength of joints affected by non-optimal loading configurations are developed with the aid of numerical analyses and described in Section 1.4.3.

1.4.2 Effects of Bond Degradation on Pull-Off Strength

Different surface preparation methods and environmental conditioning are used to produce the experimental joints in this thesis to study their effects on the fracture modes and fracture strength of the joints. All the joints are cured under vacuum-bag to replicate the curing process used in field repair and to produce representative joint properties.

Since the bonded repairs in the assessment program were installed under field conditions, the standard RAAF surface preparation technique was deliberately altered to capture conceivable field practices that could lead to inferior bond strength and partial/full interfacial fracture. In total, three surface preparation techniques were used to prepare the bonding surfaces of the joints: the standard (RAAF) Method A and two other alternatives, Method B and Method C, to produce purely cohesive, mixed cohesive-interfacial and purely interfacial failure modes. Detailed descriptions of these methods are given in Appendices I and II.

Some of these joints are tested straight away while some are conditioned in a hot-wet environmental chamber to facilitate moisture diffusion into the adhesive prior to testing. The fracture strengths of these joints are multiplied with the normalised stress components of the corresponding scarf angle to generate the yield envelopes resulting from different surface treatments and environmental aging.

Achieving those three different failure modes will aid the investigation of the effect of fracture modes on the strength of both unconditioned and conditioned joints and provide a

better understanding to the causes for the variety of fracture strengths and modes observed in the ABRAP.

1.4.3 Effects of Loading Configuration on Pull-Off Strength

Finite element models are constructed to study the effects of the loading configuration on the measured pull-strength. The constitutive behaviour of the adhesive is represented by two types of material models: an elastic-plastic stress-strain material model and cohesive elements. When the numerical models are able to predict the experimental pull-off strength, the causes for the variation in failure modes and measured strengths in the experiments can be investigated through the strain distribution and deflection of the models.

The stress-strain material model describes the yield envelope generated from the scarf and lap-shear joints experiments and requires a failure criterion at a characteristic distance to predict the strength of the joint. The characteristic distance for the material model has to be calibrated each time a material parameter is changed or a different failure criterion is used.

The cohesive element uses fracture mechanics to describe the behaviour of the adhesive as a stress-displacement relationship. The convenience of using cohesive elements to model the adhesive layers in the FE models comes from not having to calibrate the characteristic length each time the material is changed or a different failure criterion is used. Modelling with cohesive elements require the fracture toughness and fracture strength of the adhesive resulting from Mode I, Mode II and Mode III loading. The properties of the FM300 adhesive under Mode II and III loading are assumed to be similar. The double cantilever beam (DCB) is used to generate the Mode I fracture toughness of the adhesive and the end-notched flexural test is used to generate the Mode II fracture toughness. The fracture strengths of the adhesive are obtained from the tensile butt joint and single lap-shear experiments.

The effects of applying off-normal loads on the pull-strength are investigated through the same FE models of the scarf joints initially used to determine the proportion of normalised tensile and shear stress components of each scarf angle. The effects of off-normal loading on the pull-strength is verified when the numerical models are able to predict the same trend as the experimental values. A method can then be proposed to remove the effect of off-normal load from the measured pull-test to obtain the shear strength of the bond.

PATTI tests are performed on bonded tapered panels to generate the pull-strengths on tapering and uniform sections. The bonding surfaces of the panels are prepared to one of the alternative surface preparation techniques shown by the scarf joint experiments to produce comparable strength and failure mode to joints prepared to the standard RAAF technique. FE models of the pull-test configurations need to be constructed to assess the effects of these geometries on the strength measurements and to study the strain distribution within the adhesive layer. Full three-dimensional models also need to be constructed for the tapered edge configuration and axisymmetrical models can be constructed for the uniform underlying thickness configuration to save computational resources.

1.5 Thesis Outline

Following the introduction of the research project in the current chapter, Chapter 2 summarises the relevant literature studies reviewed to achieve the objectives of the research. All the experimental procedures conducted throughout the course of this research are presented in Chapter 3 and their corresponding results are presented in Chapter 4.

The meshes of finite element models developed for all numerical analyses are presented in Chapter 5. The constitutive behaviour of the adhesive, described as an elastic-plastic stress-strain material models for numerical analyses are presented in Chapter 6.

The technique to predict the PATTI pull-off strength using the elastic-plastic material models is presented in Chapter 7. In this chapter, the finite element models also investigate the consequences of applying an off-normal load on the pull-stub and performing the pull-test on different adherend thickness and taper. Chapter 8 describes the technique to express the adhesive failure with cohesive elements and compares the strength predicted with various shapes of damage evolution profiles.

Chapter 9 presents empirical methods to infer the shear strength of a bond from its tensile pull-strength without the effects of off-normal loading on the pull-stub or the flexural deformation of the adherend. In addition, this chapter also compares the two methods of predictive numerical analysis used in this thesis: stress-strain material with a failure criterion and cohesive elements with damage evolution profile. Lastly, Chapter 10 summarises the conclusions derived from the efforts of this research.

2 Literature Review

The presence of tensile and shear stresses within the adhesive of the tensile butt joints and lap-shear joints indicate that the yielding of structural adhesives are influenced by a combination of these stresses. The yielding behaviour of adhesives is discussed in Section 2.1

The selection of surface treatment techniques to produce a variety of fracture modes on the joints in this thesis is guided by past studies on the procedure to produce durable joints. These previous works are discussed in Section 2.2.

Moisture diffusion predictions for epoxy adhesives are summarized in Section 2.3. These predictions were needed to ensure that the joints are conditioned for a sufficiently long duration to show the effects of environmental degradation.

A failure criterion is required to predict the strength of the joints when using an elastic-plastic stress-strain material model in ABAQUS to describe the behaviour of the adhesive in numerical analyses. The selection of the failure criterion is presented in Section 2.4. The representation of the adhesive through cohesive elements is discussed in Section 2.5.

2.1 Yielding behaviour of the adhesive

Many studies [10, 11, 17, 18] have shown that both tensile and shear stresses prevail in the adhesive when a butt joint is loaded in tension. From the linear elastic analysis of an axisymmetric tensile butt joint [10], the stress distribution in the bondline is approximately uniform in the interior, with variation concentrated only near the edges. The tensile and shear stress distributions at the edges were shown to change through the adhesive thickness.

Lap-shear joints are commonly tested to determine the shear strength of structural adhesives [19]. In this case, tensile (peeling) stress also occurs within the adhesive in addition

to shear stress [20, 21]. The tensile stress is known to concentrate at the edges of the bond length due to the warping motion of the adherends during testing. Although the thick adherend shear test [22] reduces the peeling effect, the manufacturing and equipment requirements for the test are more complex than the single lap-shear test [23].

The yielding of structural adhesives has been reported to be affected by the hydrostatic pressure component [24]. The pressure sensitivity of the adhesive is due to the crazing of the polymer when loaded in tension [25, 26]. The tensile and shear yielding behaviour of structural adhesives are generally related via the von Mises criterion or the linear Drücker-Prager criterion [13, 14].

The linear Drücker-Prager or otherwise known as the modified von Mises yield criterion relates the tensile and shear stress components affecting the yield of structural adhesive according to the linear function given in Equation 2-1.

$$\sigma_{vm} + m\sigma_m = \sqrt{3}\tau_0 \qquad \text{Eqn. 2-1}$$

The tensile stress within the adhesive of a bonded joint is represented by the hydrostatic pressure component, σ_m and the shear stress is represented by the von Mises stress component, σ_{vm}. The sensitivity of the adhesive to hydrostatic pressure is denoted by m and the shear yield stress is denoted by τ_0. The σ_m and the σ_{vm} are calculated from the principal stresses, σ_1, σ_2 , σ_3 according to Equations 2-2 and 2-3 respectively.

$$\sigma_m = \frac{\sigma_1 + \sigma_2 + \sigma_3}{3} \qquad \text{Eqn. 2-2}$$

$$\sigma_{vm} = \sqrt{\frac{(\sigma_1 - \sigma_2)^2 + (\sigma_2 - \sigma_3)^2 + (\sigma_3 - \sigma_1)^2}{2}} \qquad \text{Eqn. 2-3}$$

When σ_{vm} is plotted against σ_m, the shear yield stress, $\sqrt{3}\tau_0$ becomes the intercept of the σ_{vm} -axis when the hydrostatic component is zero. This then leaves *m* as the slope of the curve.

Previous work [13] had shown that the modified Drücker-Prager/Cap plasticity yield criterion [27] was able to provide a good description of the yielding and plastic flow of a similar structural film adhesive commonly used in the aerospace industry, Cytec FM73, when subjected to triaxial stresses. In this investigation, the FM300 adhesive is considered to obey the linear Drücker-Prager yield criterion when it can be shown that the ratio of the von Mises stress to the hydrostatic pressure components affecting its failure varies linearly.

The effect of the scrim cloth of the film adhesive on its mechanical properties was not included in the scope of this thesis because the sponsors of this project wanted a method to interpret the strength of joints bonded with the FM300 adhesive with carrier. Nonetheless review of the works by Brewis et. al. [28] has shown that the presence of a close-knit carrier lowered the shear strength of the bonded joint but not its peel strength. It has been suggested that the carrier acts as inert fillers that reduces the strength of the adhesive by the volume fraction present and that the close-knit construction of the carrier prevented the adhesive penetrating it.

2.2 Influence of Surface Preparation Methods

In addition to determining the failure envelope of the adhesive as the ratio of the tensile and shear stress component varied, the scarf and lap-shear joint experiments also provides the means to characterise the yielding behaviour of joints produced from field repair techniques and not merely to produce the strongest possible joints under laboratory conditions.

Although it is known that joints produced from vacuum-bag curing (negative pressurisation) have more voids compared to joints cured under high positive pressurisation [29], vacuum bag pressurisation are used in field repair as it is often not feasible to fit the

damaged structure into an autoclave to apply positive pressurisation during curing. Earlier works [29, 30] showed that percentage void content up to 25% did not affect the strength of the T-peel joints. B-staging the adhesive at 80°C for 20 minutes prior to bonding had been shown to reduce the formation of voids during the curing process [31].

The bonding surfaces of the scarf and lap-shear joints prepared to the standard (RAAF) technique [15, 16] were expected for joints prepared to this reference technique to fail by cohesive mode. The alternative surface preparation methods were used to produce mixed cohesive-interfacial and interfacial fracture modes. This is done to evaluate the ability of the modified linear Drücker-Prager criterion to describe the yield behaviour of the adhesive undergoing different modes of failure and to study the effects of the fracture modes on the strength of the joints.

The first alternative surface preparation technique replaces the grit-blasting step for abrasion with alumina paper. This technique had previously been shown to produce equally durable joints to those prepared by the RAAF technique [16]. The second alternative technique prepares the joint without the scrubbing the bond surfaces with Scotchbrite™ and without the application of the γ-glycidoxypropyl-trimethoxysilane. It has previously been shown that joints prepared without silane are not as strong as those with silane and they are also more susceptible to interfacial degradation [15, 32].

2.3 Influence of Environmental Degradation

Moisture diffusion occurs when the bonded joints are subjected to hot-wet environment and is known to affect the performance of the joint [33]. Most epoxies, including the FM300 adhesive, show high percentage of strength recovery upon moisture desorption [34-36]. Moisture diffusion for epoxy-based systems had been shown to be largely caused by the motion and occupation of moisture within the microstructure of the adhesive [24, 34, 37, 38].

Some of this moisture interacts with the reactive groups (hydroxyl) of the epoxy and causes permanent damage to the adhesive [39-41]. On the other hand, extended duration of exposure to moisture, and not merely the amount of moisture content [42], has been shown to cause irreversible damage to the interfacial bonds of joint [43].

The moisture diffusion profile of the adhesive has to be determined to predict the level of moisture saturation and to ensure that the scarf and lap-shear joints are exposed to moisture for a sufficient duration of time in the environmental chamber. Joints bonded with the FM300M adhesive have been shown to be durable when exposed to moist marine atmosphere over a duration of 10 years [44]. Previous works [45-47] have shown that the moisture diffusion profiles of epoxy adhesives and compounds are best described by the dual-staged Fickian diffusion equation given in Equation 2-4.

$$M_{wt} = M_1\left[1-\frac{8}{\pi^2}\sum_{n=0}^{\infty}\frac{1}{(2n+1)^2}\exp\left[\frac{-(-2n+1)^2\pi^2 D_1}{4}\times\frac{t}{l^2}\right]\right] + M_2\left[1-\frac{8}{\pi^2}\sum_{n=0}^{\infty}\frac{1}{(2n+1)^2}\exp\left[\frac{-(-2n+1)^2\pi^2 D_2}{4}\times\frac{t}{l^2}\right]\right] \quad \text{Eqn. 2-4}$$

whereby M_{wt} is the moisture uptake. M_1 and M_2 are the moisture weight gained by the first and second stage diffusion respectively. The parameter M_2 could be expressed in terms of the saturation weight uptake, M_∞ as M_2 (= M_∞ - M_2). D_1 is the Fickian diffusion coefficient for the first stage where Fickian behaviour is dominant and D_2 for the second stage where the anomalous moisture uptake behaviour is dominant. The first stage Fickian diffusion occurs rapidly and is suggested to be caused by the migration of the water molecules from the surrounding environment into the microscopic pores and voids within the adhesive. The second stage anomalous diffusion occurs concurrently with the first stage diffusion, but at a slower rate. This anomalous diffusion is found to be caused by formation of permanent

hydrogen bonds between the water molecules and the hydroxyl groups of the polymer chains [39-41].

The initial 60% of moisture uptake can be described by the simplified version of the original Fickian equation given in Equation 2-5. As such in the dual-stage equation, M_1 caused by the movement of water molecules within the microscopic pores of the adhesive can be represented by the initial 60% moisture uptake.

$$M_{wt} = M_{\infty} \times \frac{2}{l}\sqrt{\frac{Dt}{\pi}} \qquad \text{Eqn. 2-5}$$

The bulk diffusion coefficients are considered adequate in estimating the percentage moisture content within the adhesive layer for the joints even though it is known that the rate of diffusion along the adhesive-adherend interface is higher [41]. This is because the calculation for the percentage moisture content is merely to ensure that there is sufficient moisture within the joint prior to testing and not as a parameter to correlate with the joint strength. Consequently, calculation with the bulk diffusion coefficients provides a conservative estimation of the moisture content within the joints. The carrier material does not promote diffusion because water does not wick along the carrier-adhesive interface [48] and the presence of the size on the carrier blocks the continuous transmission of water by capillary effect.

Conditioning the joints in a hot-wet environmental chamber accelerates bond degradation to allow the effects of environmental weathering on the strength and fracture mode of the bonds to be investigated. The durability of joints produced from the different types of surface preparation techniques will also be reflected in the conditioned joints.

2.4 Failure Criteria for Strength Prediction

The von Mises and modified Drücker-Prager/Cap plasticity material models in ABAQUS describe the behaviour of the adhesive through its stress-strain relationship. The material parameters for these models need to be generated from the scarf joint experiments and the manufacturer's datasheet. Through these models, the adhesive can be described to behave as an elastic-perfectly plastic material.

When using these material models to portray the behaviour of the adhesive, a failure criterion is required to predict the strength of the joints since no damage evolution was specified for them. It was previously observed by Liechti et al. [26] and Wang and Chalkley [13] that epoxy adhesives under tensile loading tend to fail by crazing due to the high triaxial tensile stress state at the crack tip. The crazing process involves the formation of microcracks ahead of the crack tip in the direction of the maximum principal strain. A failure criterion [25] expressed in terms of the maximum principal strain, $\varepsilon_{\max}$ and the hydrostatic stress, σ_m is given in Equation 2-1.

$$\varepsilon_{\max} + \frac{\sigma_m \tan\beta}{E} = \varepsilon_c \qquad \text{Eqn. 2-6}$$

where ε_c is the critical strain value when the hydrostatic stress, σ_m is zero. The parameter $\tan\beta$ reflects the sensitivity of the material to hydrostatic tensile stress. The Young's modulus is denoted by E. The application of this failure criterion is elaborated in Section 7.1.

In the parametric study by Broughton *et. al.* [49], the maximum shear strain failure criterion was found to give the best strength prediction for the single lap-shear joint and the maximum principal strain failure criterion for scarf joints. However, the critical strain values used in their predictions were measured directly from tensile and shear tests of the bulk epoxy based adhesives used in their work. The method to combine the two failure criteria into the

maximum principal strain failure criterion to predict the strength of the joints is also presented in Section 7.1.

The strain failure criterion chosen for the material models assume fracture of the joint when the strain at the characteristic length in the adhesive reaches its critical failure strain [49]. However this means that the calibration for the characteristic length is required each time any material parameter is changed or a different failure criterion is used. The method to calibrate for the characteristic distance is presented in Section 7.2.1.

2.5 Numerical Analyses with Cohesive Models

Another method to model adhesive failure in joints is via cohesive elements which can be specified with damage evolution properties. The formulation of cohesive elements in ABAQUS incorporate fracture mechanics to describe the damage evolution as energy dissipated per unit area through a stress-displacement relationship [50]. By using cohesive elements, there is no need to calibrate the characteristic length for the mesh or select a suitable failure criterion.

The damage evolution of the cohesive elements represents the "*stress-softening*" behaviour of the material due to the loss of material stiffness after damage initiation caused by the accumulation of microscopic defects [51]. The *"stress-softening"* profile can be described by the power softening law given in Equation 2-7 [52].

$$\tau = \tau_{\max}\left(1-\frac{\delta}{\delta_c}\right)^n \qquad \text{Eqn. 2-7}$$

whereby τ and δ respectively denotes the load-carrying capacity and the crack opening displacement of the material at the instance, τ_{max} denotes the strength of the material (at damage initiation) and δ_c denotes the crack opening displacement at failure (when τ drops to

zero). The shape of the profile is controlled by the softening index, n. The application of the power softening law to describe the damage evolution profiles for cohesive elements is elaborated in Section 8.1.2.

Materials have elastic-perfectly plastic behaviour when $n = 0$ and a brittle nature with no softening region when $n = \infty$ [52]. The typical fracture of polymers in plane stress has been shown to obey $0 < n < 1$. Different damage evolution profiles were generated for the FM300 adhesive through the tabular softening function in ABAQUS to study their effects on the predicted strength.

The fracture toughnesses and fracture strengths in Mode I, Mode II and Mode III are required to generate the damage initiation and evolution profile for the adhesive. Typically, adhesive are treated to be isotropic in shear mode and as such, the same Mode II properties can be specified for Mode III loading. The fracture strength is used to specify the stress at damage initiation. The crack opening displacement at damage initiation and total failure are derived from the fracture toughness and strength. The criteria to describe the fracture toughness and fracture strength for different mixed-mode are required since the material properties are only specified for their pure mode loading.

The quadratic stress criterion [53, 54] is typically chosen to determine the damage initiation stress for the mixed-mode loading of cohesive elements. This stress criterion relates the tensile and shear fracture strength of the material via a quadratic function to give the fracture strength for any transitional mode-mixity between the two pure modes. The linear law criterion [26] has been shown to capture the mixed-mode fracture toughness of the FM300 adhesive. This criterion combines to the Mode I and Mode II fracture toughness to give an equivalent toughness value representative of the mixed-mode.

3 Experiments

The PATTI pull-tests within the scope of this research were performed on a bonded panel. The ends of one adherend were milled to form a 3° taper to represent the edge region of a patch repair. The surfaces of the adherends were prepared in accordance with one of the surface treatment techniques used to prepare the scarf and lap-shear joints. The purpose of performing the PATTI tests on a bonded panel having one tapered adherend is to study the effect of adherend thickness and taper on the pull-off strength. Only one surface preparation technique was employed, although the methodology is expected to be valid for panels prepared using other surface treatment methods.

Predicting the PATTI pull-off strengths pertinent to tapered adherend requires input data for the adhesive when using the modified Drücker-Prager/cap plasticity material model and the cohesive elements. To this end, tests were conducted on scarf joints of varying angles, single lap-shear joints, double cantilever beam, and end notched flexural specimens.

Two batches of scarf and lap joints were bonded to allow one batch to be tensile tested directly and the other to be conditioned in a hot-wet environmental chamber for six months prior to testing. The joints were conditioned in the environmental chamber to facilitate the diffusion of water into the adhesive bonds. Three types of surface preparation techniques were used to prepare the bonding surfaces of the joints, with a view of producing purely cohesive, mixed cohesive-interfacial and purely interfacial failure modes. Achieving these three different failure modes will aid the investigation of the effect of fracture modes on the strength of both unconditioned and conditioned and provide a better understanding to the causes for the variety of fracture modes observed in the ABRAP.

Scarf joints of varying angles and single lap-shear joints were manufactured and tested to generate data pertinent to different ratios of tensile and deviatoric stress components for the FM300 adhesive. The fracture strengths obtained from these joints were used to verify if the yielding behaviour of the adhesive can be described by the linear Drücker-Prager yield criterion, which relates the deviatoric stress to the hydrostatic stress via a linear relationship [13, 55] as presented in Section 2.1. The shear strength of the bond can be interpreted from the pull-strength of the PATTI tests when the effect of these two loading modes on the strength of the joints is known.

The double cantilever beam and the end-notched-flexural tests were performed to measure the Mode I and II fracture toughness of the FM300 adhesive. These values are required to model the adhesive layers using with cohesive element approach. The bond surfaces of these specimens were prepared according to the same preparation technique used for the tapered edge panel experiment.

3.1 Scarf Joint Experiment

3.1.1 Pristine (Dry) Conditions

Aluminium alloy of 6060 T5 grade bars and 16 x 16 mm sections were lathed to 12 mm diameter sections for making tensile butt joints. The circular cross-sectional areas were milled to create scarf angles of 15°, 30°, 60° and 75°, as shown in Figure 3-1. Single lap-shear (SLS) joints, made from 1.6 mm thick aluminium alloy sheet of 2024 T3 grade and had overlap lengths of 12.7 mm [23], were used to represent the 90° loading condition.

The bond surfaces of the joints were prepared according to one of three surface preparation methods summarised in Table 3-1. Method A is the standard surface preparation technique used by the RAAF to achieve high quality and environmentally durable adhesive

bonds [15] and will serve as the reference to assess other surface treatment methods. A second set of joints were prepared according to Method B, where the Alumina grit blasting step was replaced by hand abrasion with alumina paper. Preliminary testing of joints prepared by these two surface preparation techniques showed very little difference in strength. The third set of joints were prepared according to Method C, where the silane was not applied because it has previously been shown that such joints are more susceptible to interfacial degradation [15, 32] when subjected to hot-wet environmental conditioning. The details of these surface preparation techniques are given in Appendices I and II. Three specimens were tested for each surface preparation method.

Figure 3-1: Joints with scarf angles of 0°, 15°, 30°, 60° and 75°.

Table 3-1: Surface preparation method for the bond area of the joints.

Surface Preparation Method	Procedure
A (RAAF)	Scotchbrite™ methyl ethyl ketone (MEK), Scotchbrite™ distilled water, Alumina grit blast, Silane
B	Scotchbrite™ MEK, Scotchbrite™ distilled water, Alumina paper abrade, Kimwipe with distilled water, Silane
C	MEK wipe, distilled water wipe, Alumina paper abrade, Kimwipe with distilled water

The Cytec FM300 film adhesive used to bond all the joints is blue and has a moisture resistant, tight-knit polyester scrim cloth [56]. The colour of the uncured FM300 adhesive is a slightly darker blue than the cured (dry) version shown in Figure 4-1a to d under Section 4.1.1. All the joints were cured at 177°C for 90 minutes and under 34 kPa vacuum bag environment. Further details of the curing procedures are given in Appendix III. While the vacuum bag is able to provide direct pressure onto the lap-shear plates, fixtures constructed of aluminium alloy channels shown in Figure 3-2 were used to align and ensure the bond surfaces maintain contact during the curing process. The fixtures were tightened such that the square-sections of the stubs were pressed

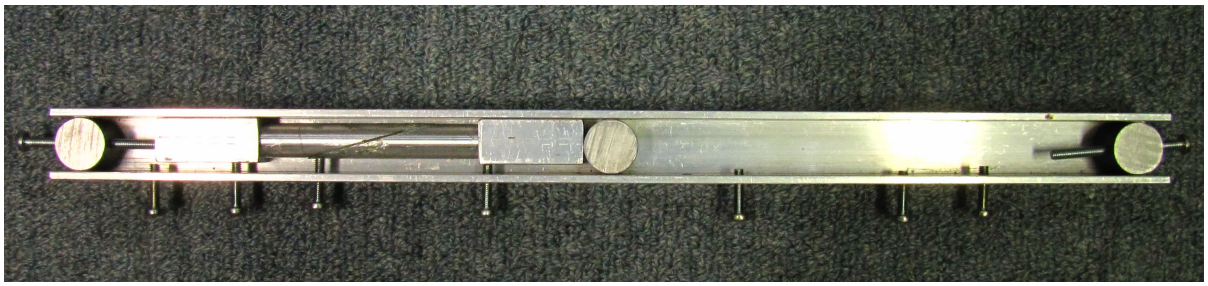

Figure 3-2: Fixture to align and maintain contact of scarf joints during curing

firmly against the inner edge of the fixture to maintain the alignment of the bonding surfaces for curing. The fixtures also squeezed the film adhesive down to the scrim cloth thickness during curing to ensure a constant adhesive thickness for all the joints. The adherend-fixture assemblies were placed in a vacuum bag to be cured in thermal oven, simulating the curing condition encountered in field repairs.

The bonded lap-shear plates were machined to 25.4 mm wide strips to produce individual SLS joints; the strips near the edges of the plates were discarded. All joints were loaded to failure under uniaxial tension in a 50 kN Instron machine at the rate of 1 mm / min.

3.1.2 Hot/Wet Conditioning

Two sets of scarf and single lap-shear joints were prepared according to Method A and Method C and bonded with FM300 adhesive as described in Section 3.1.1. The length of the doubler tabs on the grip ends of the lap-shear joints was increased from 25.40 mm to 76.20 mm in this batch to allow more grip area and to prevent the tabs from detaching during tensile testing. Due to the high percentage of voids observed on the fracture surfaces of the dry joints, the FM300 adhesive was B-staged at 80°C for 20 minutes prior to bonding to reduce the formation of voids during the curing process [31].

Previous studies [16] have shown that joints applied with γ-organosilane prior to bonding had better environmental durability compared to those without. Coupled with the

very similar fracture strengths of the shallow angled dry joints (up to 30°) prepared according to Method A and Method B (Section 4.1.1), no joints were prepared according to Method B since it is expected for joints prepared to Method A to be representative of joints prepared with γ-organosilane. Both batches of joints were conditioned in the environmental chamber at 80°C / 75% RH for 180 days.

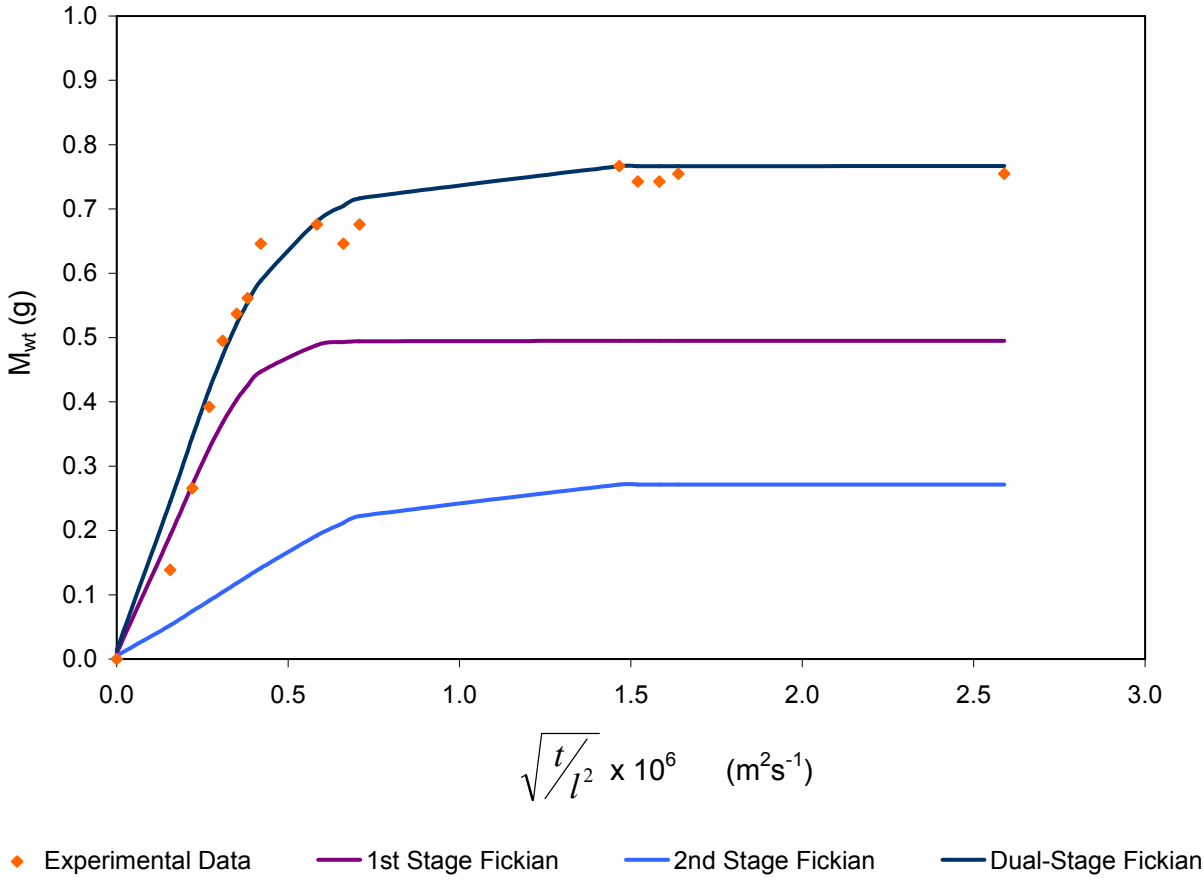

Figure 3-3: Dual-staged Fickian diffusion curve fitting for FM300 adhesive discs.

The moisture diffusion behaviour of the FM300 adhesive was first determined to allow the level of moisture saturation within the joints to be estimated. Circular adhesive discs were cured from two sheets of FM300 film adhesive and placed within the environmental chamber to measure the moisture weight uptake over time, t and diffusion distance, l as plotted in Figure 3-3. The moisture diffusion profile of the FM300 adhesive is best described by the dual-staged Fickian diffusion previously given by Equation 2-4 in Section 2.3.

$$M_{wt} = M_1\left[1-\frac{8}{\pi^2}\sum_{n=0}^{\infty}\frac{1}{(2n+1)^2}\exp\left[\frac{-(-2n+1)^2\pi^2 D_1}{4}\times\frac{t}{l^2}\right]\right]$$

$$+M_2\left[1-\frac{8}{\pi^2}\sum_{n=0}^{\infty}\frac{1}{(2n+1)^2}\exp\left[\frac{-(-2n+1)^2\pi^2 D_2}{4}\times\frac{t}{l^2}\right]\right] \qquad \textit{Eqn. 2-4}$$

The moisture weight gained by the first stage diffusion, M_1 was selected from the experimental weight uptake measurements closest to the initial 60% from full saturation. For the experimental measurements presented in Figure 3-3, M_1 corresponded to 65% of saturation. The two diffusion coefficients were determined by fitting the dual-staged Fickian equation to the experimental data using the least mean-squares method. The first stage diffusion coefficient, D_1 was found to be 4.88×10^{-12} m^2s^{-1} and the second stage diffusion coefficient, D_2 was found to be 9.00×10^{-13} m^2s^{-1}.

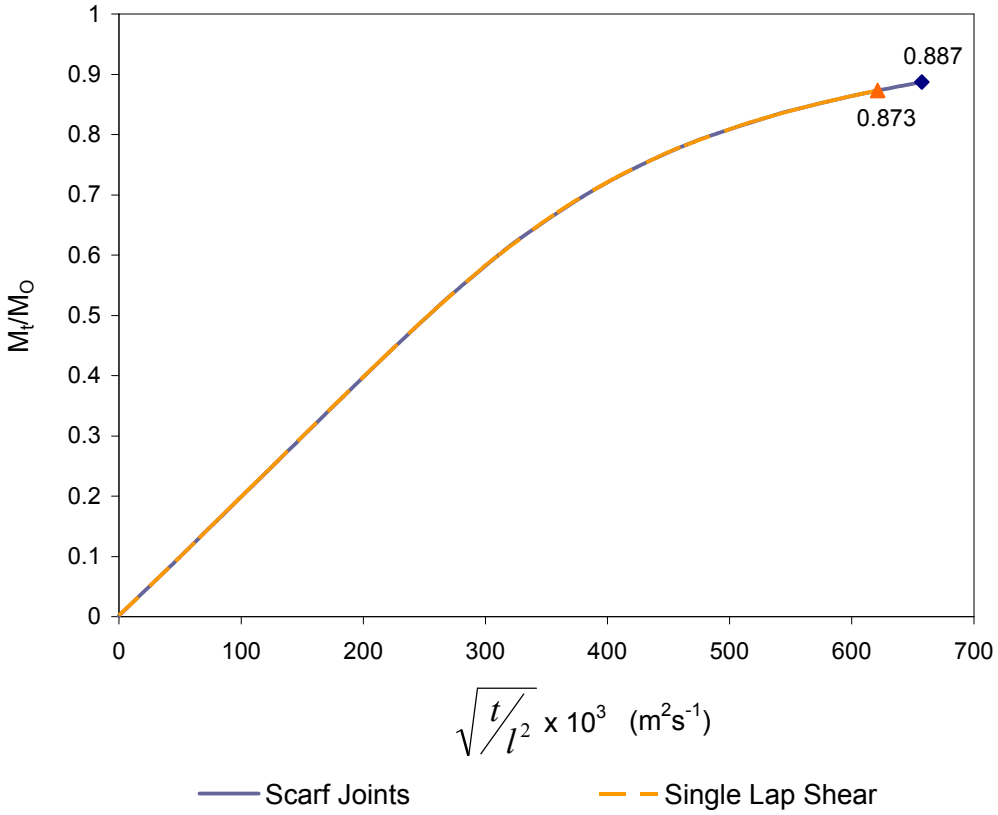

Figure 3-4: Estimating moisture saturation level within bonded joints.

Upon establishing the diffusion parameters for the FM300 adhesive, the levels of moisture saturation within the joints were calculated and plotted in Figure 3-4. Since all the scarf joints were milled from the same 12 mm diameter stock, the minor radius of the elliptical bond surface on each scarf joint remained the same. By assuming a unidirectional diffusion through the bondline thickness, the saturation time does not depend on the bonded area of the scarf joint.

Through this analysis, the adhesive in the joints were estimated to have been conditioned at more than 80% moisture saturation for approximately 30 days. The conditioned joints were allowed to cool to room temperature prior to testing at 1 mm / min in the 50 kN Instron machine.

3.2 Tapered Edge Panel Experiments

Two panels of aluminium alloy 7075 T6 grade of 3.0 mm thickness were bonded with the Cytec FM300 film adhesive, which was employed in bonding the doubler repairs on the F-111 aircraft [7]. Prior to bonding, one panel was milled to form a 3° angled taper similar to the doubler patches used in the repairs.

The bonding surfaces of the panels were prepared to surface preparation Method B described in Section 3.1.1. Method B was used to prepare the bond surfaces of the panels because shallow angle dry joints (up to 30°) were shown to produce similar strength to joints prepared to Method A. To reduce the level of voiding observed on the cohesive fracture surfaces of the dry scarf joints, the FM300 film adhesive was staged at 80°C for 20 minutes prior to bonding at 177°C for 90 minutes.

Individual discs for the PATTI test were created by boring circular grooves through the non-tapered adherend and the adhesive layer, to just surpass the bonding surface of the tapered panel as shown in Figure 3-5. The width of the groove, denoted by *e*, is approximately

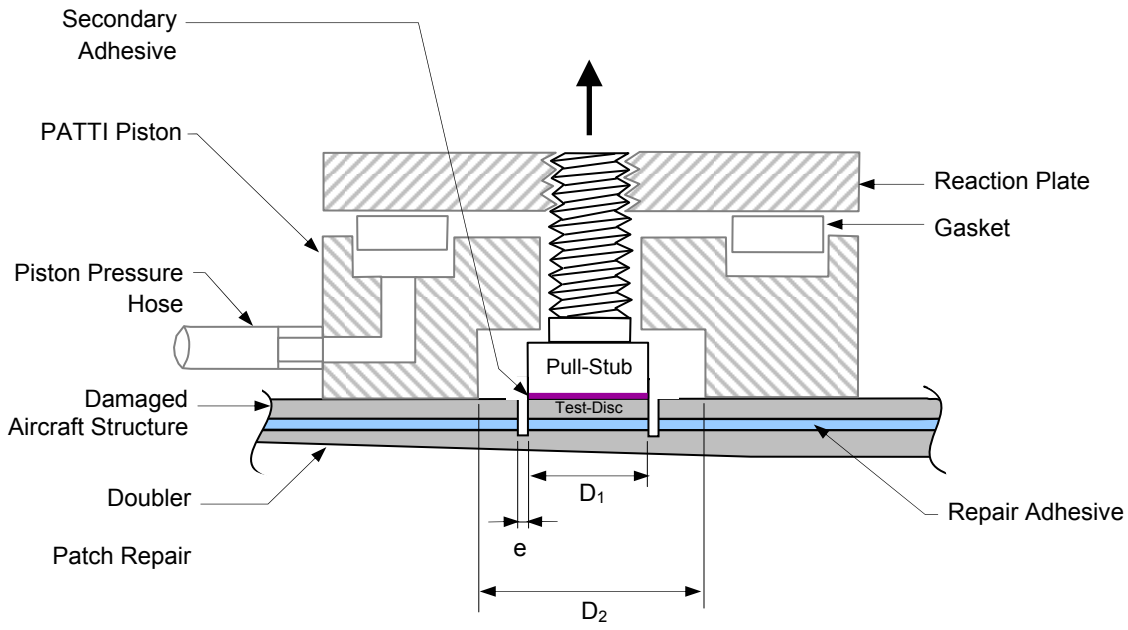

Figure 3-5: PATTI test configuration on bonded panels.

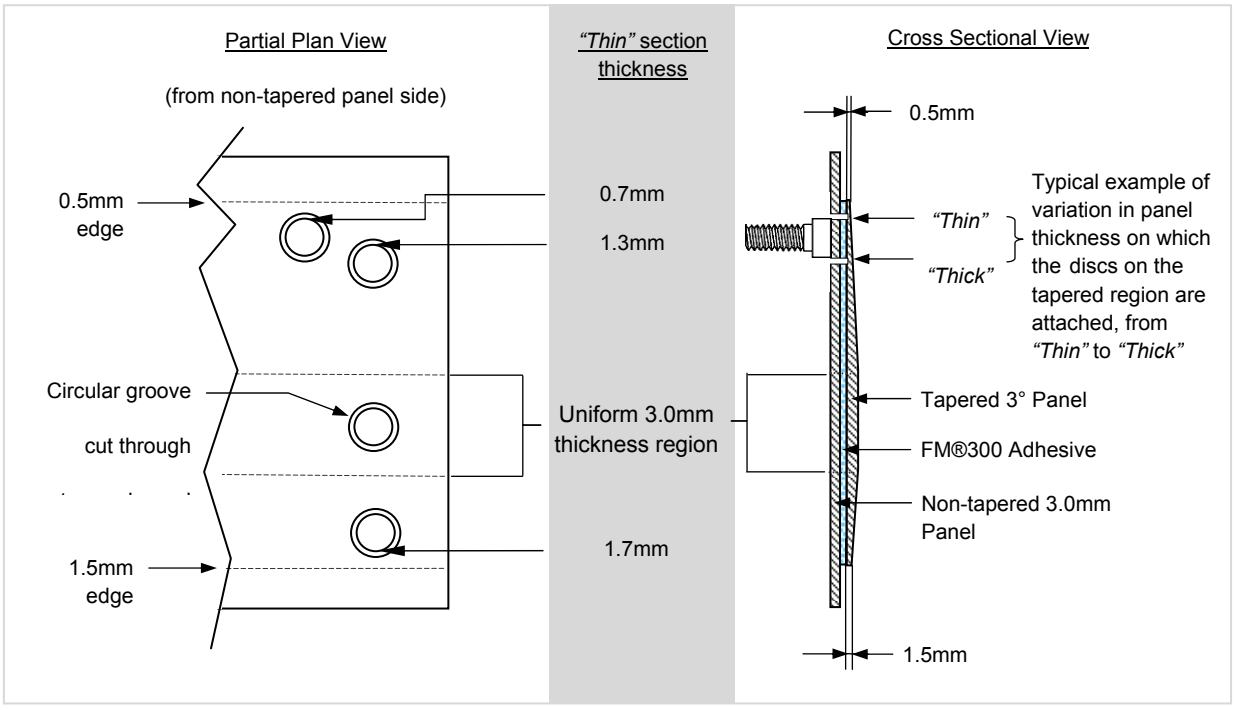

(a) (b)

Figure 3-6: a) Partial plan view from the non-tapered side of the bonded panels showing the layout of the circular grooves cut through the panel and the adhesive layer. b) Cross sectional view showing a typical circular groove cut through the non-tapered side of the bonded panel.

2 mm. The grooves were cut through the thickness of the adhesive layer to present each test disc system with equal opportunity to fail within the adhesive or at the interface as dictated by the strength of each system.

The grooves were cut at four different positions to allow the pull-test to be performed on structures of different thicknesses as shown in Figure 3-6. Each disc has a variation in patch thickness from *"thin"* to *"thick"* because the substrate thickness increases with distance from the edge. From hereinafter, the discs of the tapered configuration will be identified by the thinnest sections they were bonded to, which are 0.7 mm, 1.3 mm and 1.7 mm. Uniform thickness tests were only conducted on the thick part of the panel (3 mm).

Pull-stubs were then bonded onto the newly bored circular discs with the Hysol EA9309.3NA epoxy paste adhesive. The bonding surfaces of the stubs were scrubbed with Scotchbrite™ dampened with methyl ethyl ketone followed by scrubbing with deionised water and finally roughened by sanding with 180 grit Alumina paper. The bonded stubs were cured at room temperature for 72 hours.

PATTI tests were conducted at the rate of approximately 6.9 MPa/s (1 psi/s). The maximum pressure, P_B supplied into the gasket prior to the detachment of the Test-Disc (along with the stub) from the bonded panel was recorded. This pressure was converted to the tensile pull-off strength of the stub, σ_{PATTI} through Equation 3-1.

$$\sigma_{PATTI} = \frac{(P_B \times A_g) - C}{A_{TS}} \qquad \text{Eqn. 3-1}$$

A_g = contact area between Gasket and Reaction Plate

A_{TS} = Area of Test-Disc

C = Piston Constant

3.3 Fracture Toughness Measurements

The fracture toughness properties of the FM300 film adhesive are required to model the adhesive layers with the finite element technique using cohesive elements. The Mode I fracture toughness of the adhesive was measured using the double cantilever beam (DCB) specimens and the Mode II fracture toughness was measured through the end notched flexural (ENF) specimens. Both DCB and ENF specimens were made from aluminium alloy 2024 T3 grade of 3.2 mm thickness and were 25.4 mm wide. Three specimens were tested for each configuration.

3.3.1 Mode I – Double Cantilever Beam

The dimensions of the DCB specimens, with the exception of the adherend thickness, are according to the recommendation of ASTM D3433 [57]. The thickness of the adherend at 3.2 mm was deemed to be sufficient for aluminium alloy of 2024 T3 grade because its elastic limit was not exceeded when the same thickness was used with the FM300 adhesive for the Boeing wedge test according to ASTM D3762 [58, 59].

The bonding surfaces of the DCB specimens to be bonded with FM300 adhesive were prepared to Method B which is the same method used to prepare the tapered panels. The initial crack length and the corresponding load were measured during the DCB test to allow the Mode I fracture toughness of the adhesives to be calculated via Equation 3-2.

$$G_I = \frac{[4P^2(\max)][3a^2 + h^2]}{EB^2h^3} \qquad \text{Eqn. 3-2}$$

P (max) = Load to start crack

E = tensile modulus of the adherend

B = width of the adherend

a = initial crack length as measured from the loading points

h = adherend thickness

3.3.2 Mode II – End Notched Flexural Test

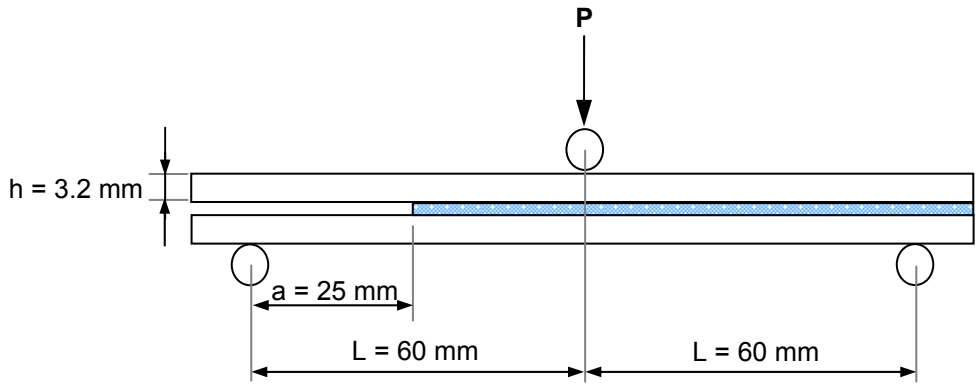

Figure 3-7: Test configuration of the ENF specimens

Due to the lack of any standardized procedure, the test configuration of the ENF specimens was adapted from the works of Liechti *et. al* .[26] given in Figure 3-7. The adherends of the ENF specimens were required to remain within its elastic limits. The bonding surfaces of the ENF specimens were prepared to Method B; the same method used for the tapered panels and the DCB specimens.

The Mode II fracture toughness of the adhesives was calculated via Equation 3-3 where the load and compliance, C (= $\frac{P}{d}$) were measured during the experiment. The compliance was taken from the initial linear region of the load-deflection curve of the specimens [60].

$$G_{II} = \frac{P^2}{8B^2h}\left[\frac{9a^2}{2E_f h^2} + \frac{0.9}{G_f}\right] \qquad \text{Eqn. 3-3a}$$

P = load when compliance deviates from linearity

B = width of the adherend

a = initial crack length

h = adherend thickness

E_f = effective Youngs modulus of adherend = $\frac{L^3 P}{4Bh^3 d}$ Eqn. 3-3b

L = span between supports

d = deflection at mid-support

G_f = effective shear modulus of adherend = $E_f \times \upsilon$ Eqn. 3-3c

υ = Poisson's ratio of adherend

The ENF specimens were subjected to three-point bending load until their compliance deviated from linearity. Unlike the DCB experiment, the crack propagation was not easily observed during the test. Nonetheless, since the crack tip was only required for the starter crack of the next measurement of the same ENF specimen, the specimen was unloaded and removed from the test configuration to allow a shim to be inserted between the adherends for the position of the crack tip to be determined. The insertion of the 1 mm thick shim did not cause any crack propagation in Mode I since the DCB tests have shown that the adherends had to be opened at least 1.5 mm before any crack propagation initiated.

4 Results

The results of the experiments described in Chapter 3 are presented in this chapter according to the same individual sub-sections as the experiments.

The fracture strengths and the fracture surfaces of the scarf and 90° / single lap-shear joints are presented in Section 4.1. This section is further divided according to the environmental conditioning of the joints. The pull-off strengths for the stubs bonded onto the tapered edge panels are presented in Section 4.2 along with the failure modes observed respectively on the panel-side and the stub-side. The fracture toughness measurements from the double cantilever beam experiment and end-notched flexural experiment are presented in Section 4.3.

4.1 Scarf Joint Results

4.1.1 Pristine (Dry) Conditions

By definition, cohesive failure within the adhesive layer leaves residues of adhesive on both sides of the fracture surface. Some cohesive failures occur at the mid-plane of the adhesive layer, involved tearing of the scrim cloth within the adhesive layer. This form of failure is considered as cohesive type failure in the work presented here because the scrim cloth does not contribute to the strength of the joint and its sole purpose is to control the nominal thickness of the adhesive after curing. Interfacial failure, on the other hand leaves residues of adhesive only on one side of the fracture surface and exposes the metallic adherend surface on the other. A mixed cohesive-interfacial failure shows a combination of both types of failure within the same joint.

The typical fracture surface mode for each joint type is shown in Figure 4-1a to d. The tight knit weave of the scrim cloth that could not previously be seen on the surface of the uncured adhesive are exposed on the fracture surfaces. The shallower angled scarf joints (up to 30°) prepared by surface preparation Methods A and B failed in a cohesive mode. The joints prepared by surface preparation Method C showed mixed cohesive-interfacial failure, with up to 9% of fracture surface area being interfacial.

All the larger angled joints (from 60° onwards) prepared by surface preparation Method A showed cohesive failure. All the joints prepared by surface preparation Methods B and C showed mixed cohesive-interfacial failure. Large voids within the cohesive failure region were observed to penetrate to the interface of the 60° joint with surface preparation Method B.

Surface Preparation Method A	Surface Preparation Method B	Surface Preparation Method C
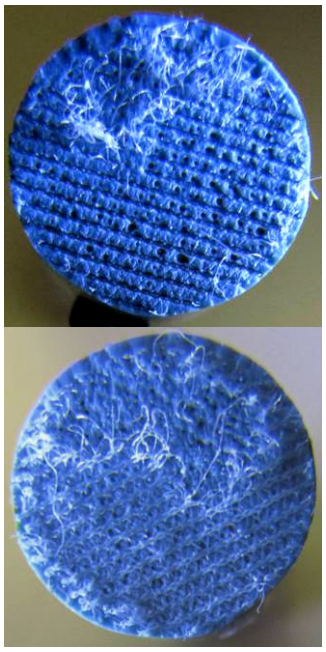	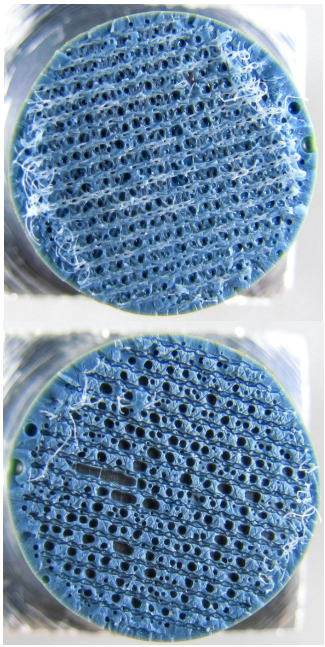	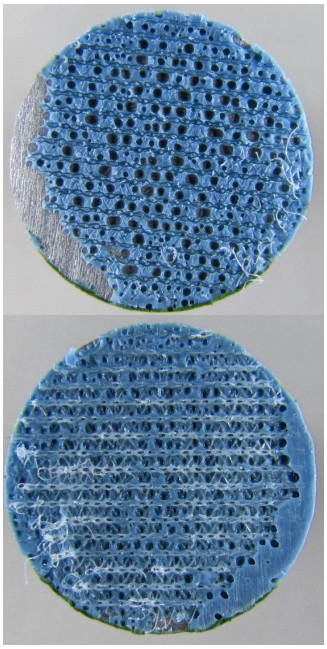
0°	0°	0°

Figure 4-1a: Typical fracture surfaces of the 0° scarf joints

Surface Preparation Method A	Surface Preparation Method B	Surface Preparation Method C
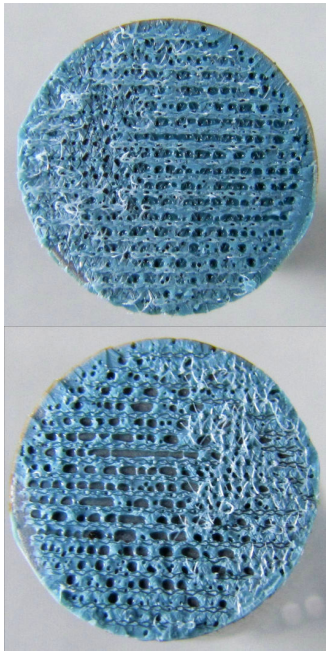	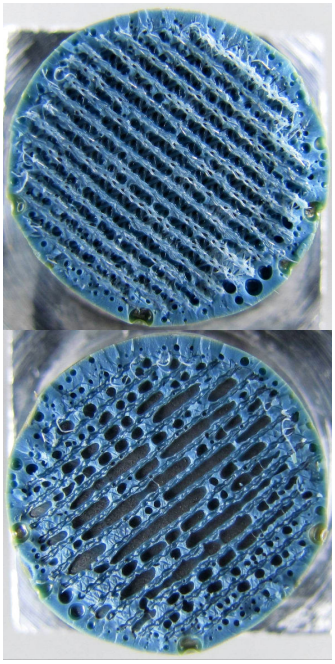	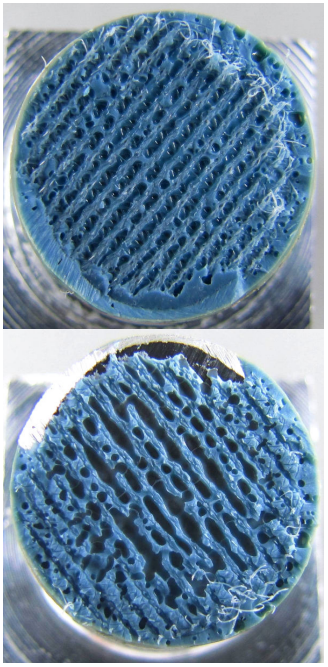
10°	15°	15°
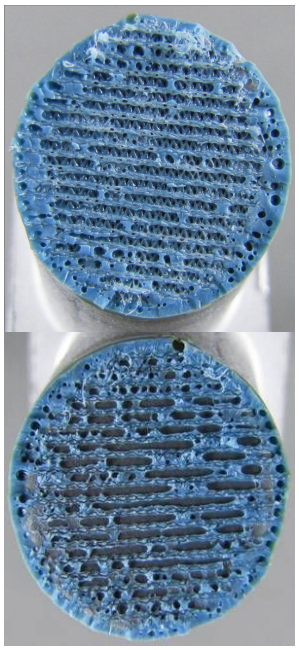	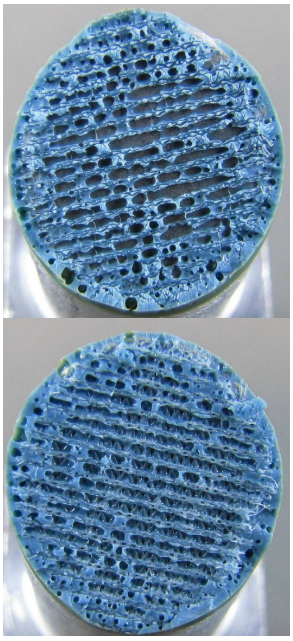	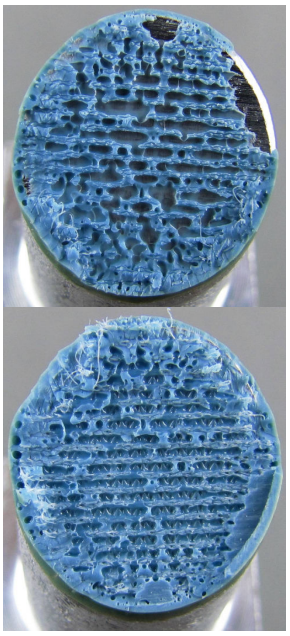
30°	30°	30°

Figure 4-1b: Typical fracture surfaces of the 10° to 30°scarf joints

Surface Preparation Method A	Surface Preparation Method B	Surface Preparation Method C
	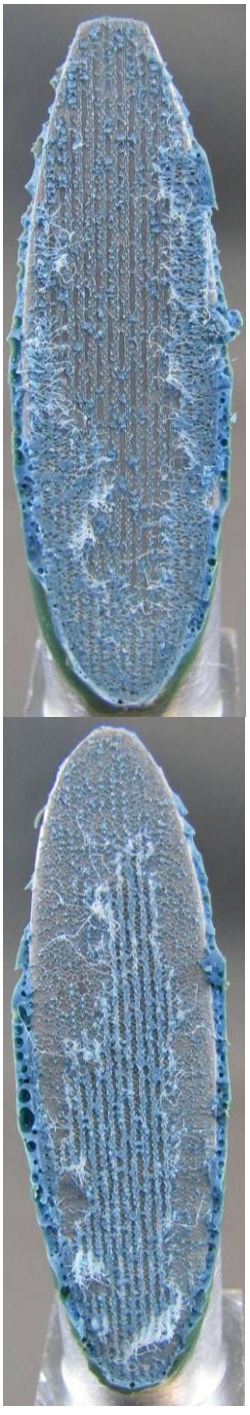	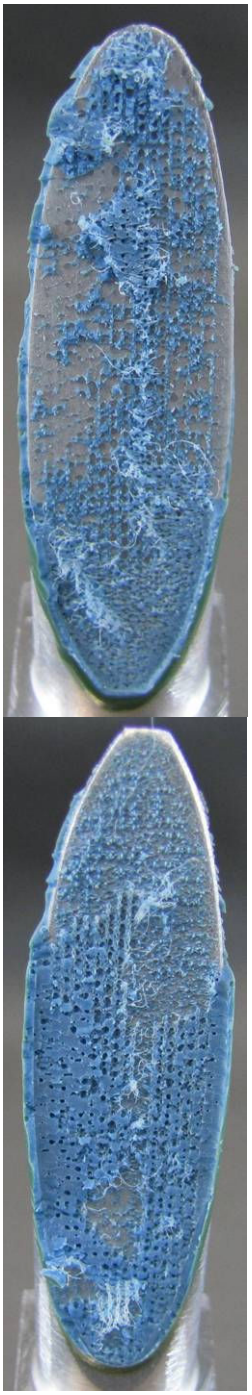
75°	75°	75°

Figure 4-1c: Typical fracture surfaces of the 75°scarf joints

Surface Preparation Method A	Surface Preparation Method B	Surface Preparation Method C
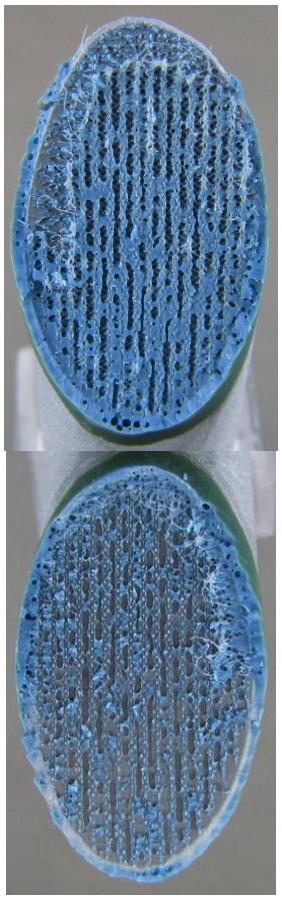 60°	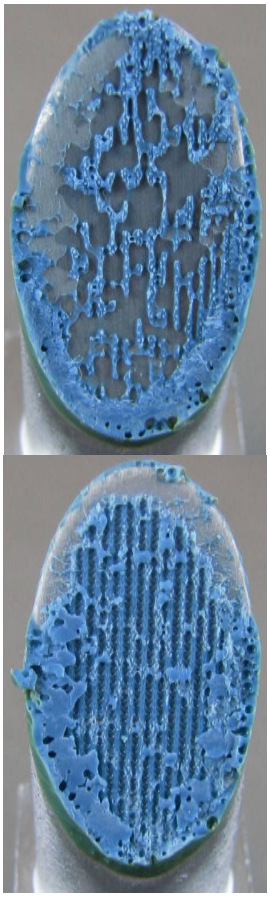 60°	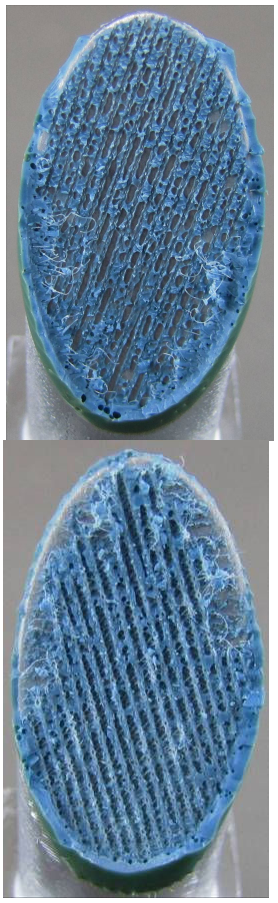 60°
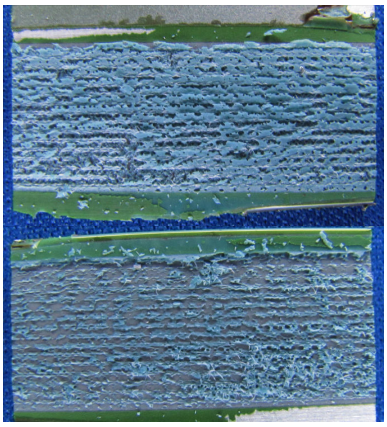 90° / SLS	 90° / SLS	 90° / SLS

Figure 4-1d: Typical fracture surfaces of the 60° scarf joints and the single lap-shear joints.

Figure 4-2 summarizes the failure mode for each surface preparation and joint type. The fracture surfaces of all the joints generally showed voids within the adhesive. These voids is the result of curing the joints under vacuum-bag pressurization, the main curing method for field repairs, instead of positive pressure by autoclave [29, 30]. The percentages voids, cohesive and interfacial fracture areas were measured by processing photographs of the fracture surfaces using the ImageJ software. The photographs were first reduced to their 8-bit format to convert the dominant colours on the fracture surfaces to black and white. The threshold of the black and white image was then manipulated to increase their contrast. Pixel scales were set by specifying the actual dimension of a particular feature in the processed image, ie. the diameter of the joint. The fracture surface area in the image was then selected and the areas of black and white particles were analysed and measured. The percentage areas of void measured on the fracture surfaces, ranging from 4 % to 29%, are also shown in Figure 4-2.

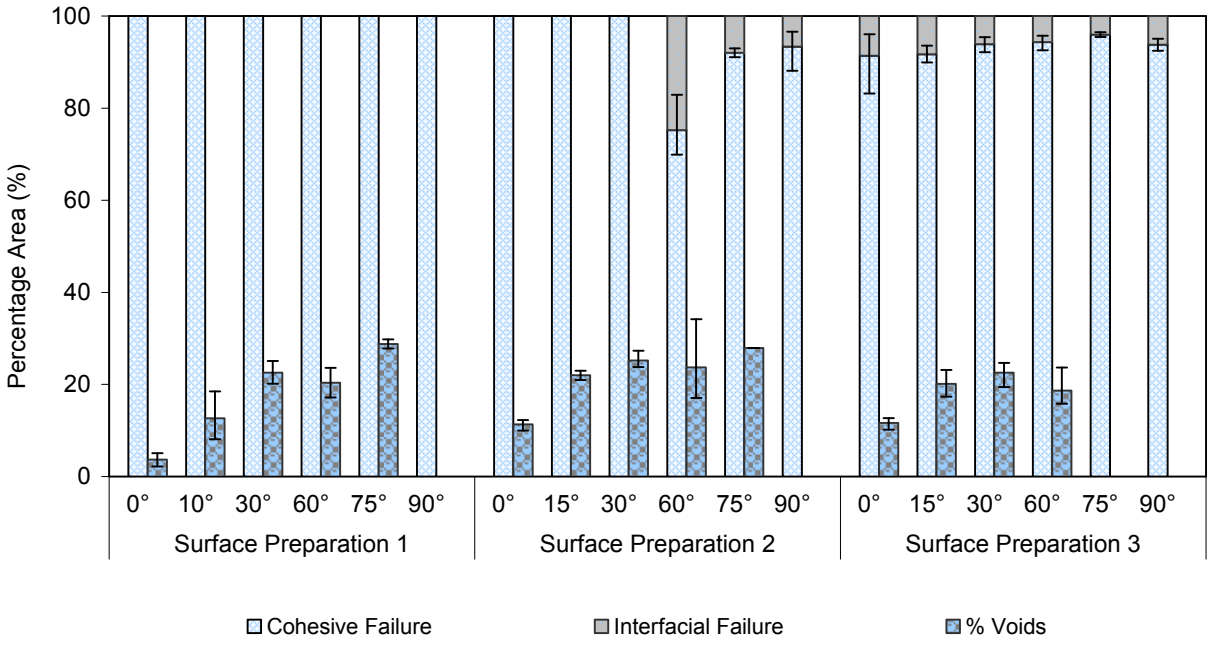

Figure 4-2: Failure mode of dry scarf and lap-shear joints and percentage voids on fracture surfaces.

Due to the scrim failure on some of the 75° and 90° / SLS joints, it was not possible to quantify the percentage area voids on the fracture surfaces of those joints. There were smaller percentage void content on the fracture surfaces of the single lap-shear joints because their configuration allowed a more uniform vacuum-bag pressure pressurization on the overlap lengths.

It is suspected that voids observed on the cohesive fracture surfaces will cause a reduction in fracture strength. To correct for this possible reduction, a void correction method was incorporated whereby the effective fracture stresses, σ_{eff} were calculated based on the net cross-sectional area after accounting for the percentage area voids, A_{void} % according to Equation 4-1. σ_{app} is the measured fracture stress.

$$\sigma_{eff} = \sigma_{app} \times \left(1 + \frac{A_{void}\%}{100}\right) \qquad \text{Eqn. 4-1}$$

This correction method can only be applied to voids on pure cohesive fracture surfaces and not joints with partial interfacial failure because interfacial bonds are able to withstand an unknown level of load [36].

Figure 4-3 compares the effective strengths for different angles and surface preparation methods. The shallower scarf joints prepared to Method C (without silane), exhibiting mixed cohesive-interfacial failure, had approximately 28% reduction in strength compared to joints prepared with silane that exhibited pure cohesion failure. This shows that the interfacial bond strength of the non-silane joints is weaker than the cohesive strength of the FM300 joints. Comparison of the fracture stresses across all surface preparation methods showed that the coefficient of variation was only 5.8% for the 60° joints and 8.4% for the 75° joints; showing that there is no significant correlation between the size of interfacial failure

area or void area to fracture stress or the surface preparation techniques. Method A yielded the highest strength results among all surface preparation methods.

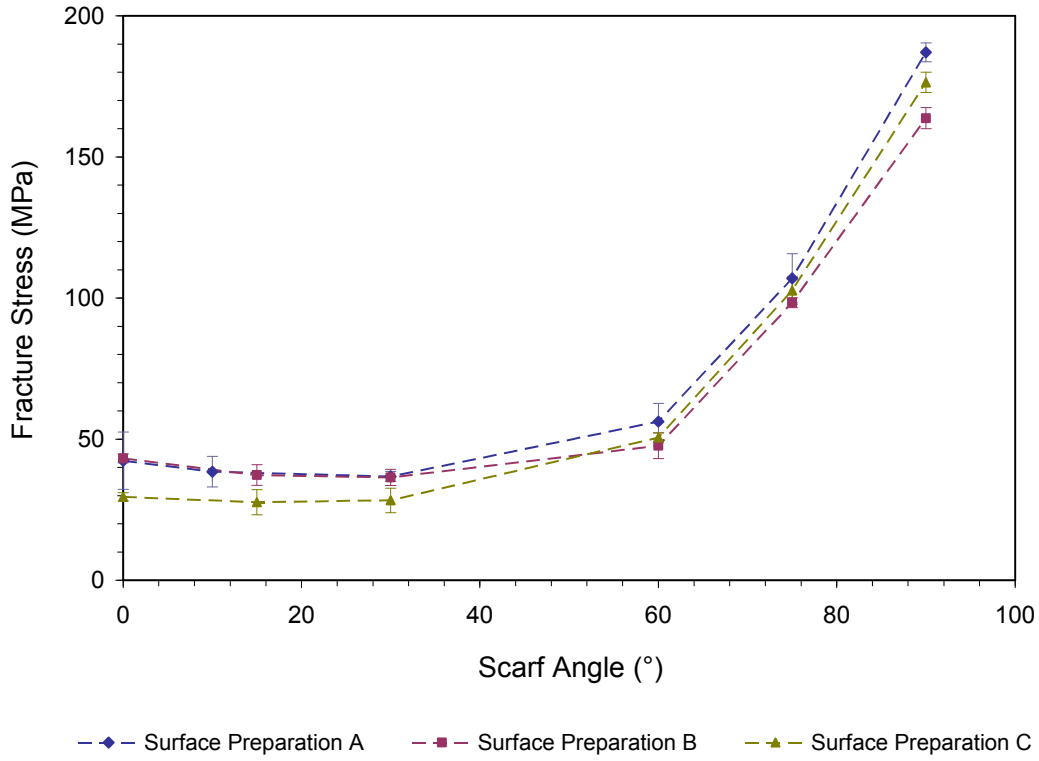

Figure 4-3: Effective fracture strength of scarf and single lap-shear joints after applying the void correction method

The fracture stresses of the single lap-shear joints (90°) with surface preparation Method B and Method C are within 13% lower than surface preparation Method A. The fracture stresses for the lap-shear joints in Figure 4-3 are the tensile fracture strength and were calculated by dividing the applied tensile load with the cross-sectional area formed by the adherend thickness. These values are required to determine the proportion of von Mises and hydrostatic stress components affecting the yield of the lap-shear joints in Section 6.2. The shear strength measurements of the lap-shear joints given in Table 4-1 are consistent with the values reported by other workers [30, 61].

Table 4-1: Shear strength measured from single lap-shear joints according to different surface preparation technique

Surface Preparation Method	Average (MPa)	Coefficient of Variation
A	27.52	3.32
B	24.38	3.89
C	23.68	0.92

The warping motion common to the flexing of the thin adherends was observed when the single lap-shear joints were loaded. This indicates that there were stresses acting within the adhesive which could lower the fracture strength [20, 21]. A method to account for the peeling stresses affecting the single lap-shear joint and to determine the ultimate shear strength of the adhesive will be presented in Section 6.2.

The strength of the steeper scarf joints and lap joints with surface preparation Method B are lower than those of surface preparation Method A and even Method C. It is suspected that the film of silane on the interface did not interact as intended with the FM300 adhesive and caused the reduction in strength for the joints prepared according to Method B. This film gave the interface of the joints a darker '*wet*' appearance as shown in fracture surface of the 60° joints.

Although silane generally improves the strength and durability of the joints, excessive thickness of silane on the bonding surfaces can be detrimental to the strength of the joint. This is caused by the reduced amount of hydroxyl bonding between the silane and substrate [62] when the thickness of the silane layer increases. It was suspected that the excessive thickness of silane on the steeper joints (60° onwards) with surface preparation Method B had caused them to fail at lower loads due to their mixed cohesive-interfacial fracture mode.

4.1.2 Hot and Wet Conditions

All the conditioned joints with silane (surface preparation Method A) failed cohesively. The voids observed on the fracture surfaces were relatively small and lesser in quantity compared to those on the cohesive fracture surfaces of joints without silane (surface preparation Method C) as shown in Figure 4-6a to c. Mixed cohesive-interfacial failure was observed on the fracture surfaces of the conditioned joints without silane.

Surface Preparation Method A	Surface Preparation Method C
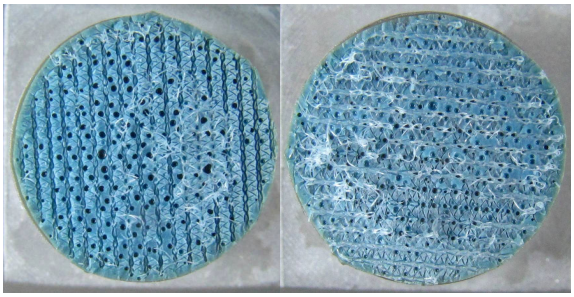	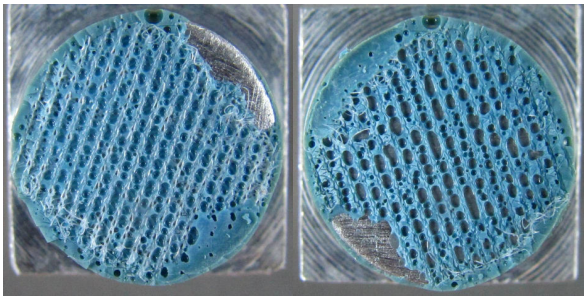
0°	0°
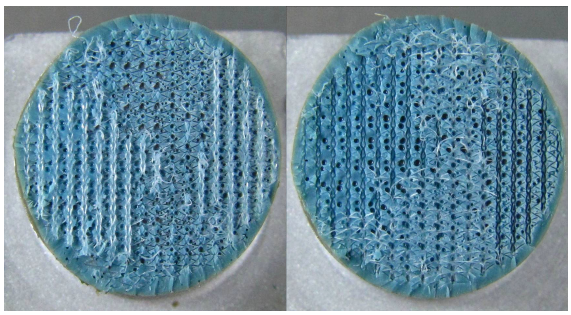	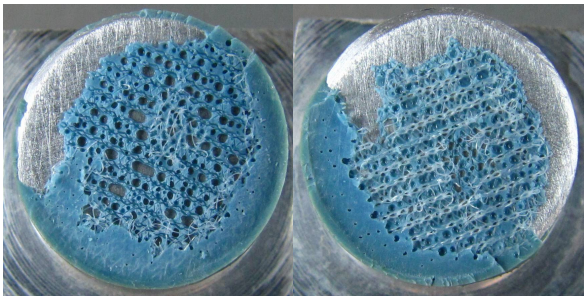
15°	15°

Figure 4-4a: Typical fracture surfaces of the conditioned 0° and 15° scarf joints

Surface Preparation Method A	Surface Preparation Method C
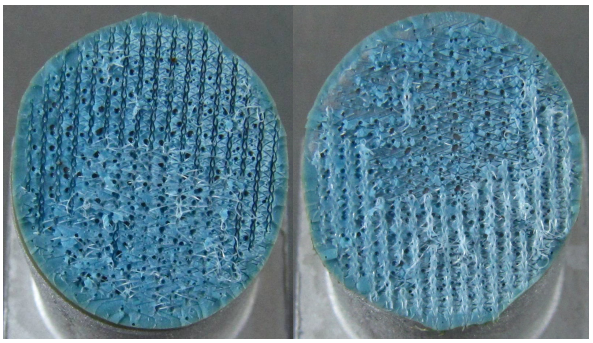	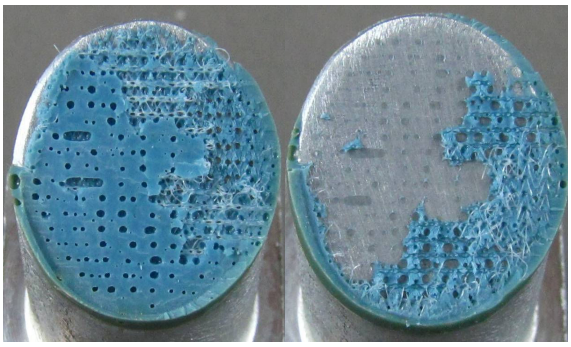
30°	30°
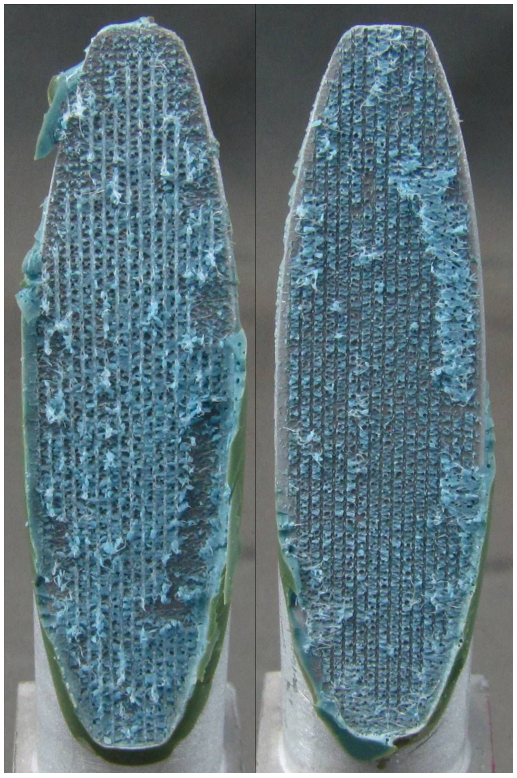	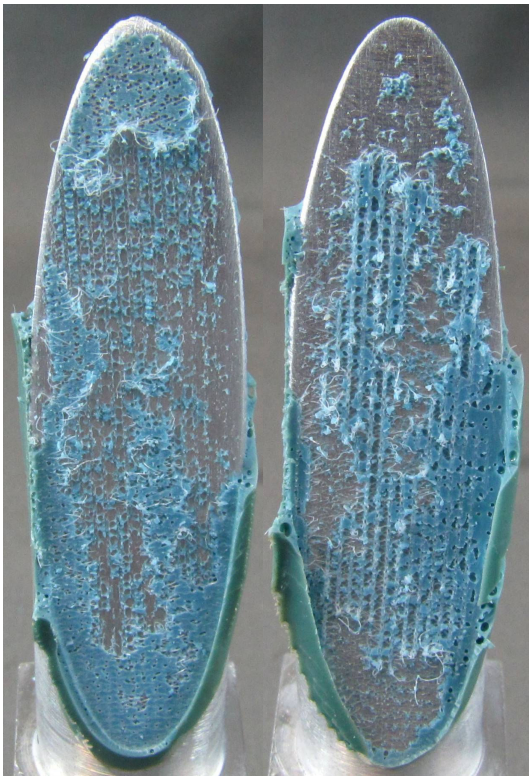
75°	75°

Figure 4-4b: Typical fracture surfaces of the 30° and 75° conditioned scarf joints.

Surface Preparation Method A	Surface Preparation Method C
 60°	 60°
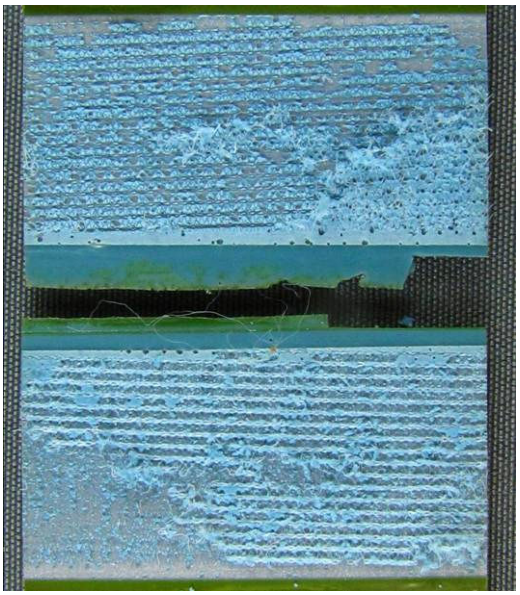 90° / SLS	 90° / SLS

Figure 4-4c: Typical fracture surfaces of the 60° conditioned scarf joints and single lap-shear joints

The percentage area voids on the conditioned joints prepared to Method A were less than their dry joints and only covered 4% to 5.2% of the fracture surfaces as shown in Figure 4-5. The reduction in voids is attributed to the additional B-staging procedure on the adhesive prior to curing. The scrim failure on the 75° and lap-shear joints made it difficult to quantify

the percentage area voids on their fracture surfaces. The percentage area of voids on the conditioned joints with surface preparation Method C were not measured since all of them showed mixed cohesive-interfacial failure and the void correction method cannot be applied to them. The effective stresses for conditioned joints showing pure cohesive failure were calculated according to Equation 4-1 given in Section 4.1.1.

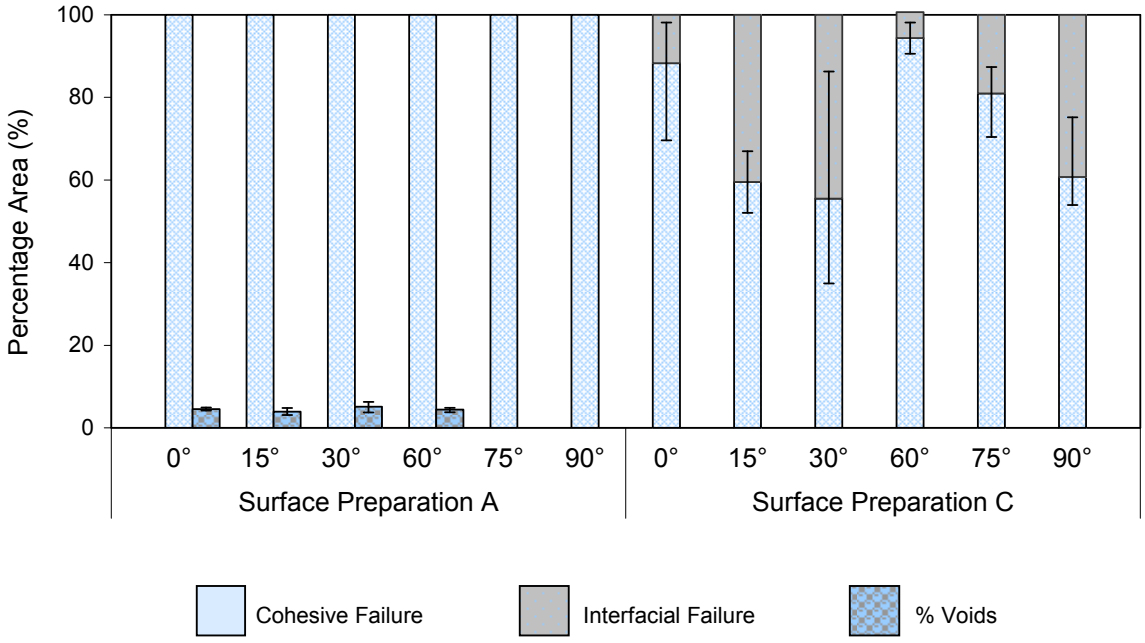

Figure 4-5: Failure mode of conditioned scarf and lap-shear joints and percentage voids on fracture surfaces.

Up to 60°, the conditioned joints with silane (Method A) exhibited very similar strength as the dry joints as shown in Figure 4-6a. This indicates that the void correction method is successful in accounting for the strength differences caused by the voids and that wet conditioning has no influence for surface preparation Method A. For larger angles, the wet joints show a higher strength. This indicates that B-staged adhesive performs better under shear loading conditions.

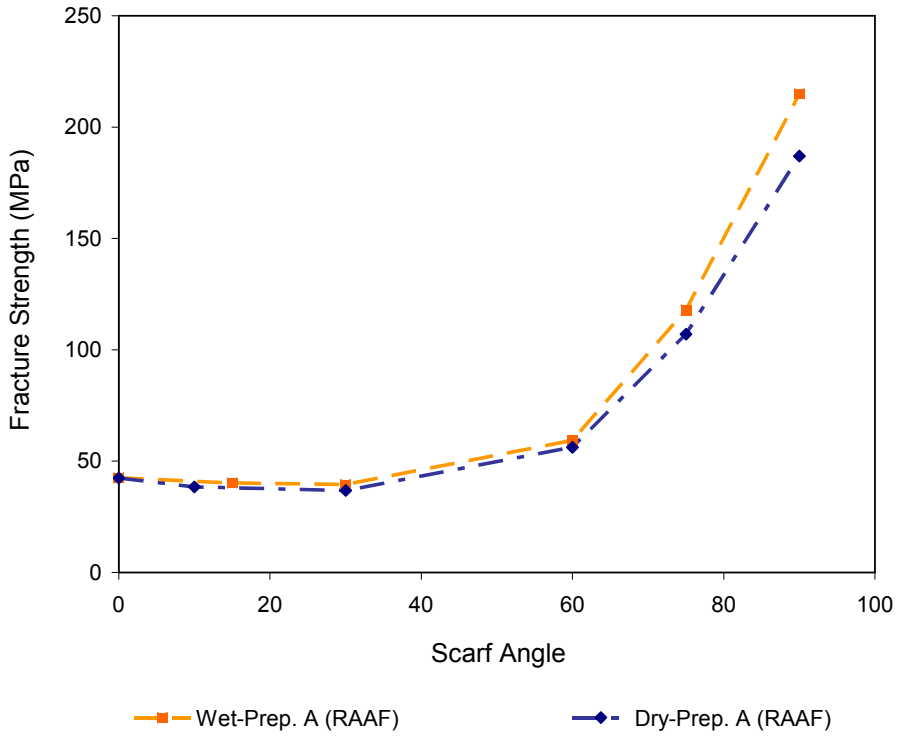

(a)

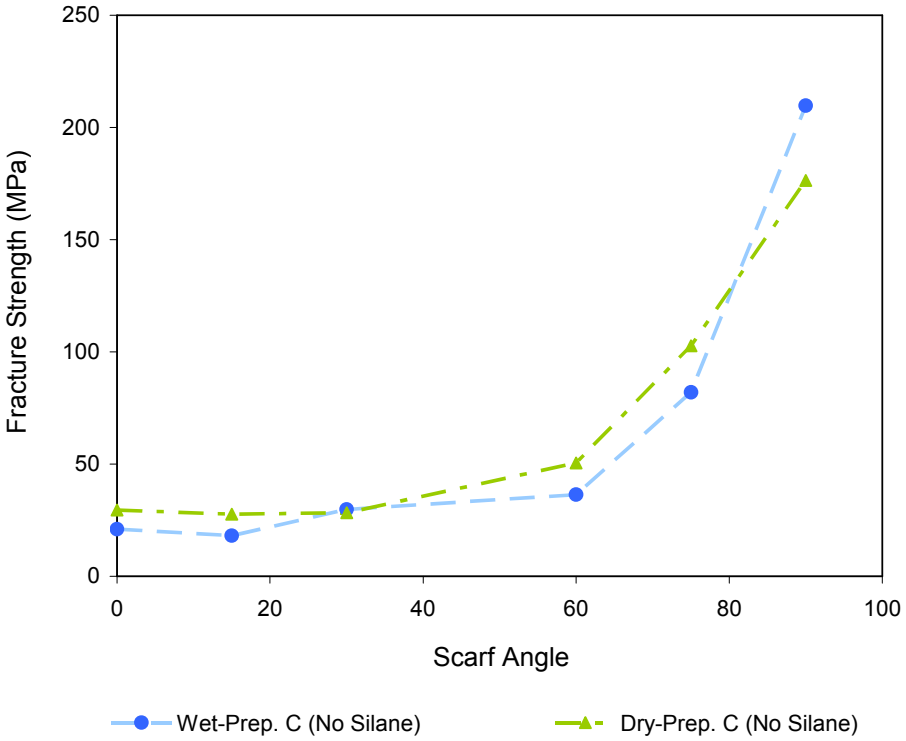

(b)

Figure 4-6: Comparison between the fracture strength of conditioned (wet) and dry joints with a) surface preparation Method A and b) surface preparation Method C.

Aside from the 30° joint, the conditioned scarf joints without silane (Method C) exhibit reduction in strength compared to their dry batch counterpart as shown in Figure 4-6b. The cause for the rise in strength for the 30° joints is unknown. The conditioned joints had larger areas of interfacial failure than the dry joints which show that an increase in percentage interfacial failure does cause a reduction in fracture strength although the exact correlation between them is yet again not explicitly expressed. This seems to shows that the strength contribution of these interfacial areas varies from case to case. It was not possible to gauge the strength of interfacial failure because none of the scarf or lap-shear joints in both dry and hot-wet conditions failed purely by interfacial failure.

The conditioned lap-joints without silane did not undergo significant strength reduction compared to those prepared to Method A. This suggests that the failure of the conditioned FM300 adhesive is more sensitive to tensile than shear loads.

4.2 Tapered Edge Panel PATTI Results

The tensile pull-off strengths converted from the maximum pressure supplied to the gasket of the PATTI tester are presented in Figure 4-7. The results show that the nominal tensile strength increases with substrate thickness. In particular, increasing the panel thickness from 0.7 mm to 1.3 mm raised the PATTI pull-off strength by almost 100%. However a further 30% increase of panel thickness from 1.3 mm to 1.7 mm only resulted in a 20% rise in pull-off strength. Increasing the thickness from 1.7 mm to 3.0 mm only increased the strength by 19%.

Cohesive failures were mainly observed for test discs pulled off the 3.0 mm and 1.7 mm adherend sections as shown in Figure 4-8a and b. PATTI tests on the 1.3 mm and 0.7 mm regions resulted in mixed cohesive-interfacial failures as shown in Figure 4-8c and Figure 4-8d. It is seen that interfacial failure on the 1.3 mm section covered up to 38% of the fracture

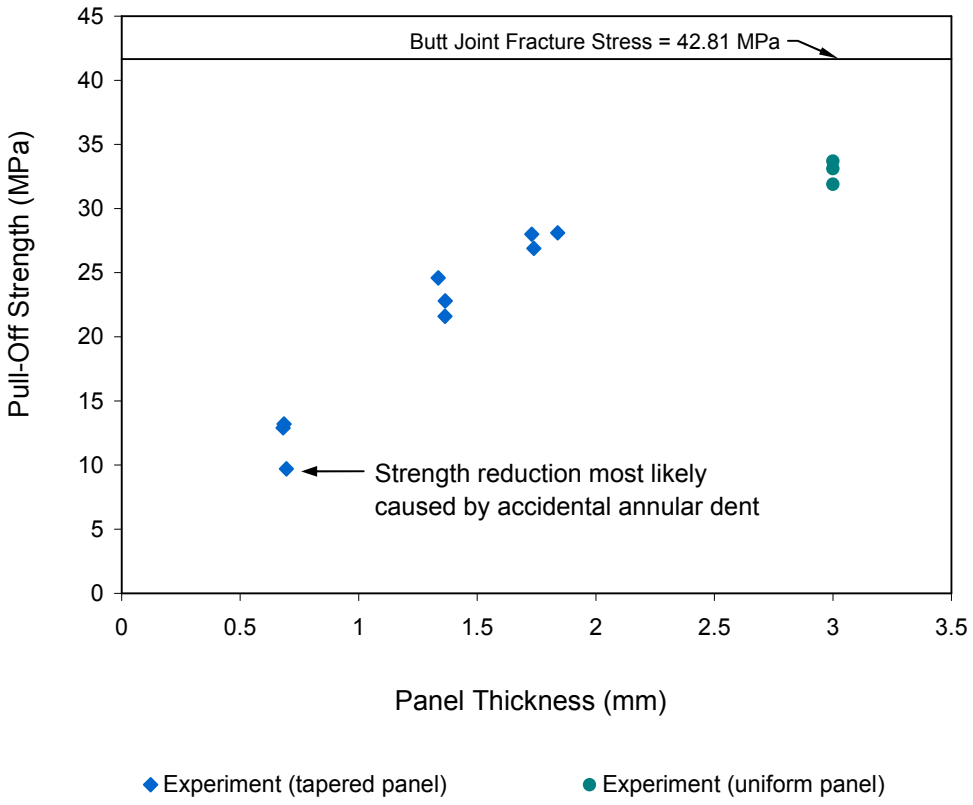

Figure 4-7: Nominal pull-off strength across different underlying panel thickness.

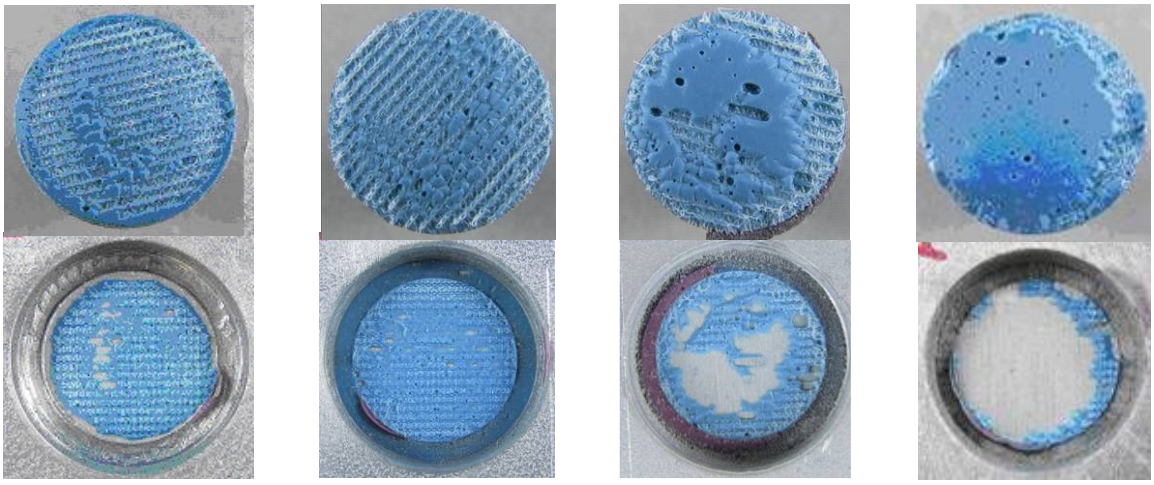

(a) (b) (c) (d)

Figure 4-8: Typical fracture surfaces on the stub-side and panel side of the (a) 3.0 mm uniform section and (b) 1.7 mm (c) 1.3 mm (d) 0.7mm tapered sections of the bonded tapered panel after PATTI testing. The left-hand side of the fracture surfaces shown in the bottom row correspond to the '*thin*' region of the tapered panels.

surface, while a much higher percentage of interfacial failure, approximately 75%, was observed on the stubs pulled off the 0.7 mm sections.

The bonded panels employed in this investigation were not subjected to any form of environmental degradation and the surface preparation method used on the bonding surfaces had previously produce cohesive fracture surfaces when subjected to tensile load. The present results suggest that the lower bond strength and greater level of interfacial failure near the tapered edge are due to the flexural deformation of thin panels.

It was noted that an annular dent corresponding to the hole-cutter used to bore the circular groove was unintentionally introduced onto the tapered panel. The pull-off strength at this particular location indicated in Figure 4-8 was 28% lower than the average strength of other tests on the 0.7 mm sections. This most likely strained the bond and introduced a partial debond into the test disc system. It was also observed that none of the tensile strength measured using the PATTI on panels up to 3.0 mm thick reached the tensile strength of butt joints, indicating that even moderately thick panels of 3.0 mm in thickness are still not approaching the infinitely thick limit.

4.3 Fracture Toughness Measurements

4.3.1 Mode I Fracture Toughness

The crack growth was monitored using a 10× magnification USB camera. Although the crack propagated intermittently through the adhesive and the interface, there was no marked change in the measured load or crack length. This seems to indicate that the interfacial bond strength is similar to the cohesive strength of the adhesive when subjected to Mode I loading despite the fact that cracks tend to propagate along the weaker bond path when a joint is loaded.

The Mode I fracture toughness of the adhesive was averaged from five measurements and presented in Table 4-2. This measured toughness is lower than the values measured by Liecthi *et. al.* [26] at 1.12 N/mm and Tenchev *et. al.* and other workers [63, 64] at 1.33 N/mm.

Table 4-2: Mode I fracture toughness of adhesives

Adhesive	Average (N/mm)	Standard Error
FM300	0.81	0.11

4.3.2 Mode II Fracture Toughness

The cracks were noted to propagate within the adhesive layer. The Mode II fracture toughness of the FM300 was averaged from five measurements and given in Table 4-3. The measured toughness is higher than the averaged values of 1.40 N/mm measured by Liecthi *et. al.* [26] but lower than the 5.0 N/mm value reported by Tenchev *et. al.* [63].

Table 4-3: Mode II fracture toughness of adhesives

Adhesive	Average (N/mm)	Standard Error
FM300	3.81	0.09

5 Finite Element Modelling

Finite Element models of the scarf and lap-shear joints were built in MSC.Patran™ to verify the yielding behaviour of the FM®300 adhesive. These models were used to obtain the normalised von Mises stress and hydrostatic pressure components within the adhesive layer through the elastic stress analyses in Section 5.1.3. The modified Drücker-Prager/Cap plasticity material in Section 6.2 was also validated with these models.

While the tensile butt-joint (0°) could be simplified to an axisymmetrical model, the scarf joints had to be analysed using three-dimensional (3D) models because the area of the bond surface changes from circular to elliptical when the scarf angle increases. Consequently, the three-dimensional (3D) tensile butt joint was constructed in addition to the axisymmetric slice model because its cross-sectional meshing formed the base mesh for the other scarf joints.

The aluminium alloy sections in all the models were only assigned with linear elastic properties from the literature [65-67] since the adhesive bonds would fail well before the elastic yield limit of the substrate is exceeded; subsequent analyses confirmed that the aluminium alloy section remained elastic at the time of joint failure. The boundary conditions for the tensile butt joint and the scarf joint models were set to emulate the experimental test conditions. The nodes on the bottom face of the lower aluminium stub were constrained in all directions. Surface loads were then applied to the top face of the upper aluminium stub for all the analyses.

Most of the adhesive shear strengths reported in the manufacturer's datasheets are quantified via the thick adherend lap shear joint because its geometry does not undergo as much eccentric loading as the single lap-shear joint and therefore produces more uniform

shear stresses along the bondline. Since the strain value used in the failure criterions of this project was taken from the manufacturers' datasheet [56], it was of interest to have a thick adherend lap shear joint model to provide a better understanding of the stress distribution within the bond. Instead of constructing a new model, additional boundary conditions were imposed onto the existing single lap-shear joint to emulate the same geometrical constraints imposed on the bond by the thick adherend lap-shear joint.

Finite Element models of the PATTI-tests were built in MSC.Patran™. Although three out of four of the panel experiments were conducted on the tapered edge, models with uniform underlying panel thicknesses were also developed because their geometry allows them to be modelled as axisymmetric which makes their computation more economical. Full 3D models of the tapered edge configuration were also built to compare the difference in predicted strength and strain distribution with the axisymmetric uniform panel models.

5.1 3D Scarf Joint Models

5.1.1 Geometry and Meshing

A two-dimensional (2D) mesh for the circular cross sectional area of the tensile butt joint shown in Figure 5-1 was constructed such that the mesh density was higher at the radial edge compared to the central region. The size of the elements at the edge was also kept uniform along the entire circumference. The mesh of the 2D cross-section was constructed with 4-noded quadrilateral elements. The radius of the circular section was 6 mm, corresponding to the experimental scarf joints.

The 2D mesh was extruded over a height of 20.6 mm to form 8-noded hex elements and was then removed from the 3D model. Of the total height, the lower and upper 10 mm formed

the aluminium alloy stubs and the 0.6 mm slice between them represents the adhesive as shown in Figure 5-2.

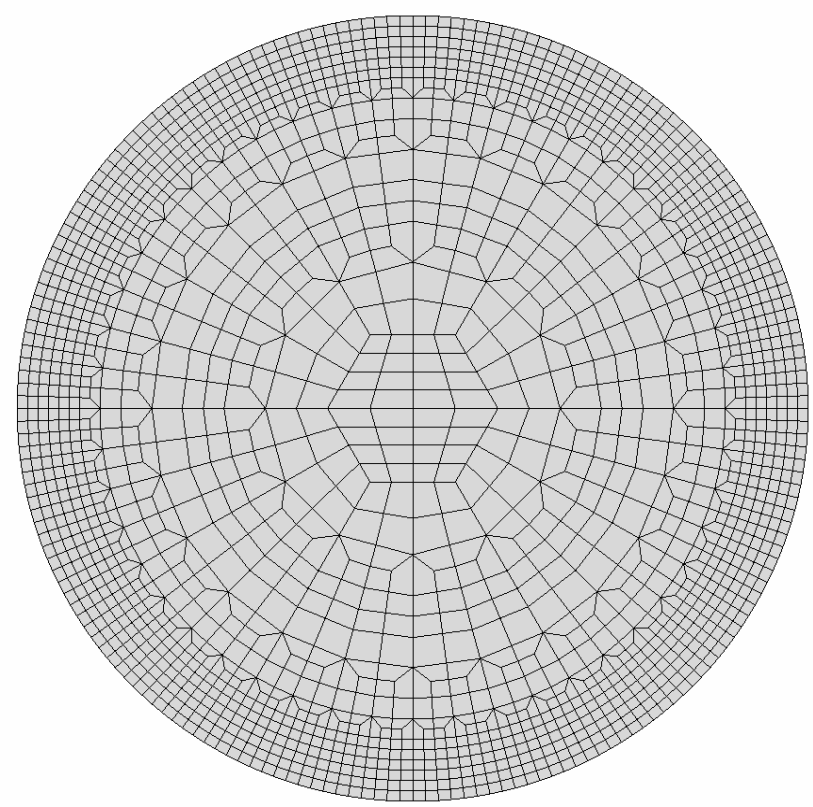

Figure 5-1: Cross sectional mesh for the tensile butt joint

The adhesive thickness was selected to be 0.6 mm in order to achieve the aspect ratio (adhesive diameter to thickness) of 20 as used by Adams et al. [10]. The adhesive thickness was subsequently divided into ten individual layers of elements. The aluminium alloy sections were divided into seven layers of elements with the height of the two immediate layers closest to the adhesive kept such that the edge elements were relatively cubic in shape. It was expected that any stress variation to be observed within the aluminium alloy sections would most probably occur close to the adhesive layer and that the stress further away would gradually become uniform.

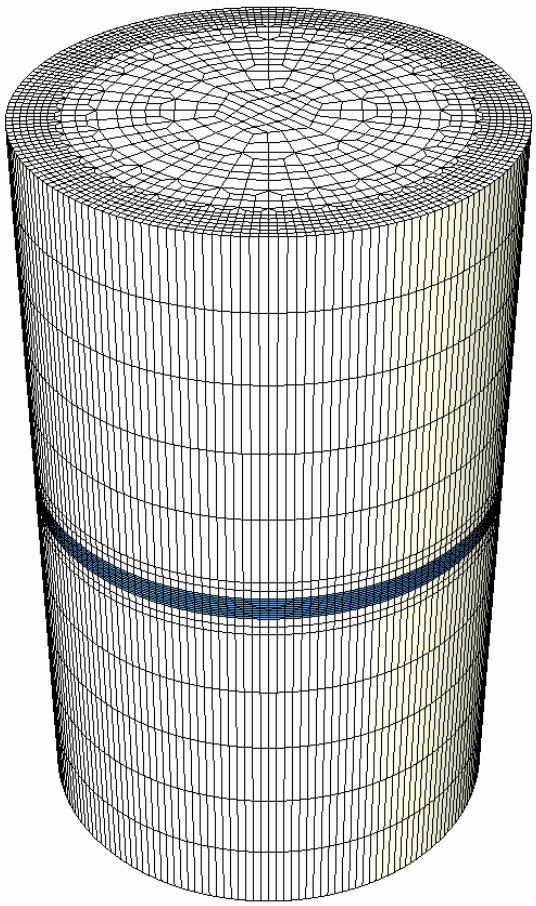

Figure 5-2: Three-dimensional model of the tensile butt joint. (The adhesive layer is represented by the blue section in between)

The angle bondline in the scarf joints shown in Figure 5-3 were created by tilting copies of the based 2D cross sectional mesh to 15°, 30°, 60° and 75°. The tilted meshes were scaled to the major diameters of the ellipses formed by each angle. The aluminium alloy sections were formed by lofting the original 2D mesh to the tilted joint angle mesh. For the steeper scarf joints (60° and 75°) intermediate tilted meshes were placed between them to regulate the height of the elements in the aluminium alloy sections. The adhesive sections were formed by lofting one of the tilted meshes to its replicate at a distance corresponding to the adhesive thickness. All the 2D tilted meshes were removed after the 3D models were formed. In order to save computation time, the models analysed were halved along their

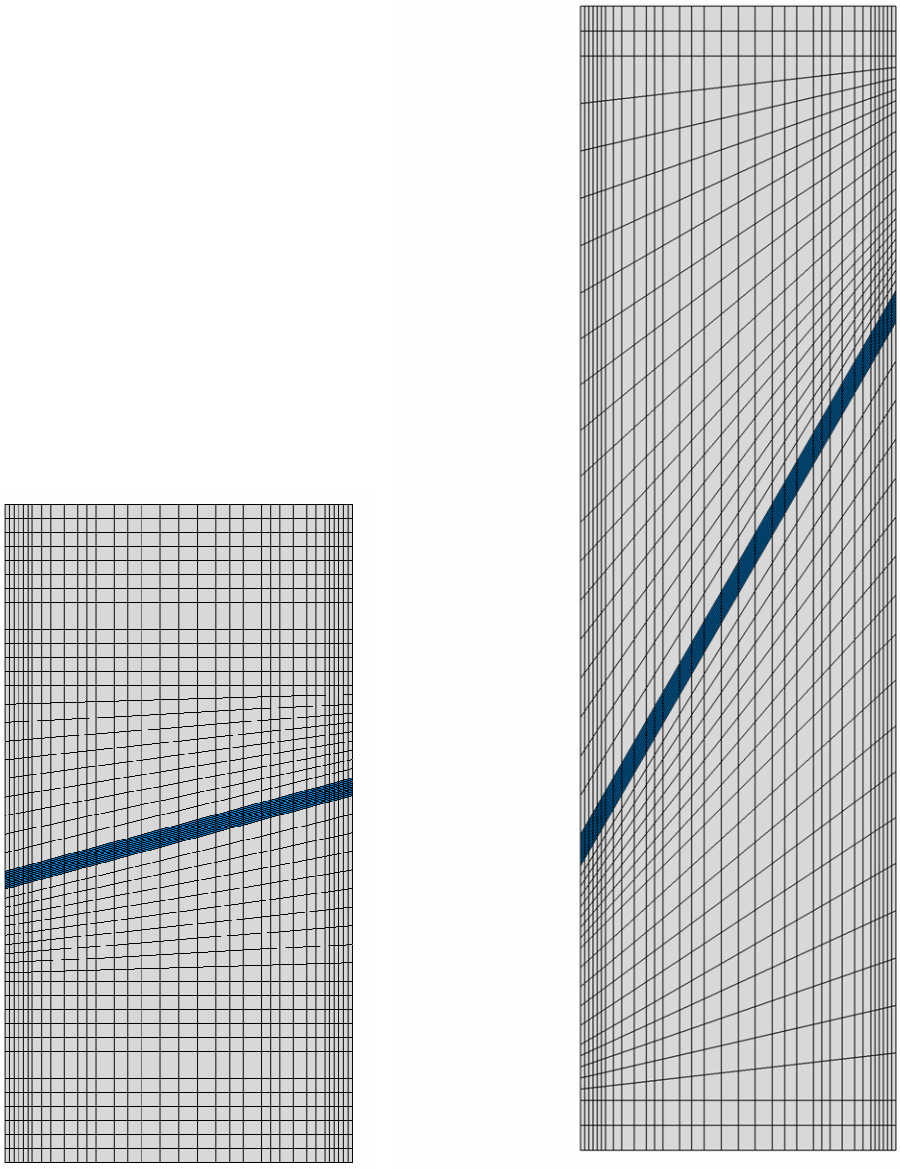

(a) (b)

Figure 5-3: Vertical cross-sectional view of the a) 15° and b) 60° scarf joint models

vertical plane of symmetry and the nodes on the *"cut-off"* surface were restrained in the direction normal to it.

Due to the scaling of the tilted mesh structure, the radial lengths of the edge elements had a maximum and minimum value as shown by the typical elliptical cross-sectional mesh in Figure 5-4. The minimum radial length for the elements in all the scarf models remained at

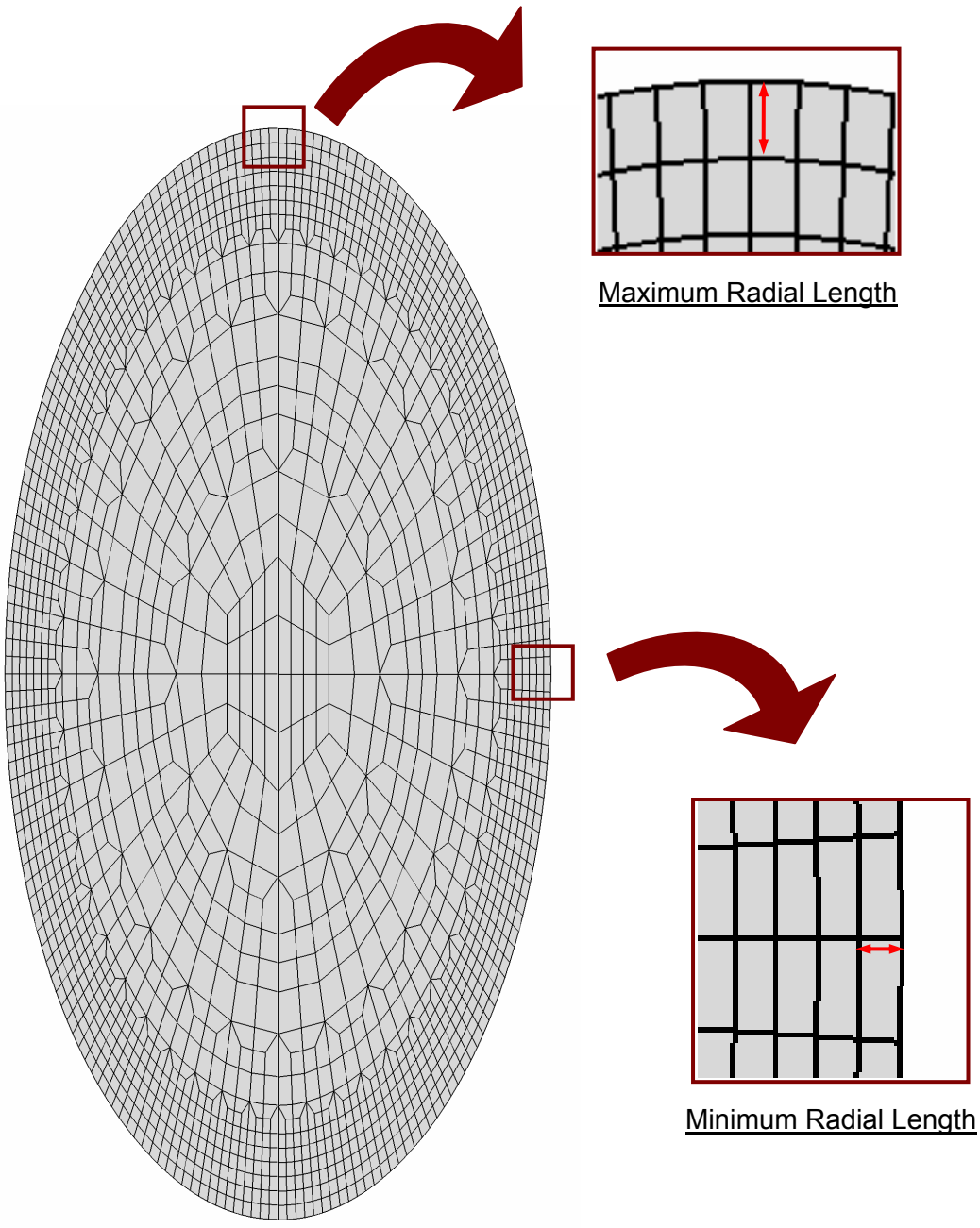

Figure 5-4: The origins for the maximum and minimum radial lengths of the elements due to scaling of the circular mesh in Figure 5-1 to the major diameters formed by the ellipses of each scarf angle

0.166 mm at the edge of the minor diameter. The maximum radial length varied at the edge of the major diameter for each scarf joint as listed in Table 5-1.

Table 5-1: Maximum length for the edge elements of the scarf joints

Scarf Angle (°)	Maximum Length (mm)
15	0.171
30	0.191
60	0.332
75	0.641

The difference in element lengths is highlighted because the element lengths of the scarf joint models have to be less than the characteristic distance calibrated to predict the strength of the joints. The maximum element lengths of the scarf joint models are less than the characteristic distance calibrated for the modified Drücker-Prager/Cap plasticity material in Section 7.3.1 which means that the material model can be employed to these models to predict the strength of the scarf joints. On the other hand, strength predictions cannot be performed when these joint models are assigned with the von Mises material because the characteristic distance calibrated for the material is less than the maximum element lengths.

5.1.2 Single Lap-Shear Joint Model

Although the stress distribution across the width of a lap-joint does not vary significantly, the 3D single lap-shear joint was constructed to be consistent with the 3D scarf models. The model was constructed from 8-noded solid hex elements and was used to obtain the normalized hydrostatic pressure and von Mises stress components within the adhesive layer. The size of the adhesive elements was kept uniform at 0.6 mm x 0.7 mm.

The aluminium alloy adherends were only modeled up to the edge of the grips in the tensile testing machine. As such, all the nodes on the cross sectional end on the left-hand side were constrained in all directions while the nodes on the right-hand end were restrained in the y and z-directions as shown in Figure 5-5a. Surface loads were applied on the right-hand end of the model. The adherend sections of the model were observed to warp in the y-direction like the experimental lap-shear joints when loaded. This warping motion induces peeling stresses within the adhesive layer and is represented by the hydrostatic pressure component.

The single lap-shear model was converted to represent a thick adherend lap joint by applying boundary conditions on the bottom surfaces of the left adherend and the top surface of the right adherend to prevent the warping motion as shown in Figure 5-5b.

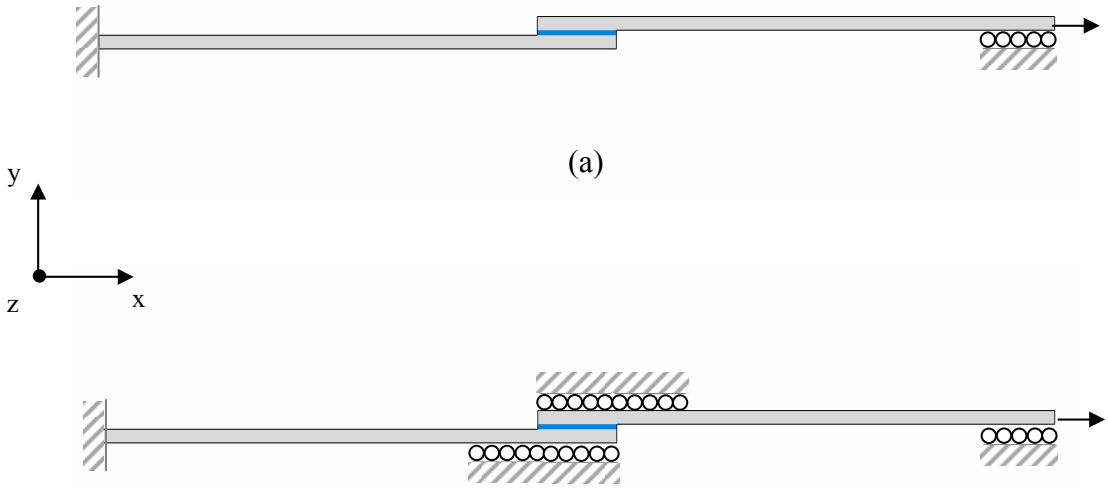

(a)

(b)

Figure 5-5: Boundary conditions applied to the a) single lap-shear model and b) thick adherend lap-shear model

5.1.3 Elastic Stress Analysis

A linear elastic analysis was performed on the 3D tensile butt joint model (0°) using the material properties [66, 68] given in Table 5-2 to verify that the mesh could adequately capture the stress distribution across the bondline. The stress components across the diameter of the joint shown in Figure 5-6 are in good correlation with the results by Adams et al. [10] except for the peak shear stress at the interface. The lower shear stress produced by the 3D tensile joint model is similar to the 2D plane stress model in the works of Alwar and Nagaraja [11]. Nevertheless, the mesh of the current tensile butt joint model was considered adequate since the overall stress distribution generated by both axisymmetric and plane stress models were closely matched.

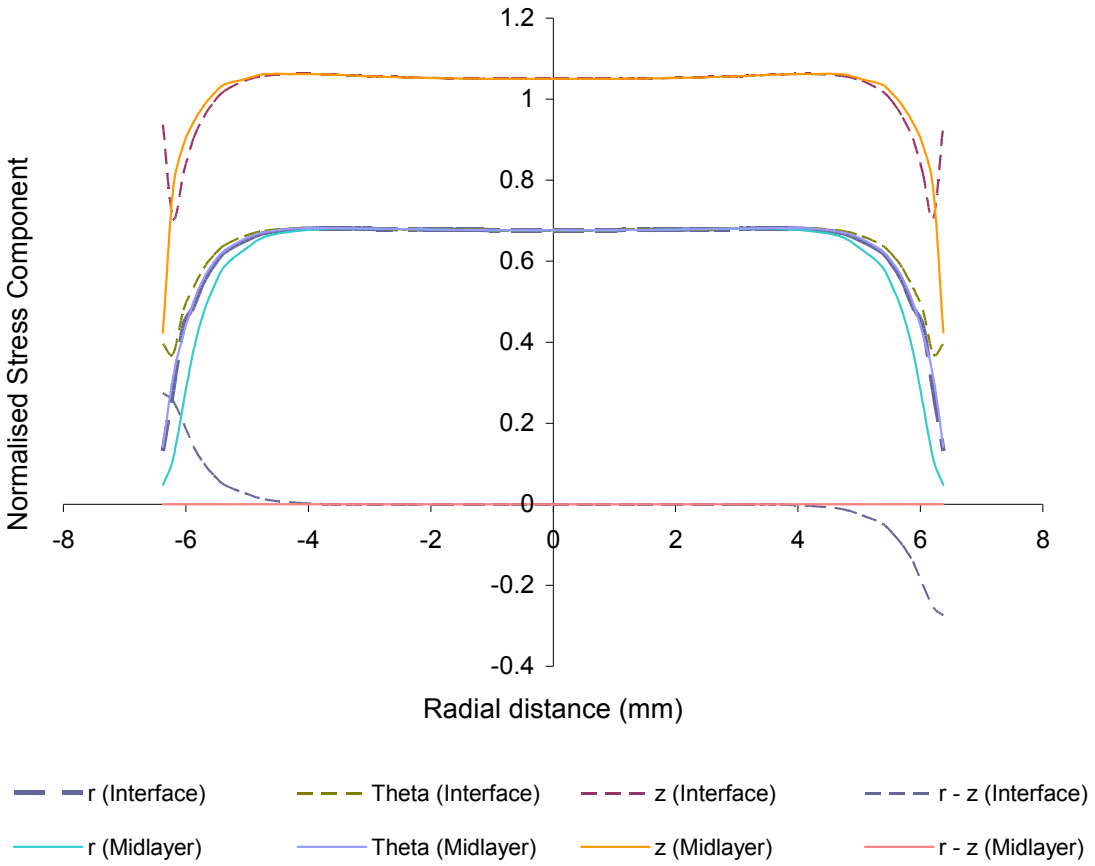

Figure 5-6: Stress distribution within the tensile butt joint where *r* represents the radial stresses and *Theta* represents the circumferential stresses in the cylindrical coordinate system

Table 5-2: Material properties for linear elastic analysis [66, 68]

Adhesive	Young's Modulus (MPa)	Poisson's ratio
Aluminium alloy	69500	0.33
FM300 adhesive	2280	0.36

The linear Drücker-Prager yield criterion relates the tensile and shear stress components affecting the yield of structural adhesive according to the linear function previously given by Equation 2-1 in Section 2.1.

$$\sigma_{vm} + m\sigma_m = \sqrt{3}\tau_0 \qquad \textit{Eqn. 2-1}$$

whereby σ_m is the hydrostatic pressure and σ_{vm} is the von Mises stress. The sensitivity of the adhesive to hydrostatic pressure is denoted by m and the shear yield stress is denoted by τ_0.

The von Mises and hydrostatic stress components with an infinitesimal block of adhesive within the central region of the scarf joints were calculated by assuming the coordinate and stress system shown in Figure 5-7. The applied stress, σ_{app} was resolved into the normal, σ_n and shear stress components, τ_n acting along the coordinate axes according to Equations 5-1 and 5-2 [69].

$$\sigma_n = \sigma_{app}\cos^2\theta \qquad \text{Eqn. 5-1}$$

$$\tau_n = \frac{1}{2}\sigma_{app}\sin 2\theta \qquad \text{Eqn. 5-2}$$

Due to the lateral constraint imparted by the stiff aluminium alloy stubs, the lateral tensile and shear strains were assumed to be zero as given in Equations 5-3 and 5-4.

$$\varepsilon_{x1} = \varepsilon_{y1} = 0 \qquad \text{Eqn. 5-3}$$

$$\tau_{xz} = \tau_{yz} = 0 \qquad \text{Eqn. 5-4}$$

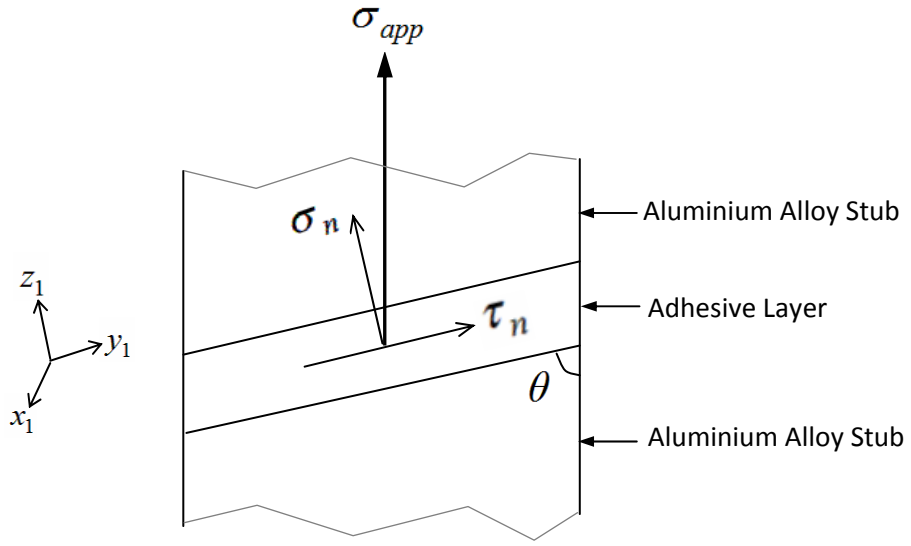

Figure 5-7**:** Orientation of stress vectors within adhesive of scarf joints.

Since the adhesive is an isotropic material, the stress components of the coordinate system defined above can be expressed in terms of σ_n and τ_n as follows:

$$\sigma_{z_1} = \sigma_n \ , \quad \sigma_{x_1} = \sigma_{y_1} = \frac{\nu}{1-\nu}\sigma_n \text{ and } \tau_{xy} = \tau_n \qquad \text{Eqn. 5-5}$$

The von Mises stress component, expressed in term of σ_{app} is derived from the normal stress components as follows:

$$\sigma_{vm} = \sqrt{\frac{\left(\sigma_{x1}-\sigma_{y1}\right)^2 + \left(\sigma_{y1}-\sigma_{z1}\right)^2 + \left(\sigma_{z1}-\sigma_{x1}\right)^2 + 6\left(\tau_{xy}^{\ 2} + \tau_{yz}^{\ 2} + \tau_{zx}^{\ 2}\right)}{2}} \qquad \text{Eqn. 5-6a}$$

$$= \sqrt{\frac{\left(\frac{\upsilon}{1-\upsilon}\sigma_n - \sigma_n\right)^2 + \left(\sigma_n - \frac{\upsilon}{1-\upsilon}\sigma_n\right)^2 + 6\tau_n^{\ 2}}{2}} \qquad \text{Eqn. 5-6b}$$

$$= \sqrt{\frac{\sigma_n^{\,2}\left[\left(\frac{2\upsilon-1}{1-\upsilon}\right)^2+\left(\frac{1-2\upsilon}{1-\upsilon}\right)^2\right]+6\tau_n^{\,2}}{2}} \qquad \text{Eqn. 5-6c}$$

$$= \sqrt{\sigma_n^{\,2}\left(\frac{2\upsilon-1}{1-\upsilon}\right)^2+3\tau_n^{\,2}} \qquad \text{Eqn. 5-6d}$$

$$= \sqrt{\left(\frac{2\upsilon-1}{1-\upsilon}\right)^2\sigma_{app}^2\cos^4\theta+\frac{3}{4}\sigma_{app}^2\sin^2 2\theta} \qquad \text{Eqn. 5-6e}$$

$$= \sigma_{app}\sqrt{\left(\frac{2\upsilon-1}{1-\upsilon}\right)^2\cos^4\theta+\frac{3}{4}\sin^2 2\theta} \qquad \text{Eqn. 5-6f}$$

The derivation of the hydrostatic stress component in term of σ_{app} is as follows:

$$\sigma_m = \frac{1}{3}\left(\sigma_{x1}+\sigma_{y1}+\sigma_{z1}\right) \qquad \text{Eqn. 5-7a}$$

$$= \frac{1}{3}\left(\sigma_n+\frac{2\upsilon}{1-\upsilon}\sigma_n\right) \qquad \text{Eqn. 5-7b}$$

$$= \sigma_{app}\times\frac{1}{3}\left(\frac{1+\upsilon}{1-\upsilon}\right)\cos^2\theta \qquad \text{Eqn. 5-7c}$$

The von Mises and hydrostatic stress components in Equations 5-6f and 5-7c are normalised by the applied stress to obtain their individual fractions when the joints were loaded. These normalised stress components are given in Equations 5-8 and 5-9 and are shown to be dependent on the loading angle and the Poisson's ratio of the adhesive.

$$\sigma_{vm}^N = \frac{\sigma_{vm}}{\sigma_{app}} = \sqrt{\left(\frac{2\upsilon-1}{1-\upsilon}\right)^2\cos^4\theta+\frac{3}{4}\sin^2 2\theta} \qquad \text{Eqn. 5-8}$$

$$\sigma_{vm}^N = \frac{\sigma_m}{\sigma_{app}} = \frac{1}{3}\left(\frac{1+\upsilon}{1-\upsilon}\right)\cos^2\theta \qquad \text{Eqn. 5-9}$$

The calculated values of the normalised stress components are plotted in Figure 5-8. The analytical solution presented above only calculates the stress components in the centre region of the adhesive. The calculation for the stress components at the edge region of the adhesive become a function of the lateral strains caused by Poisson's effect and the radial distance since the principal stresses diminish to zero at the edge.

Linear finite element analyses were performed on the 3D scarf joints using the material properties given in Table 5-2 to include the stress gradient at the edge of the adhesive into the normalised stress components. The normalised stress components were obtained by averaging the von Mises stress and hydrostatic pressure components in the midlayer of the adhesive when a unit surface load was applied on the joints. The normalised components for the single lap-shear joints were also obtained in a similar manner from the single lap-shear model. These normalised stress components were assumed to be the characteristic stresses

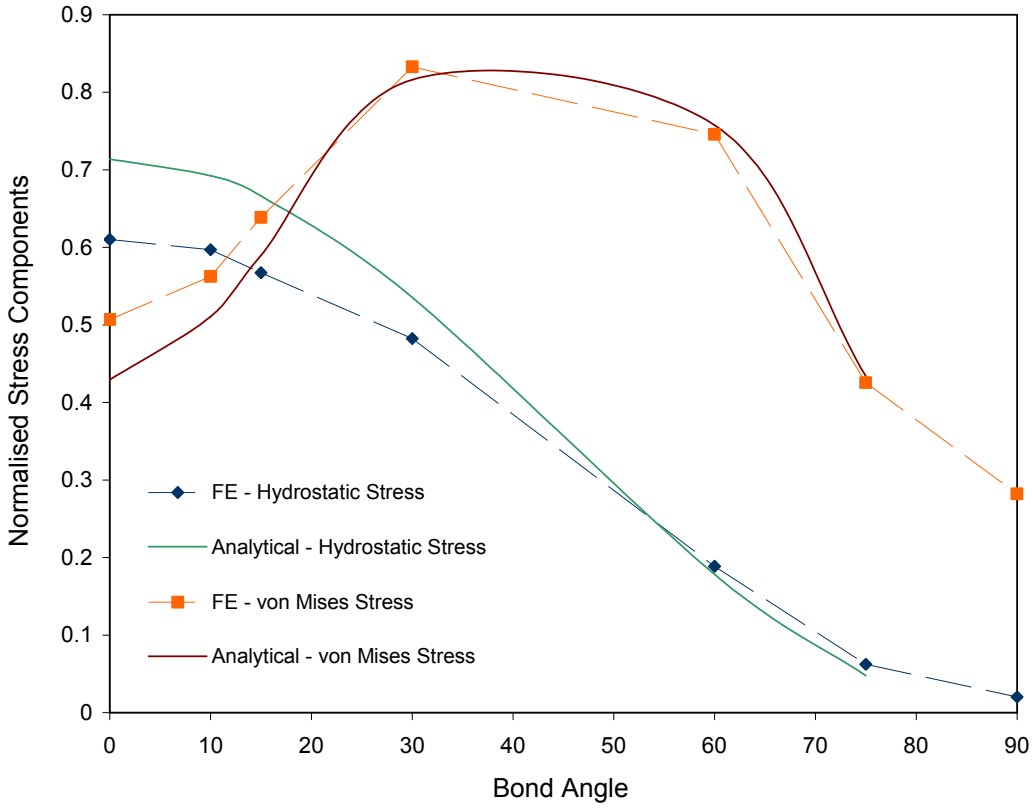

Figure 5-8: Normalised von Mises and hydrostatic stress components versus scarf angle.

affecting the yield of the adhesive and are plotted in Figure 5-8 for comparison with values obtained through the analytical solution.

As the scarf angle increases, the difference between the normalised stress values obtained through the analytical and FE method decreases. This difference is caused by stress gradient at the edge of the adhesive which was not taken in account by the analytical calculation. Figure 5-9 shows the stress distribution across the major diameters of some of the scarf models and the gradient between the edge and the central region decreases as the scarf angle increases.

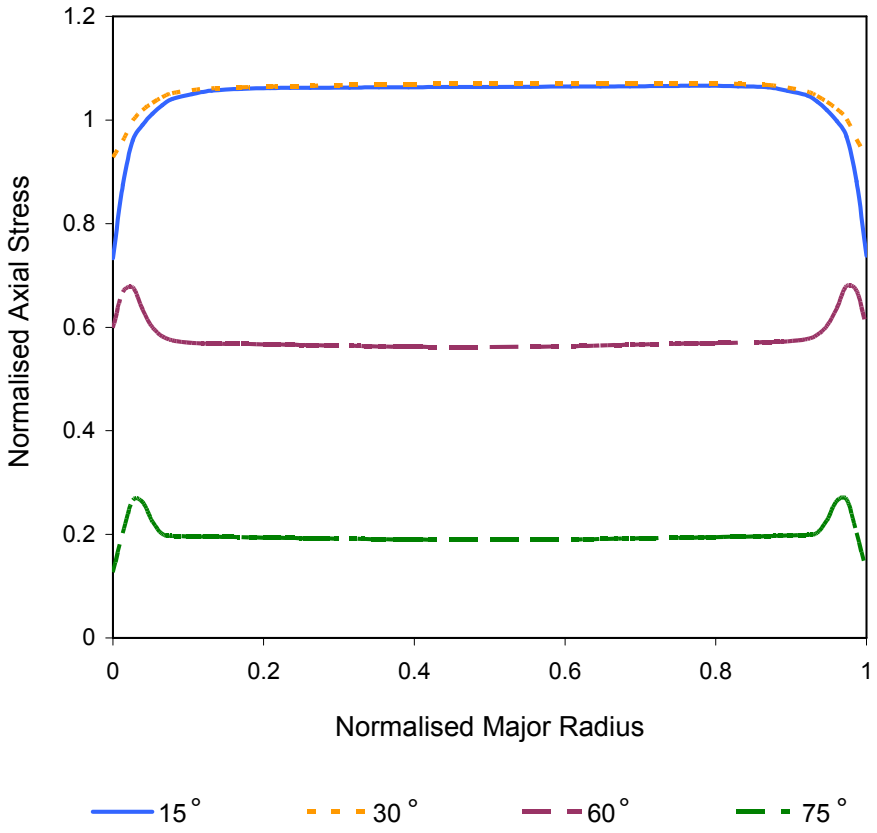

Figure 5-9: Stress gradient of the edge and central regions at the midlayer of the adhesive for different scarf angle

5.2 Axisymmetric Tensile Butt Joint Models

Due to the axisymmetric geometry of the tensile butt joint, three axisymmetrical slice models were built to calibrate the characteristic distances of the material models described in Chapter 6. The radius of all the models was kept at 6.00 mm, similar to the actual joints. The height of the aluminium alloy sections was 10.00 mm and the adhesive thickness was reduced to 0.2 mm to represent the adhesive thickness of the experimental joint.

The 2D mesh containing the relevant element sizes was first created from the *r-z* plane of the 3D butt joint model. The 2D mesh was then rotated through 1° angle about its vertical axis to form a unit thickness slice of solid elements in the angular direction. Other than the column of 15-noded wedge elements at the centre of the butt joint geometry, the rest of the elements were 20-noded quadratic hex elements.

The radial length of the elements in the central region of all three models was maintained within the range of 0.25 mm to 0.34 mm (similar to the 3D butt joint model) since the stress in the central region does not vary as much as at the edges. On the other hand, the lengths of the elements at the radial edge of all three models were refined for material calibration. The heights of the aluminium alloy elements within 1 mm distance from the adhesive layer (blue) were 0.1 mm. Beyond that, the heights of the aluminium alloy elements were 0.5 mm.

The main difference between all three models is the meshing of the adhesive section at the radial edge as shown in Figure 5-10. The mesh shown in Figure 5-10c had the smallest edge element of 6.6×10^{-3} mm and was used to calibrate the characteristic distance for the elastic-plastic von Mises material. The element length used for the initial calibration of the modified Drücker-Prager/Cap plasticity model was 0.04 mm (Figure 5-10b) and subsequently increased to 0.17 mm to verify the mesh sensitivity (Figure 5-10a).

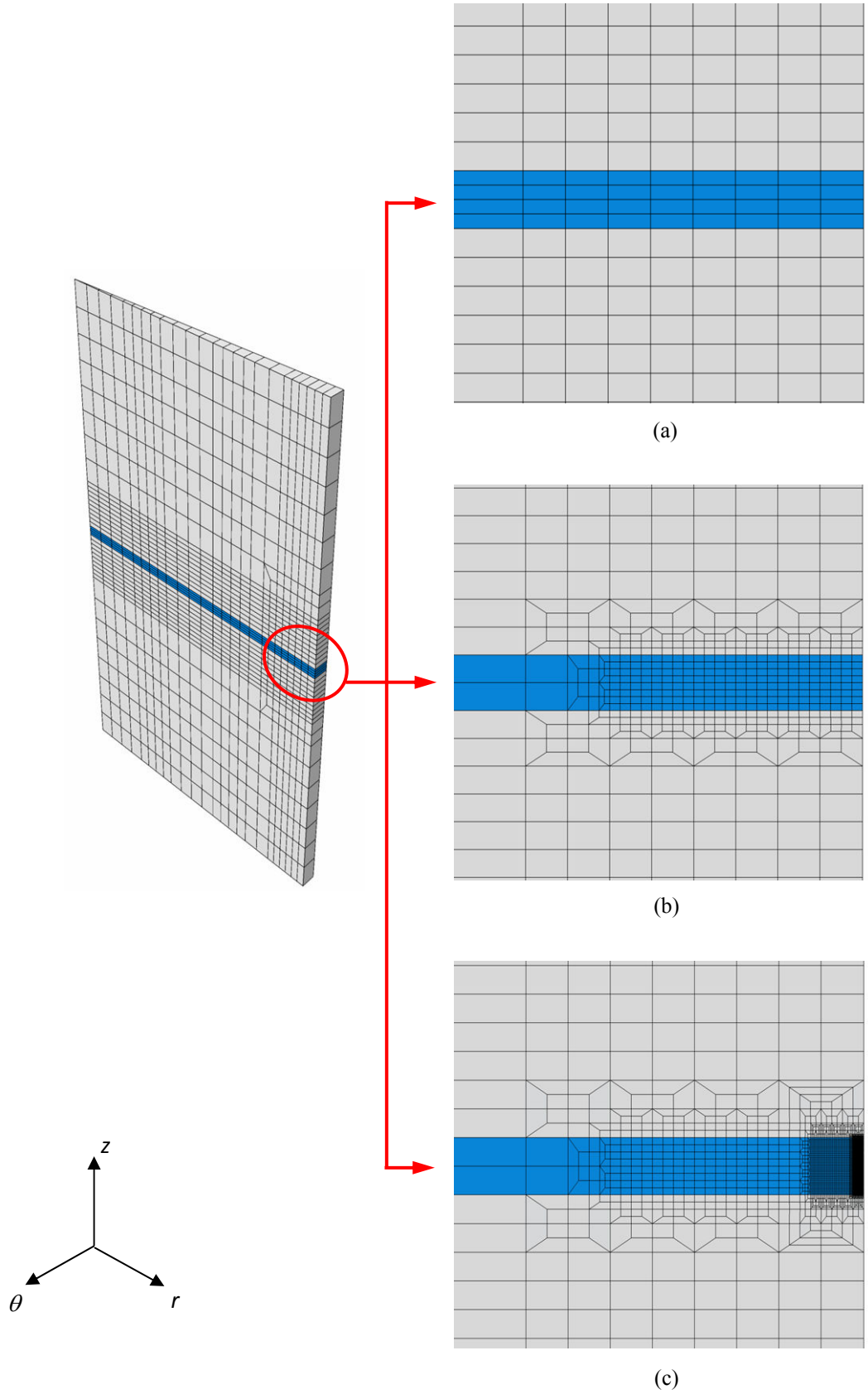

Figure 5-10: Typical axisymmetrical model for the tensile butt joint with three different meshing at the radial edge region of the adhesive layers.

The axisymmetric boundary conditions for all three slice models were the same. The displacements of all the nodes on the radial surfaces were constrained in the hoop direction and the column of nodes at the edge of the wedge elements were constrained in the radial direction to impose axisymmetrical boundary conditions on the models.

5.3 Uniform Panel Models

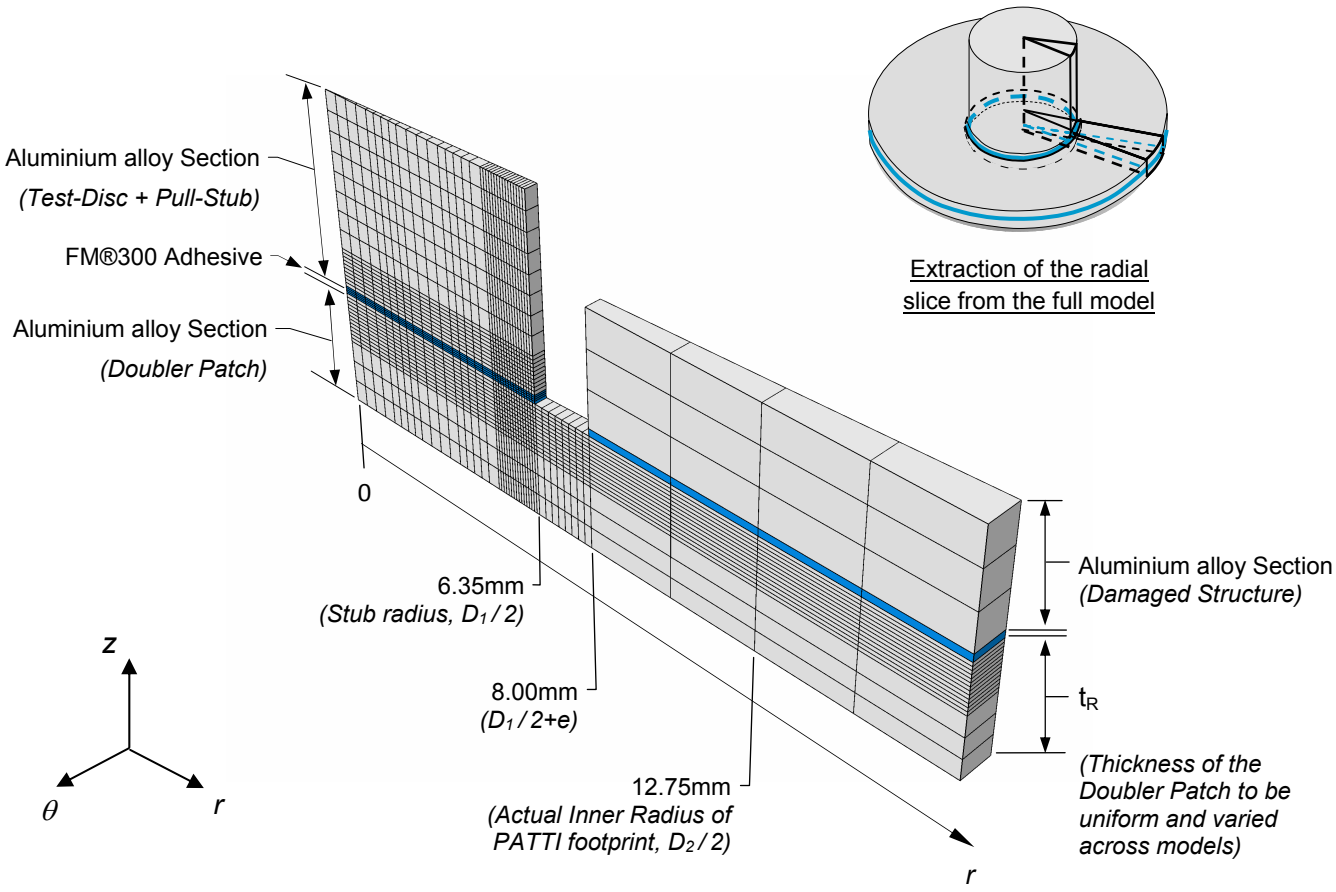

Figure 5-11: Typical radial slice model of the pull-test configuration with uniform underlying panel thickness

Four axisymmetric models of the pull-test configuration with uniform underlying panel thickness (t_R) of 0.7 mm, 1.3 mm, 1.7 mm and 3.0 mm were developed. For analyses of the uniform thickness panels, the typical radial slice model shown in Figure 5-11 was built

instead of the full three-dimensional models to save computational time. These models combined the pull-stub and test-disc to be the same aluminium alloy section and assumed that the bond between the stub and the structure to be infinitely strong. Similar to the axisymmetric tensile butt joint model, the entire radial slice model consisted of 20-noded quadrilateral elements except for the centremost column of elements that were formed by 15-noded wedge elements.

The stress distribution at the edge region of the adhesive are expected to exhibit large fluctuations, similar to the cylindrical butt joints loaded in tension. As such, a fine mesh was required at the edge region to capture the stress gradient near the edge. The same adhesive meshes used to determine the characteristic lengths for the von Mises and modified Drücker-Prager/Cap Plasticity materials were used to model the adhesive of the panel models.

Due to the very short characteristic distance calibrated for the von Mises material, the aluminium alloy elements adjacent to the edge of the adhesive in the uniform panel models were also refined to allow the transition from the coarse mesh at the far field to the fine mesh at the edge of the adhesive. The mesh at the edge of the adhesive is the same as that shown in

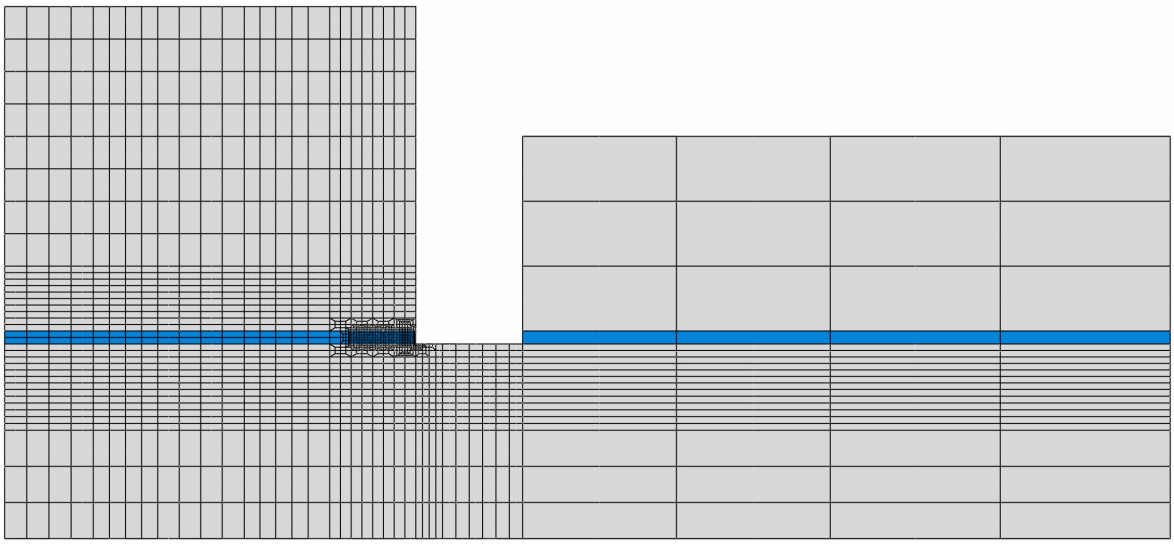

Figure 5-12: Typical uniform model with refined mesh at the edge of the adhesive for analyses with the von Mises material

Figure 5-10c. The typical uniform panel model for the von Mises material is shown in Figure 5-12 and the shortest element at the edge of the adhesive edge was 6.6×10^{-3} mm.

It was found that for the modified Drücker-Prager/Cap Plasticity material, the element length at the edge of the adhesive could be doubled without affecting the predicted strength. As such, the radial length of the elements at the edge region was increased to 0.085 mm. The elements in the central region for both types of material models were kept within the range of 0.25 mm to 0.34 mm, similar to the butt joint models.

The FM300 adhesive section was 0.2 mm thick in accordance to nominal adhesive thickness given in the datasheet [56] and close to the average adhesive thickness of 0.19 mm measured from the bonded panels. The FM300 adhesive section was modelled with four layers of elements for the modified Drücker-Prager/cap plasticity material and two layers when the adhesive was modeled with cohesive elements. This change was made because modeling four layers of cohesive elements for the adhesive led to convergence problems during the analyses. Two layers of cohesive elements were used to investigate if the models are able to capture the damage through the adhesive thickness similar to the strain distribution when using the modified Drücker-Prager/cap plasticity material for strength prediction in Section 7.3.3. The outcome of modeling with two layers of cohesive elements is shown in Section 8.2.1.

The elements beyond the 8 mm radial distance were relatively coarse since they were only used to simulate the restraint of the PATTI piston on the bonded structure during the pull-off test. The thickness of the upper aluminium alloy adherend was kept at 3 mm for all the models. The radial lengths of the elements were between 2.3 mm to 2.6 mm.

Using Figure 5-11 as reference to describe the boundary conditions for all the uniform panel models, the radial displacements of the column of nodes in the centre and the hoop displacements along the two radial faces were constrained to simulate axisymmetric

conditions. The top surface of the upper adherend, at 12.75 mm from the centre, was constrained in the z-direction, corresponding to the contact between the PATTI piston and the bonded structure as shown in Figure 3-5. Stress loads were applied on the top surface of the pull-stub upper surface of the "*Test-Disc + Pull-Stub"* aluminium alloy section.

In order to replicate the secondary bond between the pull-stub and the test-disc, the aluminium alloy section representing the "*Test-Disc + Pull-Stub*" was modified to include an additional layer of Hysol adhesive as shown in Figure 5-13. This allowed the effects of the secondary bond on the measured pull-strength and stress distribution within the structural adhesive to be studied. It was of interest to simulate the Hysol 9309.3NA adhesive used to bond the pull-stub to the structure because the key to measuring the strength of a bonded

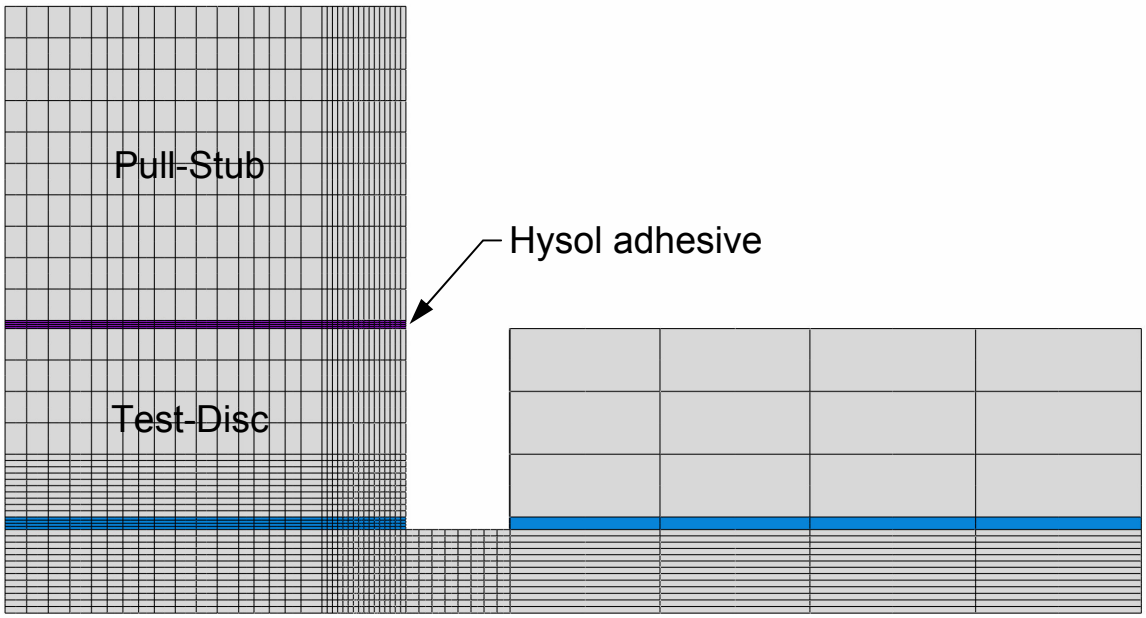

Figure 5-13: Typical uniform panel model with a layer of Hysol adhesive between the "Test-Disc" and "Pull-Stub" section

structure via the pull-test method requires failure to occur within the structural adhesive used for repair and not the secondary adhesive used to setup the pull-test configuration.

The radial length of the Hysol elements in the edge region was 0.085 mm; similar to that of the FM300 adhesive. The thickness of the Hysol section was 0.13 mm in accordance with the nominal thickness given in its datasheet [70] and formed of four layers of elements.

Lastly a 0.2 mm overcut was introduced into the 0.7 mm and 3 mm panel models as shown in Figure 5-14 to investigate if overcutting into the underlying panel has an effect on the predicted strength.

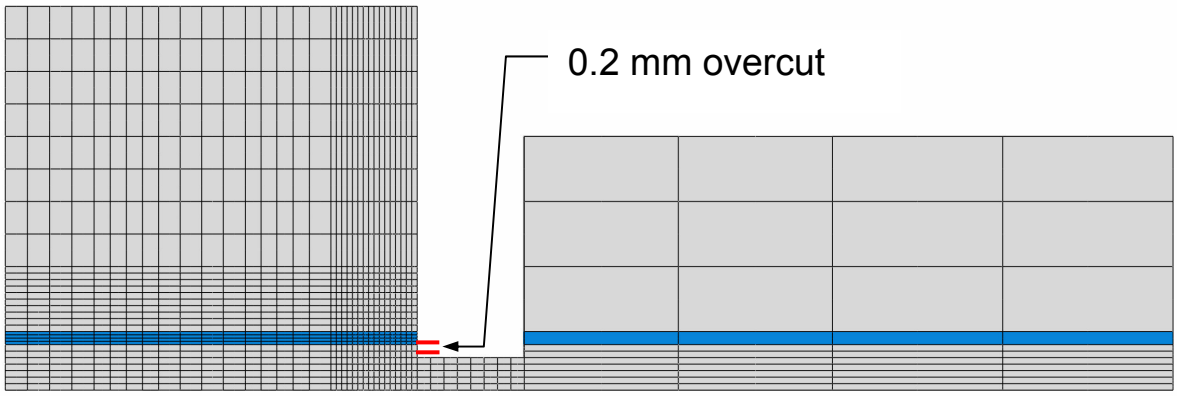

Figure 5-14: Typical uniform panel model with a 0.2 mm overcut

5.4 Tapered Edge Panel Models

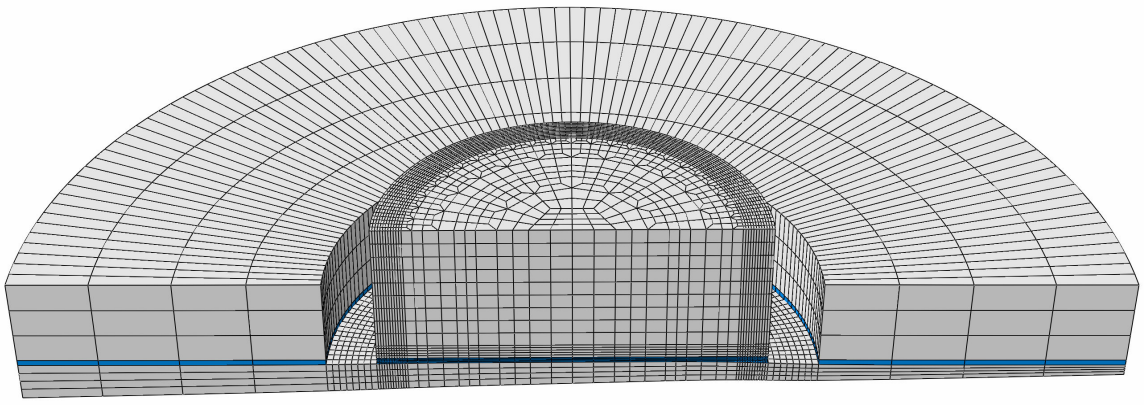

Figure 5-15: Typical three-dimensional model of the halved PATTI test configuration with finer mesh at the edge of the stub's adhesive and variation in underlying substrate thickness.

For analyses of tapered adherends, full 3D models as shown in Figure 5-15 were constructed to investigate the influence of thickness tapering on the pull-off strength. The tapered adherends in the models corresponded to the actual variation of substrate thickness in the experiments. The models were constructed of 8-noded linear hex elements to shorten computational time. It should be noted that the tapered edge panel cannot be simplified to a plain strain strip model formed from the "*cut-off*"' face of the 3D model shown in Figure 5-15. This is because such a model would only capture the loading as a beam bending case instead of the actual plate bending case.

Similarly constraints were applied to the topmost nodes of the aluminium alloy section representing the *'Damaged Structure'* in the three-dimensional tapered models shown in Figure 5-11. Surface loads were applied onto the upper surface of the *'Pull-Stub + Test Disc'* section.

6 Constitutive Materials for the Adhesive

Two plastic yield criteria, von Mises criterion and the linear Drücker-Prager criterion are employed to describe the constitutive behaviour of the FM300 adhesive. The calibrations for these two yielding criteria are described in this chapter.

6.1 Von Mises Material

The FM300 film adhesive was first idealised to obey the von Mises yield criterion. The pertinent material properties were obtained from the shear strength given in the Cytec datasheet [56] as shown in Figure 6-1. The ultimate shear failure strength of the adhesive was

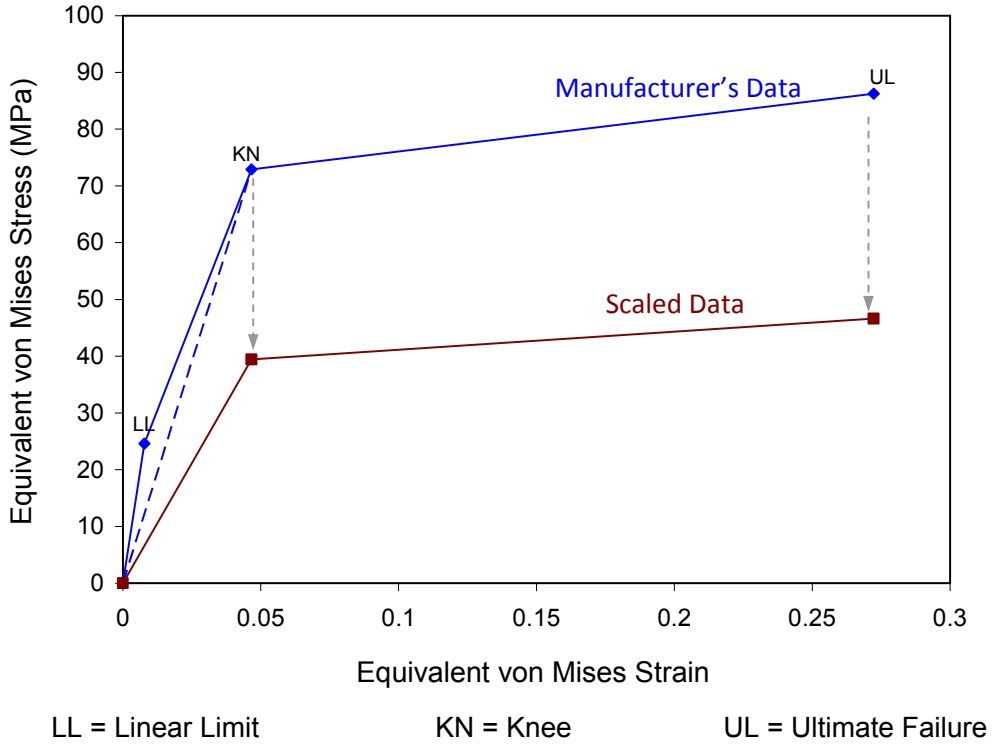

Figure 6-1: Equivalent von Mises data converted from the Cytec datasheet [56] and the scaled values to match the experiments.

reported to be 49.8 MPa by the manufacturer and is higher than measurements from the single lap-shear experiments.

The '*knee*' stress and strain values in the datasheet were used to denote the threshold of the elastic region in the work presented here because it marks the point when the plastic yielding of the adhesive occurs [22]. The stress-strain response of the adhesive is approximated as linear hardening (blue dash-lines).

The elastic and plastic properties of the FM300 adhesive were required to describe the von Mises model in ABAQUS [71]. By regarding the FM300 adhesive as an isotropic material that obeys the von Mises yield criterion, the shear strength given in the manufacturer's datasheet were converted to the equivalent von Mises stress, σ_{vm} according to Equation 6-1. After conversion, all the σ_{vm} values were scaled down by 44% as shown in Figure 6-1 so that the ultimate failure stress (UL point) matched the equivalent von Mises stress of the experimental lap-shear joints with surface preparation Method B given in Table 4-1. This knock-down factor is to account for the different curing methods (vacuum bag versus autoclave).

$$\sigma_{vm} = \sqrt{3}\tau \qquad \text{Eqn. 6-1}$$

The shear strains, γ in the datasheet were first converted into the absolute plastic strain values, $\gamma^{pl.}$ required for the tabular *"Plastic"* material function in ABAQUS through Equation 6-2 that removes the elastic portion of the strain. The equivalent strain values were not scaled and were kept as they are. The shear modulus, *G* was calculated from the '*knee*' stress and strain values of the scaled curve presented in Figure 6-1 since they denote the limit of the elastic region. The value of the Young's modulus at 666 MPa was lower than the value obtained from the conversion of the manufacturer's shear modulus due to the scaling of the stresses with the strains remaining unchanged.

$$\gamma^{pl.} = \gamma - \frac{\tau}{G} \qquad \text{Eqn. 6-2}$$

The $\gamma^{pl.}$ were subsequently converted into the neat equivalent von Mises strain, $\varepsilon_{vm}^{pl.}$ according to Equation 6-3.

$$\varepsilon_{vm}^{pl.} = \frac{\gamma^{pl.}}{2} \qquad \text{Eqn. 6-3}$$

Table 6-1: Parameters for the von Mises material model in ABAQUS

Elastic	
Young's Modulus (MPa)	Poisson's Ratio
666	0.3634
Plastic	
Yield Stress (MPa)	Plastic Strain
39.43	0
46.64	0.2172

The adhesive in the FE models were idealised to behave as an elastic-perfectly plastic von Mises material through the parameters given in Table 6-1. The same Poisson's ratio used for the elastic analysis in Section 5.1.3 was specified for the von Mises material.

6.2 Linear Drücker-Prager Yield Criterion

Previous work [13] had shown that the modified Drücker-Prager/Cap Plasticity material [27] was able to provide a good description of the yielding of a similar structural adhesive when subjected to triaxial stresses. As such, it was necessary to verify if the FM300 can be adequately described by the linear Drücker-Prager yield criterion.

The linear Drücker-Prager yield criterion relates the tensile stress to the shear stress affecting the yielding behaviour of the adhesive according to the relationship previously given in Equation 5-1. The normalised hydrostatic component in Figure 5-8 represents the tensile stress component and the normalised von Mises component represents the shear stress component affecting the failure of the joints. Aluminium alloy scarf joints of 0°, 15°, 30°, 60°, 75° and single-lap shear joints were employed to generate data corresponding to different stress ratios. The experiments and results of these joints are respectively described in Section 3.1 and Section 4.1.

Since the pressure sensitivity of the adhesive is due to crazing of polymers induced by positive hydrostatic stress [25, 26], the plastic deformation of the adhesive could be considered insensitive to compressive hydrostatic stress. As such, the yielding behaviour of the adhesive is restricted to the hydrostatic tensile region with insensitive compression yielding.

The following sub-sections describe the validation of the yield criterion for the FM300 adhesive and the effects of surface preparation and environmental conditioning on its yielding behaviour.

6.2.1 Pristine (Dry) Condition Joints

Multiplying the effective fracture strengths (after applying the void correction method described in Section 3.1.1) of the scarf and lap-shear joints, shown in Figure 4-3, by the normalised stress components in Figure 5-8, a plot of the von Mises stress versus the hydrostatic stress can be generated as shown in Figure 6-2. The R-squared values of linear regression curves fitted through the data points were from 0.9631 to 0.9813. The linear trend lines fitted the plots of the effective fracture strength better than those generated from the measured (raw) fracture strength that only gave R-squared values from 0.8162 to 0.9813.

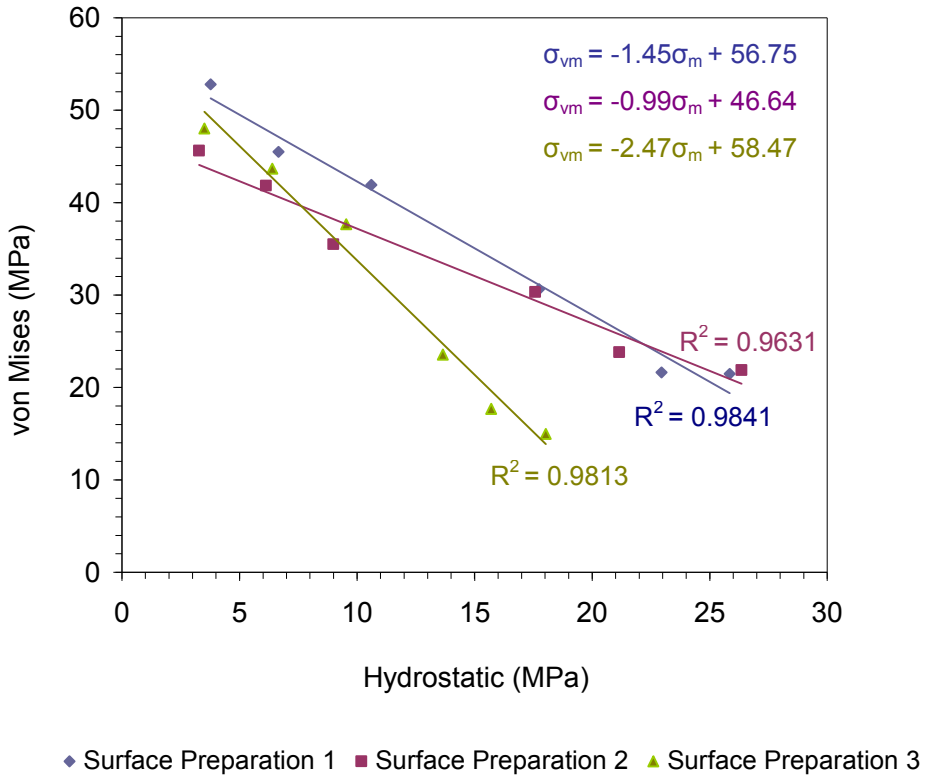

Figure 6-2: 'Corrected' linear Drücker-Prager fit for dry joints.

The slope of the plot, *m*, for surface preparation Method C (without silane) is almost twice that of Method A and Method B (with silane). On the other hand, joints prepared using surface preparation Method C showed partial interfacial failure. In this case the data from joints using Method C do not reflect the true adhesive properties.

The ultimate shear strength, τ_0 of joints prepared to a specific surface preparation method can be calculated from the σ_{vm}-intercept ($=\sqrt{3}\tau_0$) in the absence of any hydrostatic (peeling) stresses. This provides a method to determine the ultimate shear strength of the adhesive without the influence of the peeling stresses induced by the bending moment of a single lap-shear joint. Despite the gradient of the non-silaned joints being greater than the silaned joints, the σ_{vm} -intercept only differed by 12%. This shows that the dry shear strength of the FM300 joints is not sensitive to the surface preparation techniques used in this experiment. However, the dry flatwise tensile strength of the joints is sensitive to the presence of silane because as the proportion of hydrostatic stress component increases (and scarf angle decreases), so does the difference between the fracture strengths of the silaned and non-silaned joints. The results for the tensile butt joint are represented by the data points at the bottom-right-hand ends of each linear curve.

6.2.2 Hot and Wet Conditioned Joints

Similar to the dry joints, the fracture strengths of the conditioned (85% RH, 70°C) joints were multiplied to the normalised stress components to produce the plots in Figure 6-3. The linear regression curve fitted the plot of the conditioned joints with silane (surface preparation Method A) gave an R-squared value of 0.9930.

In contrast, the R-squared value for a linear curve through the conditioned joints without silane (surface preparation Method C) is only 0.5591. The poor fit of the curve is due to the 30° scarf joints being almost as strong as the unconditioned joints. It is not known what might have caused this abrupt increase in strength seeing as the 30° joints showed the same mixed cohesive-interfacial mode failure as the rest of the conditioned joints without silane and were conditioned for the same duration and under the same condition.

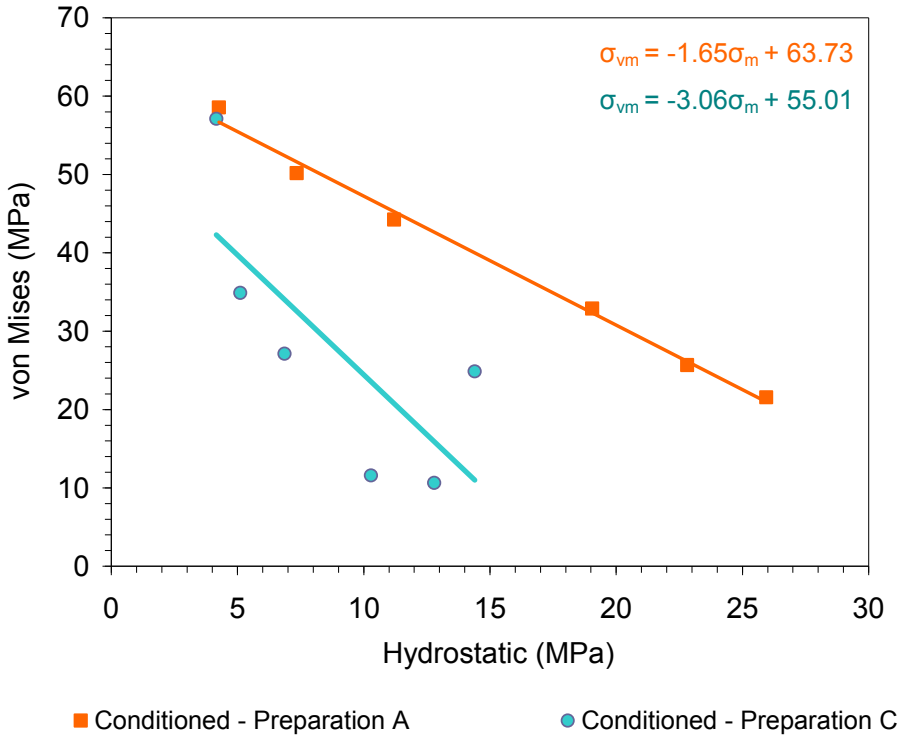

Figure 6-3: Linear Drücker-Prager fit for conditioned joints.

The strength of the conditioned lap-shear joints without silane is similar to those with silane. The conditioned lap-shear joints without silane show a 150% increase in strength from the 75° joints instead of the expected 82% increase (see Figure 4-6). By removing the outliers corresponding to the 30° scarf joint and the lap-shear joint, the R-squared fit would have improved to 0.9272. Nonetheless, this shows that the shear strength of the lap-shear joints is hardly affected by the high humidity and temperature conditioning.

6.2.3 Influence of Surface Preparation and Environmental Conditioning on Joint Strength

A comparison between the linear Drücker-Prager plots for all the conditioned and dry joints in Figure 6-4 showed that there is no significant change for joints made using Method A. In fact, the conditioned joints showed a 5% improvement in strength for the shallow scarf joints and gradually improved to 13% for the lap-shear joints. It is suspected that the presence of moisture within the adhesive layer caused plasticization and raised the fracture toughness

of the adhesive, which in turn caused the adhesive to fail at a higher load. A similar phenomenon was observed by LaPlante *et. al*. [34] who found that bulk FM300 specimens conditioned in a hot and wet environment failed at a higher load and strain compared to unconditioned specimens. Nonetheless, the joints prepared according to Method A exhibited cohesion failure regardless of their environmental conditioning and showed strength durability.

Apart from the lap-shear joints, the conditioned scarf joints prepared according to Method C showed strength reduction from their unconditioned counterparts. This reduction is caused by the higher percentage area of interfacial failure observed on all the joints.

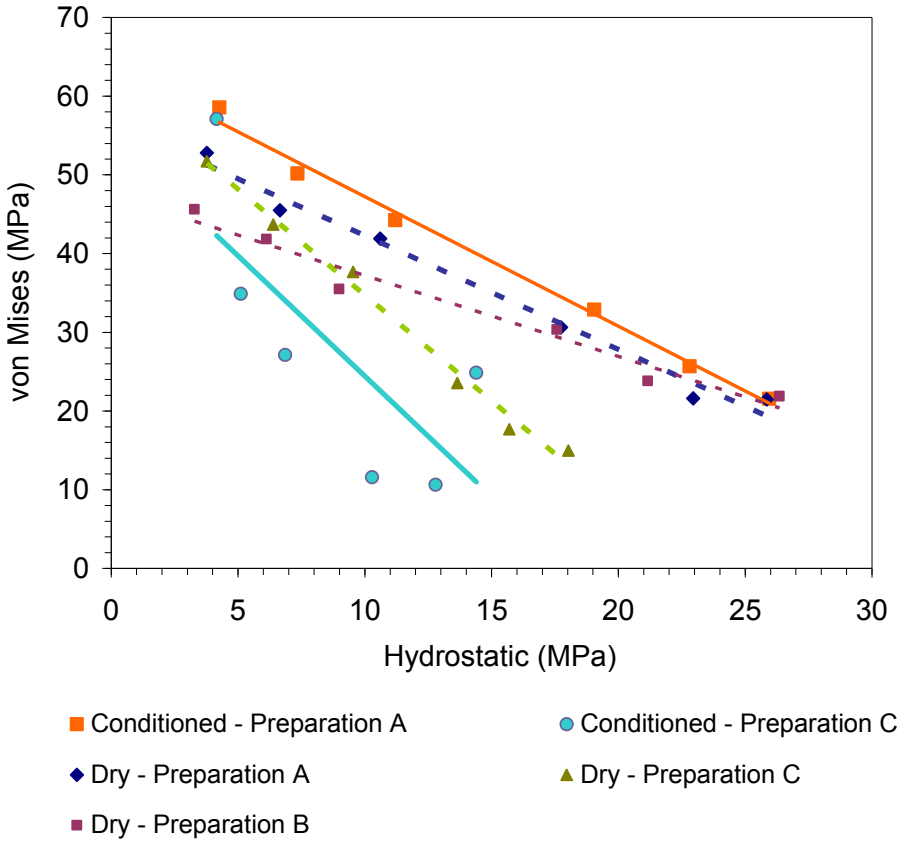

Figure 6-4: Linear Drücker-Prager plots of all the scarf and lap-shear joints

From the plots of all the joints in Figure 6-4, the hydrostatic pressure component of the bond is more affected by the surface preparation technique and the environmental conditioning compared to the von Mises stress component which represents the shear stress

component influencing the failure. Since the hydrostatic pressure component dominates the loading configuration of the PATTI pull-tests, the tensile pull-off strength of the tests will show variation for bonds affected by the inadequate surface treatment and environmental degradation because the hydrostatic pressure represents the tensile stress component affecting the yielding of the joints.

However a reduced tensile pull-strength does not necessarily mean a reduction in the shear strength of the bond because all the steeper angle scarf joints undergoing large amounts of deviatoric stress showed relatively consistent values for the equivalent von Mises stress component. The fact that the fracture strength of these joints hardly changes indicate that shear strength is retained when the failure of the joint is dominated by the deviatoric stress component.

6.2.4 Modified Drücker-Prager / Cap Plasticity Material

The modified Drücker-Prager/Cap Plasticity material in ABAQUS was selected to apply the linear Drücker-Prager criterion to the FM300 adhesive layer of the panel models. In total the Drücker-Prager/Cap plasticity model requires six parameters to describe the tensile and compressive yielding of the material.

Similar to Equation 2-1, the linear Drücker-Prager yield surface in ABAQUS describes the plastic yielding behaviour under tensile load according to

$$F_s = t - p\tan\beta - d = 0 \qquad \text{Eqn. 6-4}$$

where t and p denote a deviatoric stress and the hydrostatic pressure stress (= $-\sigma_m$) respectively. The parameter β is the angle of friction of the material ($\tan\beta = m$) and d is the material von Mises yield strength (=$\sqrt{3}\tau_0$). The deviatoric stress t is defined by

$$t = \frac{1}{2}\sigma_{vm}\left[1 + \frac{1}{K} - \left(1 - \frac{1}{K}\right)\left(\frac{r}{\sigma_{vm}}\right)^3\right] \qquad \text{Eqn. 6-5}$$

where σ_{vm} is the von Mises stress and r is the third stress invariant. By setting the parameter K to 1.0, the deviatoric stress recovers the von Mises stress and Equation 6-4 describes the linear relationship between the von Mises stress and the hydrostatic pressure. The parameters β and d were previously determined from the dry scarf joint experiments with surface preparation Method B which was used to prepare the bonding surface of the PATTI test panels.

The linear Drücker-Prager yield surface is valid until it meets the cap yield surface described by Equation 6-6.

$$F_c = \sqrt{\left[p - p_a\right]^2 + \left[\frac{R\sigma_{vm}}{\left(1 + \alpha - \alpha/\cos\beta\right)}\right]^2} - R\left(d + p_a \tan\beta\right) = 0 \qquad \text{Eqn. 6-6}$$

where p_a denotes the initial yield surface position, α the transition surface radius, and R the cap eccentricity. The cap yield surface limits the deviatoric yield surface in the hydrostatic compression region by providing an inelastic hardening mechanism to simulate plastic compaction. Since the formulation of the Drücker-Prager yield surface within the model allows the material to dilate, the cap yield surface also softens the material when it is yielding in shear and captures the characteristic of the FM300 adhesive that does not undergo substantial volume expansion upon yielding. The parameter R controls the eccentricity of the cap yield surface, reflecting the sensitivity of compressive yielding to the hydrostatic stress.

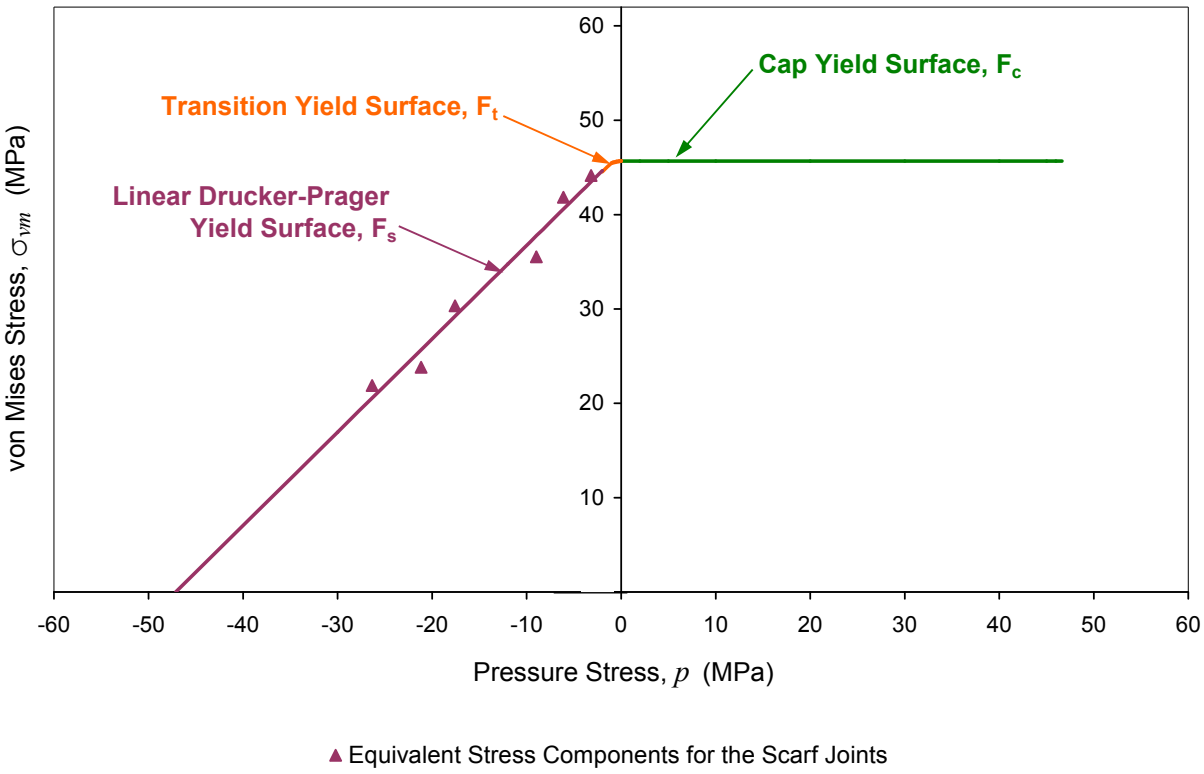

Figure 6-5: Yield surfaces of the FM®300 adhesive specified by ABAQUS 6.10 Modified Drücker-Prager/Cap model in the deviatoric-hydrostatic plane.

Upon specifying the shear and cap yield surfaces, the magnitude of α controls the transition between the two yield surfaces via the following relation,

$$F_t = \sqrt{\left[p - p_a\right]^2 + \left[\sigma_{vm} - \left(1 - \frac{\alpha}{\cos\beta}\right)\left(d + p_a \tan\beta\right)\right]^2} - \alpha\left(d + p_a \tan\beta\right) = 0 \qquad \text{Eqn. 6-7}$$

This transition surface serves to link the linear Drücker-Prager and Cap yield surfaces.

Since the plastic deformation of film adhesives could be considered insensitive to compressive hydrostatic stress within the context of the pull-test's loading conditions, the pressure p_a is assigned to be zero. The linear Drücker-Prager yield surface is therefore effectively restricted to the hydrostatic tensile region and the cap yield surface is specified to begin when the hydrostatic stress component is zero. The parameter R can be set to the maximum allowable input value of 1000 [27] to describe a compression-insensitive yielding,

i.e., the yield surface is a horizontal line in the positive pressure regime. The yield surfaces defined by the modified Drücker-Prager/Cap Plasticity material model are shown in Figure 6-5, whereby the negative hydrostatic pressure represents yielding under tension and positive hydrostatic pressure represents yielding under compression. The yield surfaces, consisting of the linear Drücker-Prager surface F_s, the transition yield surface F_t, and the cap yield surface F_c, shown in Figure 6-5, are fully defined by the parameters given in Table 6-2.

Table 6-2: Modified Drücker-Prager/Cap plasticity parameters for the FM®300 adhesive layer.

d (MPa)	β (°)	R	p_a (MPa)	α	K
46.64	44.71	1000	0	0.05	1.0

Another set of the modified Drücker-Prager/Cap plasticity parameters given in Table 6-3 were specified for the Hysol EA 9309.3NA epoxy paste adhesive. New values were generated for the parameters d and β since the tensile yielding behaviour of the pull-tests is governed by the linear Drücker-Prager surface F_s. These values were obtained from the lap-shear test in the manufacturer's datasheet [70] and through additional experiments where the 0° and 30° scarf joints bonded with the EA 9309 paste adhesive were loaded to failure in tension. The method to generating the linear Drücker-Prager yield surface is similar to the technique described in Section 6.2.

Table 6-3: Modified Drücker-Prager/Cap plasticity parameters for the Hysol EA 9309.3NA adhesive layer.

d (MPa)	β (°)	R	p_a (MPa)	α	K
84.54	79	1000	0	0.005	1.0

6.3 Summary of Material Models

Two sets of parameters were generated to describe the constitutive properties of the FM300 adhesive for FE analyses. The yielding behaviour of the FM300 adhesive was first described to obey the von Mises yield criterion through the parameters given in Table 6-1. These parameters were generated by adapting the stress-strain curve given in the manufacturer's datasheet to the experimental measurements of the single lap-shear joints.

The material parameters given in Table 6-2 and Table 6-3 respectively described the yielding behaviour of the FM300 and Hysol 9309.3NA adhesives according to the linear Drücker-Prager yield criterion via the modified Drücker-Prager/cap plasticity material model in ABAQUS. The parameters for the adhesives were generated from a combination of the scarf joint experiments to determine their fracture strengths and the linear elastic FE analyses to determine the tensile and deviatoric stress components affecting their failure.

These material parameters were assigned to the adhesive sections of the FE models in the Chapter 7 to predict the pull-off strength of the panels on tapered edges and on different thicknesses.

7 Bond Strength Prediction

A failure criterion is required to determine when to assume failure for the FE joint. Due to plastic yielding, a strain-based failure criterion was selected to predict the strength of the joints in the present investigation. The suitability of two yield criteria was evaluated: von Mises yield criterion and the linear Drücker-Prager yield criterion.

The strain-based failure criterion assumes that joints attain their ultimate strength when the maximum strain at a characteristic distance from a corner singularity reaches the adhesive failure strain. While the critical failure strain of the adhesive is an inherent property that remains unchanged regardless of the failure criterion, the characteristic distance is dependent on the assumed failure criterion.

One major complication in predicting the failure strength of bonded joints is that deformation tends to concentrate at the corners, due to the corner singularity effect [72]. This singularity effect is caused by the large difference between the moduli of elasticity for the metallic adherend and the adhesive. When a butt joint is loaded in tension, the deformation in the adherends is negligible in comparison with the adhesive. However, Poisson's ratio effect and the relatively lower modulus of elasticity of the adhesive cause the edge of the adhesive in a butt joint to contract much more than the metallic adherend. This difference in deformation gives rise to a corner singularity. The works of Karachalios et. al. [73] state that the high values exceeding the adhesive allowable at the corner singularity does not necessarily signify joint failure and the load on the joint could still be transferred via other parts of the adhesive in the through-thickness direction. Their FE analyses showed that the strain distribution away from the corner is not greatly influenced by the corner singularity and that only when these strains exceed the adhesive allowable do the joint starts to fail.

As a result of the corner singularity, refining the mesh at the region will see the stress and strain in the corner region to increase indefinitely. The values of stress or strain near the corner node cannot be used to predict the strength of the joints because its values depend strongly on the size of the elements. To overcome this non-uniform strain distribution problem in joints, it is necessary to introduce a characteristic distance: joints are said to have reached its maximum load-carrying capacity when the maximum principal strain at the characteristic distance reaches the critical value, ε_c. Through this approach, it is assumed that joint failure will occur when the region within the characteristic distance exceed the critical strain even if the central region of the adhesive has not yielded.

This appropriate distance needs to be determined by comparing FE model analysis and experimental results: the characteristic distance is the distance between the most highly stressed corner and the point where the principal strain attains the material's failure strain when the model is subjected to the experimentally measured failure load. Because the strain distribution is strongly dependent on the yield criterion, the characteristic distance needs to be calibrated each time a new material constitutive model is used to describe the adhesive.

7.1 Failure Criterion

To predict the failure strength of the bonded discs measured by the PATTI test, a failure criterion is required in the finite element modelling. A failure criterion [25] expressed in terms of the maximum principal strain, $\varepsilon_{\max}$ and the hydrostatic stress, σ_m was previous given in Equation 2-6.

$$\varepsilon_{\max} + \frac{\sigma_m \tan\beta}{E} = \varepsilon_c \qquad \textit{Eqn. 2-6}$$

where ε_c is the critical strain value when the hydrostatic stress, σ_m is zero. The parameter $\tan\beta$ (=0.99) reflects the sensitivity of the material to hydrostatic tensile stress and the

method undertaken to obtain its value was presented in Section 6.2.1. The Young's modulus is denoted by E. When applied to the FE models, this criterion assumes failure to occur when the combination of strains within any adhesive element; calculated by the left-hand term, achieves the pre-determined ε_c. This means that the critical failure strain value needs to be decided before this criterion can be used.

According to the manufacturer's datasheet, the FM300 film adhesive with 0.2 mm thickness within a thick adherend lap shear joint was measured to give an engineering shear failure strain of 0.545 [56] at room temperature. The shear strain of the adhesive within the tapered panel were assumed to be the same as the value reported in the datasheet because the average adhesive thickness within the panels was measured to be 0.191 mm which is close to the nominal thickness reported in the datasheet.

A simple linear elastic FE analysis of the thick adherend lap joint was performed to determine the behaviour of the principal strains within the adhesive. An element taken from the middle of the adhesive was shown to have negligible strain in the lateral (width) direction and the other principal strains were equal and of opposite signs to each other. This shows that plane strain conditions given in Equation 7-2 could be assumed for the adhesive within the thick adherend lap shear joint. As such, the engineering shear strain reported in the datasheet can be converted to the maximum principal strain via the Mohr's circle method according to Equation 7-3 and 7-4 to arrive at the normal critical failure strain.

$$\varepsilon_{mid} = 0 \quad , \quad \varepsilon_{\max} = -\varepsilon_{\min} \qquad \text{Eqn. 7-1}$$

$$\frac{\gamma_{\max}}{2} = \frac{\varepsilon_{\max} - \varepsilon_{\min}}{2} \qquad \text{Eqn. 7-2}$$

$$\varepsilon_c = \varepsilon_{\max} = \frac{\gamma_{\max}}{2} \qquad \text{Eqn. 7-3}$$

In the context of the FM300 adhesive, the hydrostatic strain failure criterion in Equation 2-6 then becomes Equation 7-4.

$$\varepsilon_{\max} + \frac{\sigma_m \tan\beta}{E} = 0.270 \qquad \text{Eqn. 7-4}$$

Instead of using separate failure criteria to predict the strength single lap-shear joints and scarf joints [49], the maximum principal strain failure criterion can be used to predict both types of joints by performing the same strain conversion as described in Equations 7-1 to 7-3.

Although the critical tensile failure strain used for strength predictions in the work here was set to be 0.270, it is worth noting that this value depends on the method undertaken to measure or derive it. While similar method of measurement is expected to produce similar strain values, comparison between Cytec's measurements with those measured by Lee *et. al.* [68] proves otherwise. To further complicate the matter, the tensile failure strain of the FM300 bulk adhesive is lower than the values measured via the thick adherend lap shear tests. Nonetheless, with proper calibration of the critical characteristic distance within the FE models, these other strain values could also be used to give equally good strength predictions.

Before deciding which of these failure criteria is most suitable in predicting the strength of the joints, a characteristic distance needs to be calibrated to avoid the corner singularity effect due to the difference in material stiffness of the adherend and the adhesive.

7.2 Prediction with the von Mises Yield Criterion

7.2.1 Calibration of Characteristic Length

The FE joint models are assumed to reach their maximum load-carrying capacity when the strain at the characteristic distance reaches the predetermined critical strain value,

ε_c. The type of strain at the characteristic distance is dependent on the failure criterion used. This distance is determined by the position of the element away from the most highly stressed corner to first attain the critical strain value when the model is subjected to the experimental fracture load. The adhesive layers of the axisymmetric tensile butt joint models from Section 5.2 were designated with the von Mises yield criterion described in Section 6.1 and used in conjunction with the maximum principal strain failure criterion to calibrate the characteristic distance.

The model with the coarsest mesh shown in Figure 5-10a was first used for the calibration of this characteristic distance. However, when the fracture load was applied onto the model, the highest maximum principal strain achieved by an element at 0.085 mm radial distance from the corner was 16% of the critical failure strain. Next, the fracture load was applied to the model shown in Figure 5-10b with twice the mesh density of the first. The highest strain had increased to 17.4% of the critical value and was achieved by an element at 0.042 mm radial distance from the corner.

Mesh refinement was done on the edge until an element in the mesh shown in Figure 5-10c achieved the critical strain corresponding to the experimental fracture load. The radial distance from the corner when the maximum principal strain in the adhesive attained the critical strain at the experimental fracture load is 1.65×10^{-3} mm. The behaviour of the critical element in each mesh is shown in Figure 7-1 for comparison.

The calibration for the characteristic distance described thus far was undertaken using the maximum principal strain failure criterion. When using the hydrostatic strain invariant failure criterion, the characteristic distance was calibrated to be 2.3×10^{-3} mm for the same mesh density, which is larger than for the maximum principal strain. The hydrostatic stress component of the critical element was used to calculate the hydrostatic term of the failure

criterion. With these characteristic distances, the pull-off strength of the panels could now be predicted.

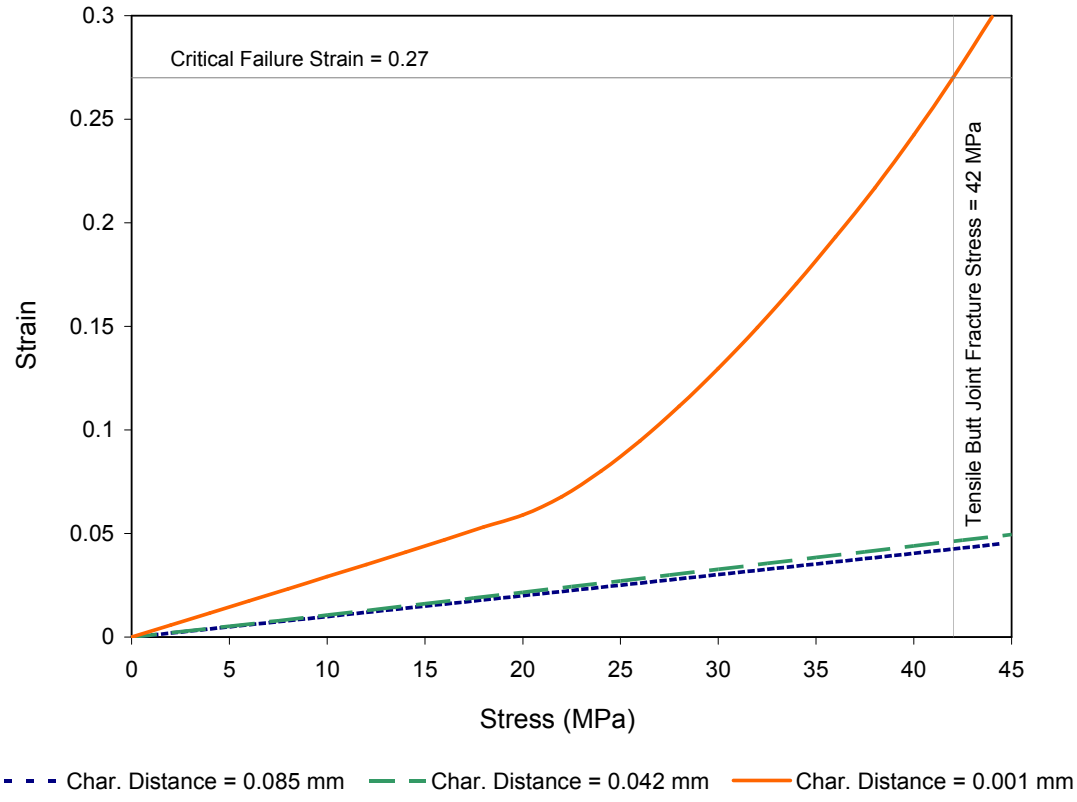

Figure 7-1: Comparison of the behaviour of the critical element in each mesh.

7.2.2 Panel Strength Prediction

The FE models with the typical refined meshing at the edge of the adhesive as shown in Figure 5-12 were used with the characteristic distance calibrated for the von Mises yield criterion to predict the pull-off strength of the panels.

Even though the hydrostatic term in Equation 7-4 was calculated to contribute 19% of the critical strain, the characteristic distance calibrated from the hydrostatic strain invariant failure criterion predicted similar pull-off strength to the maximum principal strain failure criterion. This shows that the maximum principal strain parameter on its own is sufficient to predict the strength of the uniform FE panels when their adhesive layers are described by the

von Mises criterion. As such, only one set of prediction was plotted in Figure 7-2 for comparison with the experimental pull of strength.

However, combining the FE models with the von Mises criterion severely underpredict the experimental pull-off strengths. This shows that the von Mises criterion is unable to capture the yielding behaviour of the FM300 adhesive under tensile dominated loading.

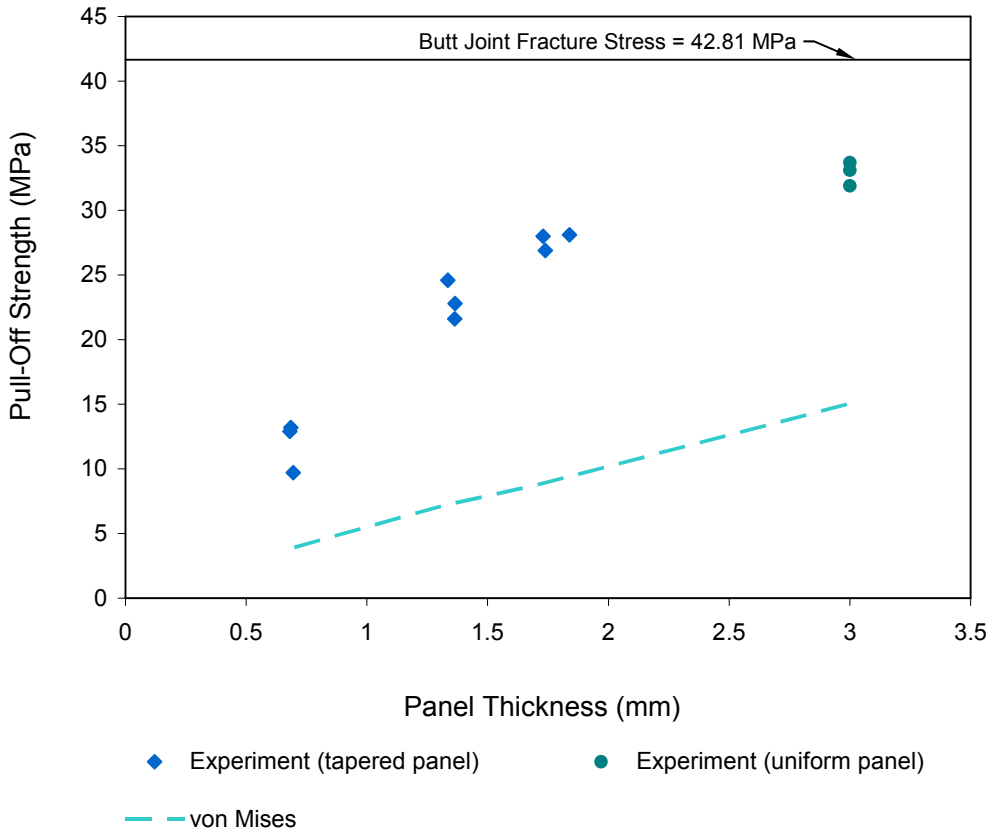

Figure 7-2: Plot of the experimental pull-off strength and the prediction by the uniform panel FE models with von Mises material versus the underlying panel thickness.

7.3 Prediction with the Cap Plasticity material

7.3.1 Calibration of Characteristic Length

Similar to the calibration method presented in Section 7.2.1, a characteristic distance first needs to be determined before any predictions can be made for the PATTI pull-off

strengths. The average failure load of butt joints was applied to the axisymmetric tensile joint model shown in Figure 5-10b. The adhesive layers of the model were specified with the modified Drücker-Prager/Cap Plasticity material described in Section 6.2. The characteristic distance when the maximum principal strain equals to the adhesive's failure strain was found to be 0.8 mm which is significantly larger than the characteristic distance found using the von Mises elastic-perfectly plastic material to define the adhesive layer. When using the hydrostatic invariant strain failure criterion, the characteristic distance was found to be 0.69 mm. The highest von Mises stress in the Aluminium alloy sections at the average failure load of the joint was 42 MPa which is well below the tensile yield strength of any Aluminium alloy.

Table 7-1: Comparison of failure strengths from FE prediction and experimental measurement for the tensile butt joint.

Joint Type	Failure Strength (MPa)		Difference (%)
	Experimental *(Standard Deviation)*	FE Prediction	
Tensile Butt Joint	42.81 *(2.69)*	41.66 (fine mesh)	-2.69
		39.64 (coarse mesh)	-7.40

To verify that the critical distance according to the modified Drücker-Prager/Cap Plasticity material is independent of the mesh density, the calibration technique above was repeated with a coarser mesh. The strength predicted by the coarse mesh model using the predetermined critical distance from the fine mesh model using the maximum principal strain failure criterion only deviated by 4.7% as shown in Table 7-1, indicating that the critical distance is not influenced by the meshing.

7.3.2 Scarf Joint Strength Prediction

The adhesive layers within the FE scarf joints presented in Section 5.1.1 were designated with the modified Drücker-Prager/Cap Plasticity material and the strength of the joints were predicted using the characteristic distance of 0.8 mm calibrated for the material model. These scarf joint models can be used to predict the strength of the joints because the radial lengths of the adhesive's edge elements had been shown to be less than the characteristic distance.

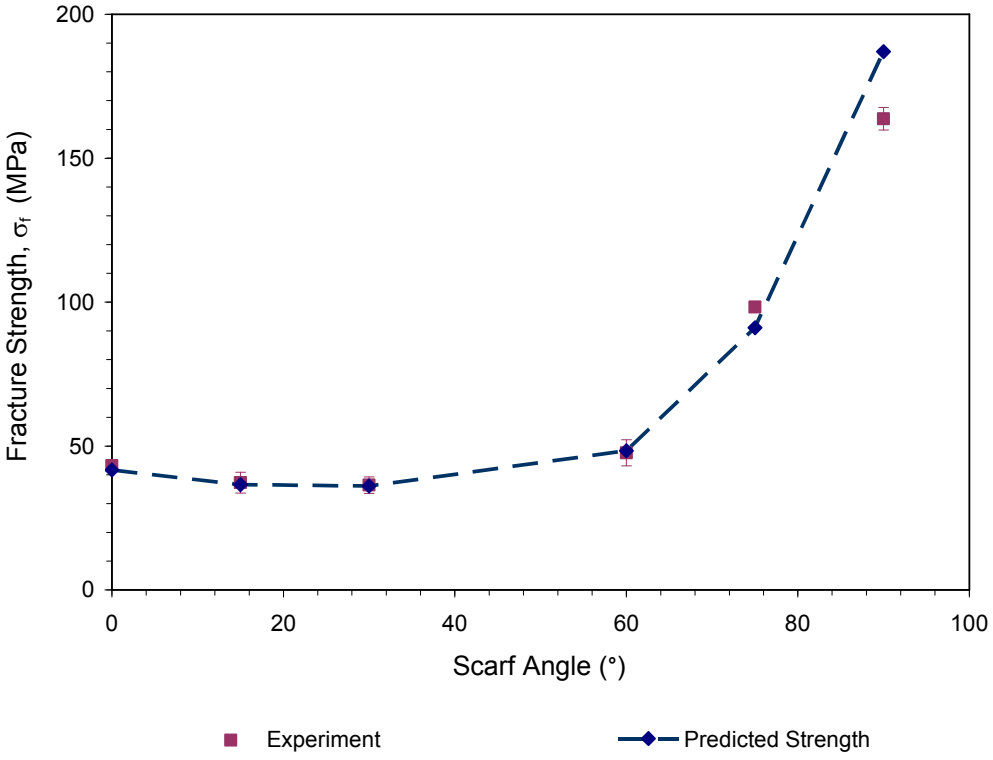

Figure 7-3: Predicted strength for the scarf and single lap-shear joints using the modified Drücker-Prager/Cap Plasticity material.

The predicted strength of the 0° to 60° scarf joints using the characteristic distance from the maximum principal strain failure criterion only differed from the experimental fracture strength by 3.5% as shown in Figure 7-3. The predicted strength for the 75° scarf joint

showed a larger divergence of 7.4% from the actual experimental strength and this divergence increased to 11.3% for the single lap-shear joints.

Since using the 0.8 mm characteristic distance under-predicts the strength of the 75° scarf joint, a larger characteristic distance of 1.6 mm was arbitrarily selected to investigate if the prediction could be improved. Nonetheless, the strength predicted with the larger distance only improved the difference from the actual strength to 7.2%. In fact, when the maximum principal strain across the adhesive layers exceeded the critical failure strain, the difference between the prediction and the actual strength was still 6.8%. This shows that the 0.8 mm characteristic distance can be used to predict the strength of the 75° scarf joint.

The joint strength predicted with the characteristic distance of the hydrostatic invariant strain only differed from predictions in Figure 7-3 by less than 1%. Once again, the maximum principal strain was sufficient as a parameter to predict the strength of joints modeled with the modified Drücker-Prager/Cap Plasticity material.

The lap-shear joints used in the experiments were considered to have short overlap length. Although the difference of their predicted strength was only 11.3%, yielding of the short lap-shear joints occurred across the entire bondline, making their configuration less ideal for the calibration of the characteristic distance. The same can also be said of the steep 75° scarf joint where the predicted strength does not appear to be as sensitive to the characteristic distance as the shallower scarf joints.

Nevertheless, the use of the characteristic distance of 0.8 mm with the current modified Drücker-Prager/Cap Plasticity material was shown to be suitable for use on scarf joint configurations undergoing as minimal as 20% hydrostatic stress (referring to scarf joints up to 60° joints in Figure 5-8) within the adhesive. Furthermore, the loading of the actual pull-off test is more alike the tensile butt joint setup where the hydrostatic component affecting the failure of the joint is highest compared to the rest of the scarf joints.

With the FE models predicting a similar trend for the fracture strength of the scarf joints, the decrease in fracture strength as the scarf angle increases from 0° to 30° was shown to be caused by the intrinsic yielding behaviour of the adhesive when subjected to small off-normal loads. The initial increase of the scarf angle from 0° to 15° resulted in 12% strength reduction from the strength of the tensile butt joint while subsequent increase to 30° only caused a further 1% reduction. It is important that this reduction in strength is not mistaken as degradation of the bond. The method to remove the off-normal loading effect on the measured strength of the pull-test is presented in the following sub-section 7.3.2.1.

7.3.2.1 Effects of Off-Normal Loading on Pull-Strength

In practice, it is unlikely that the pull-test stubs would ever be loaded at off-angles beyond 6°. This phenomenon is verified by shimming packers between the PATTI piston and the bonded structure (unpublished experiment by DSTO). In addition to tilting the piston at an angle to the bonded structure, a gap was introduced between the piston and the reaction plate. The size of this gap was found to increase with the thickness of the packer used. The gasket within the housing was squeezed through the gap during pressurization when the size of the gap was sufficiently large. When this occurred, the gasket was no longer capable of applying load onto the reaction plate to pull the stub from the bonded structure. The tilt angle when this occurred was only 5.2°. Insofar as the experiment for the angled pull-test conducted, the gasket did not escape from the housing in the presence of the largest gap tested resulting from a 3.4° tilt.

Nonetheless, this shows it is possible to load the pull-stubs at small off-angles which require lower loads to fracture. From the scarf joint experiment and FE analyses, the reduction in strength appears to be more severe for the initial increase of the scarf angle from 0° to 15°. However, this does not mean that the strength decreases linearly between these two angles. It

is possible for the strength to reduce to 88% of the tensile butt joint prior to 15°. The angle when the rate of the strength reduction plateaus to an almost constant value could be determined by trial and error through FE analyses with models of the appropriate scarf angle. Alternatively, this angle could be approximated from Equation 7-5 when σ_{app} reaches the minimum value. The normalised stress components can be obtained from Figure 5-8.

$$\sigma_{app} = \sqrt{3}\tau_0(\sigma_{vm}^N + m\sigma_m^N) \qquad \text{Eqn. 7-5}$$

It is important that the reduction in strength caused by off-normal loading is not mistaken as a loss of durability in the adhesive. By knowing the hydrostatic sensitivity of the adhesive, *m* and the ratio of stress components affecting the yield of the joint, the inherent shear yield strength, τ_0 of a bond could be estimated from Equation 7-6. This equation removes the effect of off-normal loading on the bond and is obtained by rearranging the linear Drücker-Prager criterion given in Equation 2-1.

$$\tau_0 = \frac{(\sigma_{vm}^N + m\sigma_m^N)\sigma_{app}}{\sqrt{3}} \qquad \text{Eqn. 7-6}$$

The inherent shear yield strengths of the scarf joints are determined by applying their fracture strength to Equation 7-5 to produce the plots in Figure 7-4. With the exception of the trend line for the conditioned joints without silane (Cond. Prep. C), the slopes of the trend lines fitted through the other plots are close to zero and as such, the θ-term in the trend lines are negligible.

By removing the θ-term from the linear trend line functions, the inherent shear yield strength becomes independent of the scarf angle, which can be translated to independence from the off-normal loading angle. This shows that Equation 7-6 has removed the off-normal loading effect from the joints to produce the inherent shear yield strength of the bond.

The slope for the conditioned joints with silane is the steeper than the rest because of the increased fracture strengths for the 30° and the lap-shear joints. Nonetheless, the slope at 0.0632 only causes a maximum of 5.8 MPa increase in the estimated shear yield strength of the 90° (lap-shear) joint. Since the pull-stub in the PATTI test configuration will never be loaded at an off-angle more than 3.4°, the θ-term for this trend line function can be ignored.

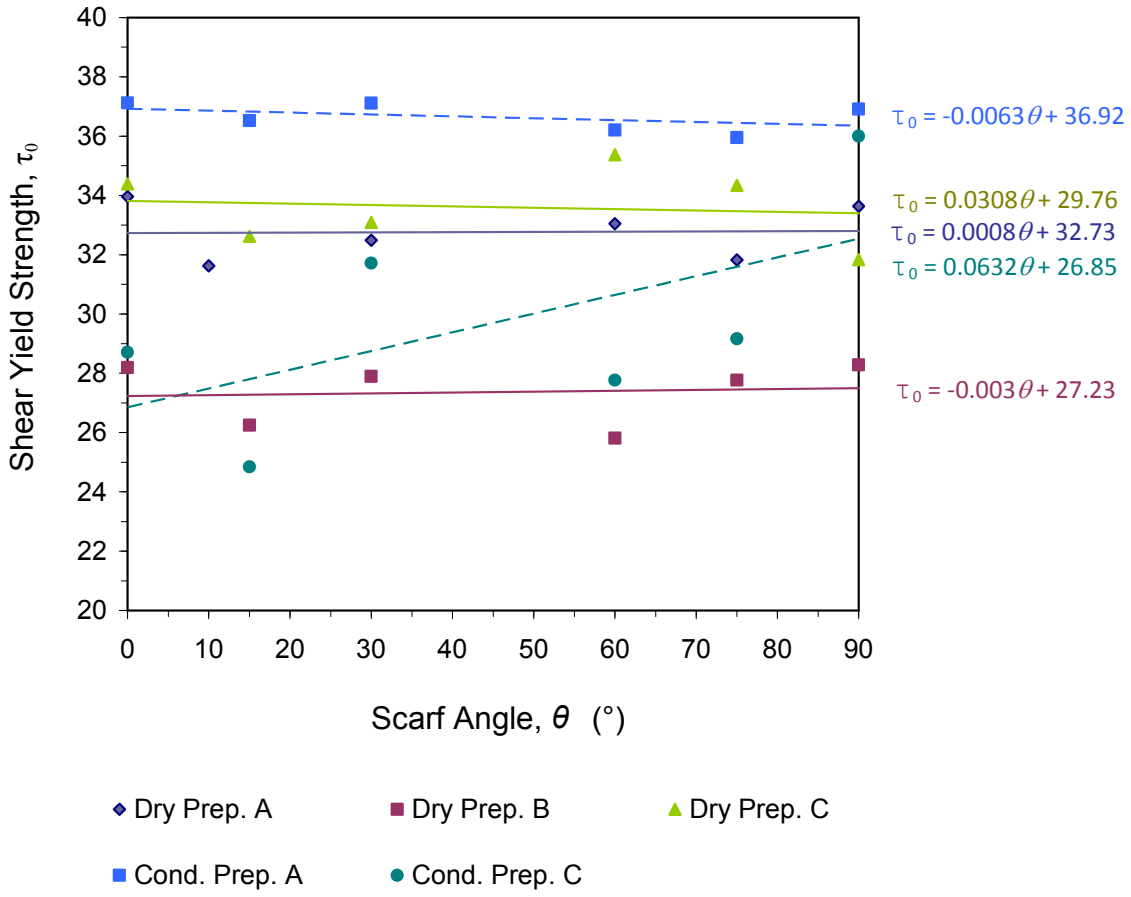

Figure 7-4: Plot of shear yield strength of joints after removing off-normal loading effect

7.3.3 Panel Strength Prediction

Predictions of the pull-off strength for all panel tests, tapered and uniform, were performed using the calibrated critical distance in conjunction with the maximum strain failure criterion and the predicted strengths are plotted in Figure 7-5. The FE models used for

all these prediction were presented in Sections 5.3 and 5.4. The experimental results and the strength prediction of the panels were all lower than the fracture strength of the tensile butt

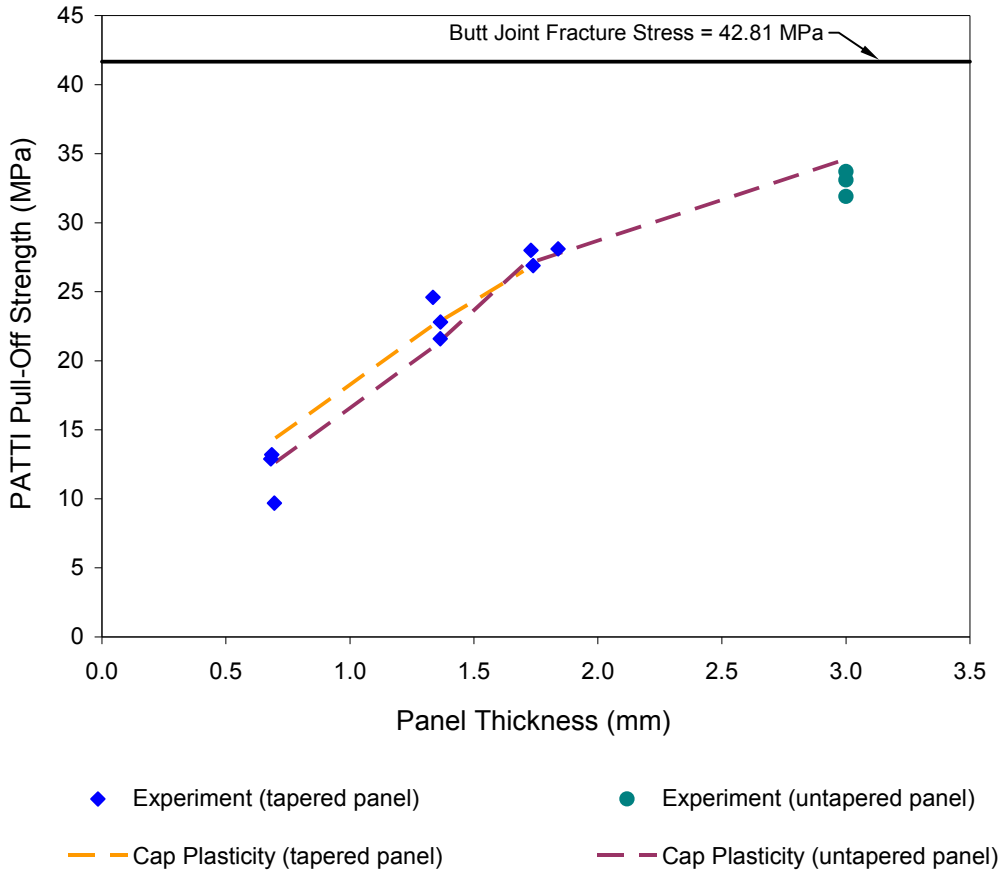

Figure 7-5: Plot of experimental and FE prediction of the PATTI pull-off strength versus the underlying panel thickness and their reduction from the fracture strength of the tensile butt joint.

joint. Introducing the additional layers of Hysol adhesive between the aluminium alloy sections of the "*Test-Disc*" and *"Pull-Stub"* did not change the predicted strength from the uniform panel models that combined the two sections. Likewise, the introduction of the 0.2 mm overcut into the uniform panel models did not affect the pull-off strength of the panel and only increased the predicted strengths by a negligible amount of 0.62 MPa. The highest von Mises stress in the Aluminium alloy sections of the uniform panel models was 430 MPa which is less than the typical tensile yield strength (503 MPa) of Aluminium alloy 7075 T6.

It is interesting to observe that during elastic deformation the strain was approximately uniformly distributed through the thickness of the adhesive. As plastic deformation proceeded, strain began to concentrate on the lower corner and spread radially. The radial propagation of strain in the 0.7 mm uniform panel model is confined within a very thin layer at the interface, as shown in Figure 7-6. As the adherend thickness increases, the strain

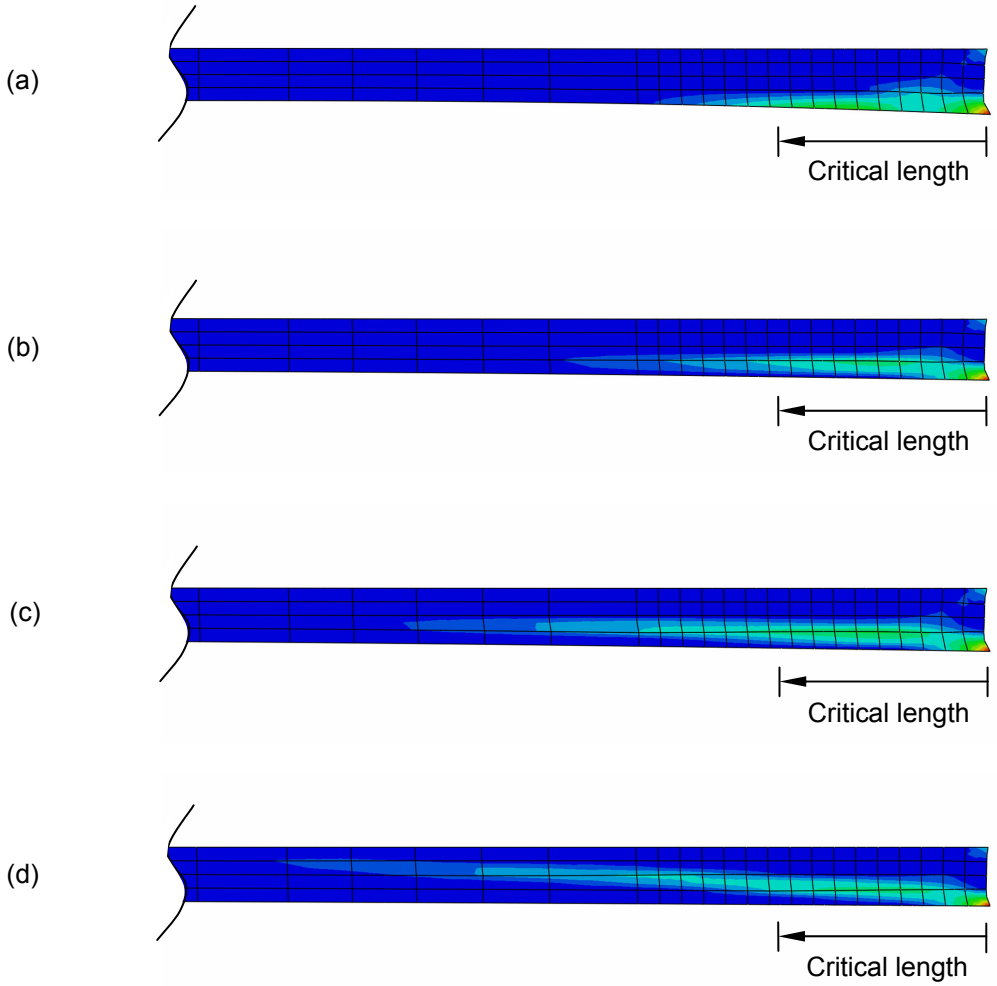

Figure 7-6: Strain distribution within the adhesive layer modelled with the modified Drücker-Prager/Cap Plasticity material for a) 0.7 mm b) 1.3 mm c) 1.7 mm and d) 3.0 mm uniform panels at failure.

localisation shifts towards the midlayer of the adhesive. When the panel thickness exceeds 10.0 mm, the predicted strength and strain distribution of bonded panels show similarity to the tensile butt joint.

Although the applied load on the panels were never as high as the tensile butt joint, the magnitudes of the maximum stress across the bondline of the uniform panel models, at approximately 40 MPa, are closer to the fracture strength of the butt joint and are similar for all panel thicknesses. These maximum stresses concentrate towards the edge of the adhesive at failure as shown in Figure 7-7 and the length spanning over them increases with the thickness of the panels. Due to the linear Drücker-Prager yield surface in the material model, these maximum stresses at failure reflect the yield stresses. From the observation that the

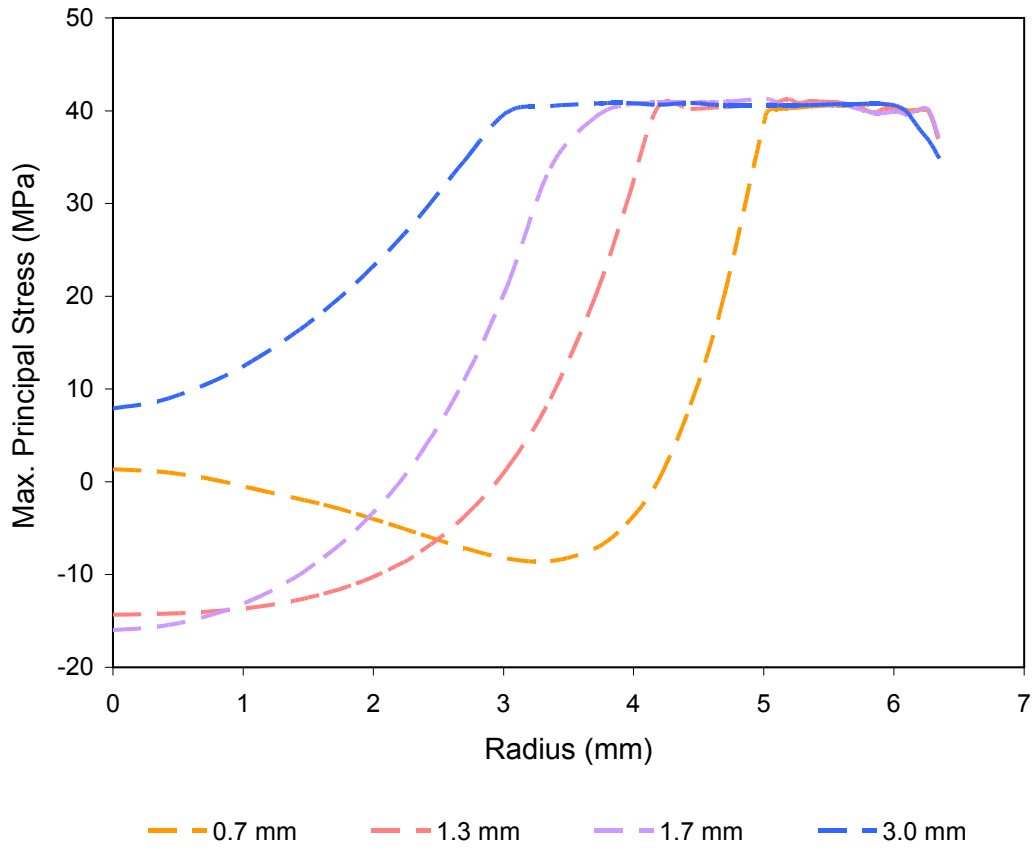

Figure 7-7: Maximum principal stress distribution across the adhesive when modelled through the modified Drücker-Prager/cap plasticity material

maximum stresses are less than the strength of the tensile butt joint, it is suspected that the loading mode on the adhesive within the panels is no longer pure tensile as it was within the butt joint. This is based on the assumption that the yield strength of the adhesive will decrease when the loading changes from tensile to shear as described by the quadratic stress criterion [52, 53].

The strength predicted from the 0.7 mm tapered model was higher than the uniform model. On the other hand, the strength predicted from the 1.7 mm tapered model is similar to the uniform model. The predictions from both uniform and tapered panel models are very close, indicating the panels of constant thickness are able to give good estimate for the pull-off strengths of the tapered panels.

The FE results confirm the earlier observations from the tapered panel experiments that the adherend thickness plays a significant role on the pull-off strength of the PATTI tests. With this knowledge, the reduction caused by the adherend thickness can be factored into the measured strength in the method presented in the next sub-section 7.3.3.1.

7.3.3.1 Effects of Adherend Thickness and Taper on the Pull-Strength

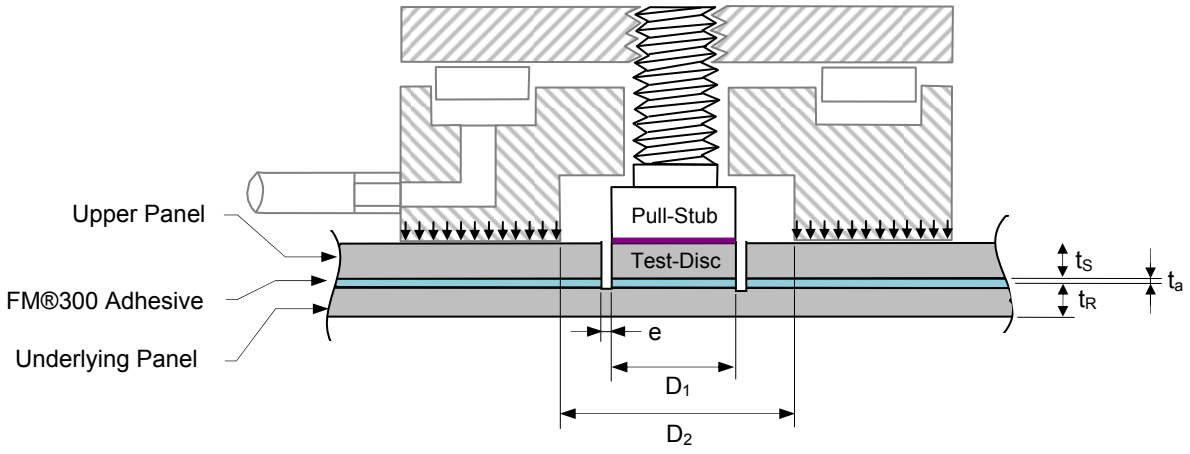

Figure 7-8: Supported and unsupported areas of the bonded panel during pull-tests.

The PATTI piston prevents the bonded panel from lifting at $D_2/2$ (=12.75mm) radius onwards when the Test-Disc was pulled off the underlying panel as shown in Figure 7-8. This leaves an unrestrained radial clearance of $(D_2 - D_1)/2$ (=6.4mm) from the edge of the stub to the inner radius of the PATTI piston. Due to this lack of constraint over this gap region, the upper panel only provides some stiffening effect to the bonded panel. As a result, the area of the panel, D_1+e, between the stub and the inner edge of the piston can deflect freely during the PATTI test. Thinner panels with lower bending stiffness accentuate this deflection.

The curvature due to the lower bending stiffness of the thin panels induces strain in the adhesive near the edge of the bond interface and causes failure at lower loads. Due to the strain concentration at that location, fracture tends to initiate and propagate along the lower bond surface and result in interfacial failure as shown in Figure 7-9. In comparison to the case of thin adherends, the curvature of a thicker adherend panel is less pronounced during loading

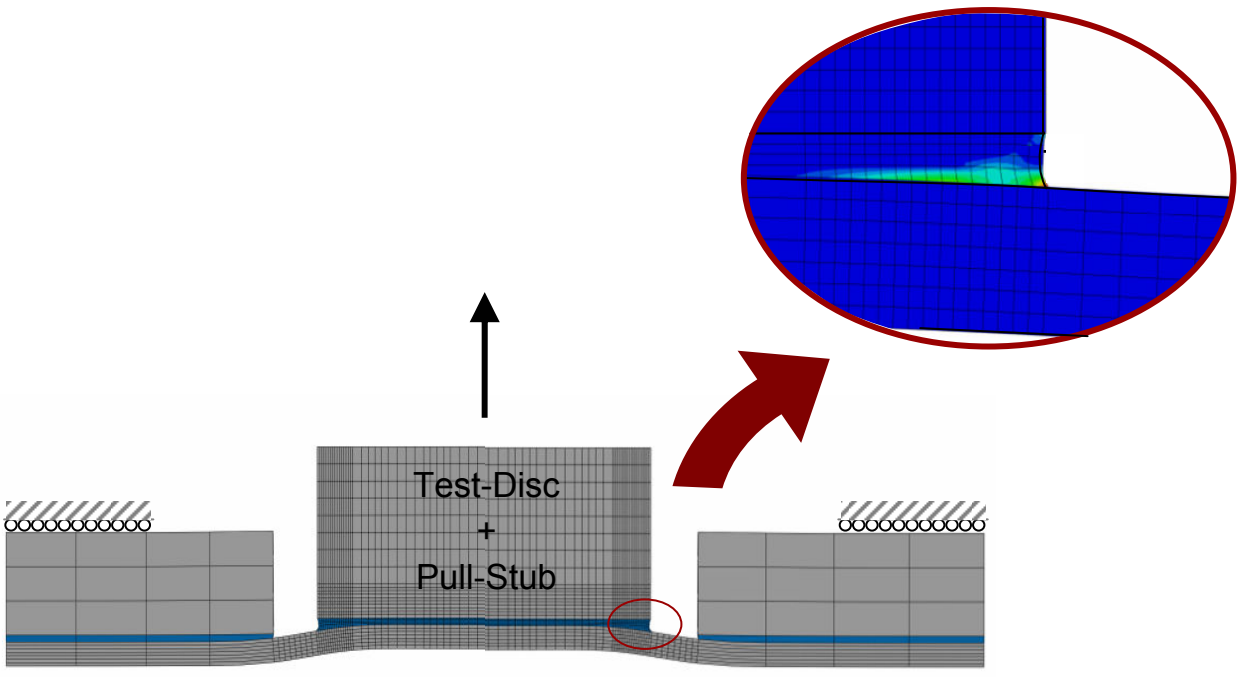

Figure 7-9: View of the PATTI test during loading showing the deflection and the strain distribution causing mixed cohesive-interfacial failure at the thin underlying panel section.

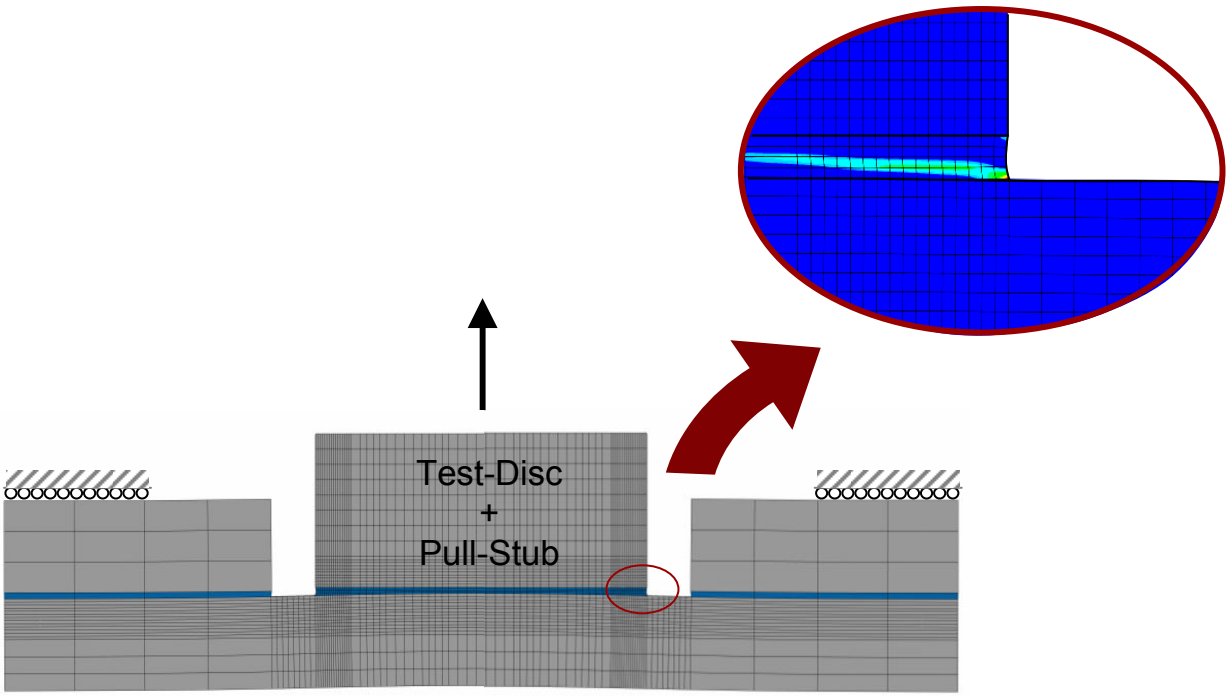

Figure 7-10: View of the PATTI test during loading showing the deflection and the strain distribution causing cohesive failure at the thick underlying panel section.

and as such failure tends to propagate along the mid-plane of the adhesive. This results in cohesive failure as illustrated in Figure 7-10

Unlike the uniform panel where the strain concentration in the adhesive is uniformly distributed around the edges, the strain in the tapered panel concentrates at the radial edge over the '*thin*' panel region as shown in Figure 7-11a because the '*thin*' region has a lower bending stiffness which allows for more deflection than the '*thick*' region. The '*thick*' region has a higher bending stiffness which enables it to resist more deflection and sustain higher load than the '*thin*' region. Consequently, it is expected for pull-tests conducted on a sufficiently thin tapered edge region to have a higher fracture strength compared to tests on uniform regions of the same thickness.

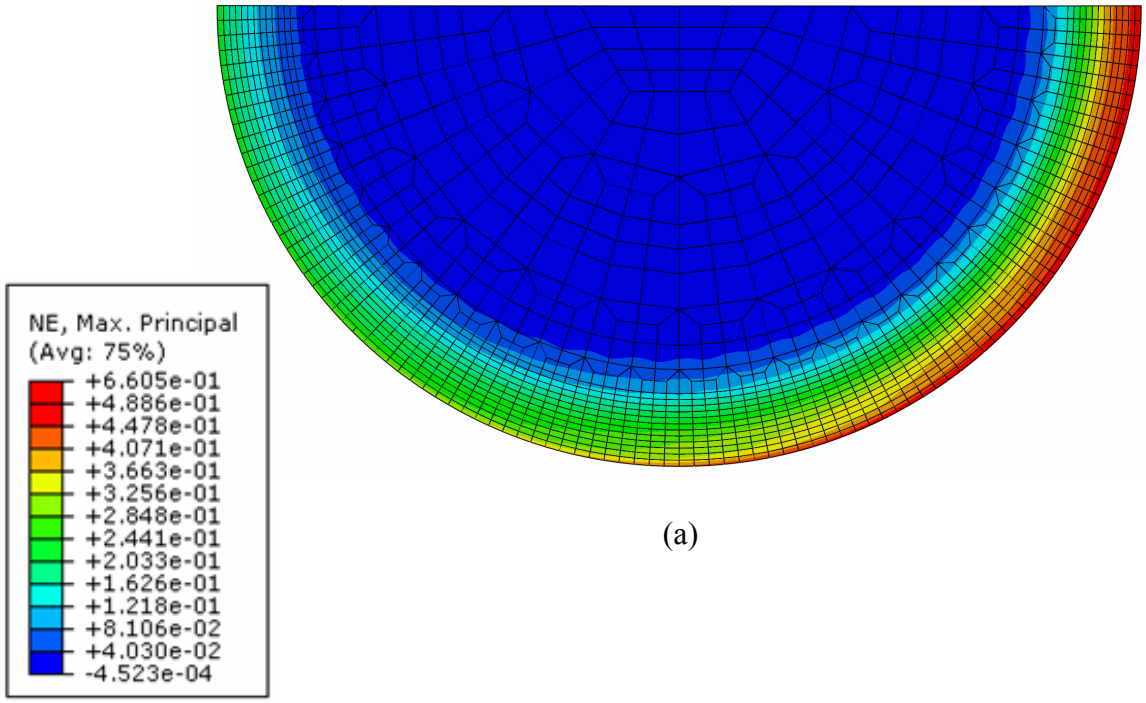

(a)

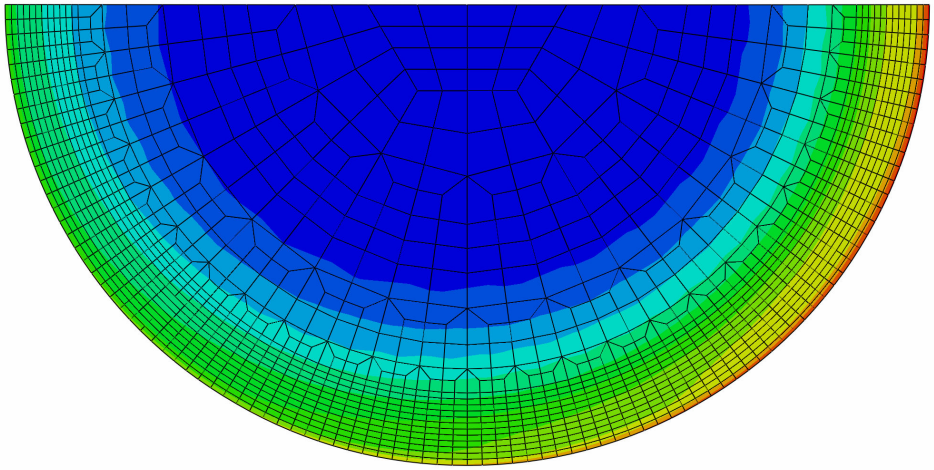

(b)

Figure 7-11: Strain distribution of the adhesive layer at the lower interface of the a) 0.7 mm and b) 1.7 mm tapered models

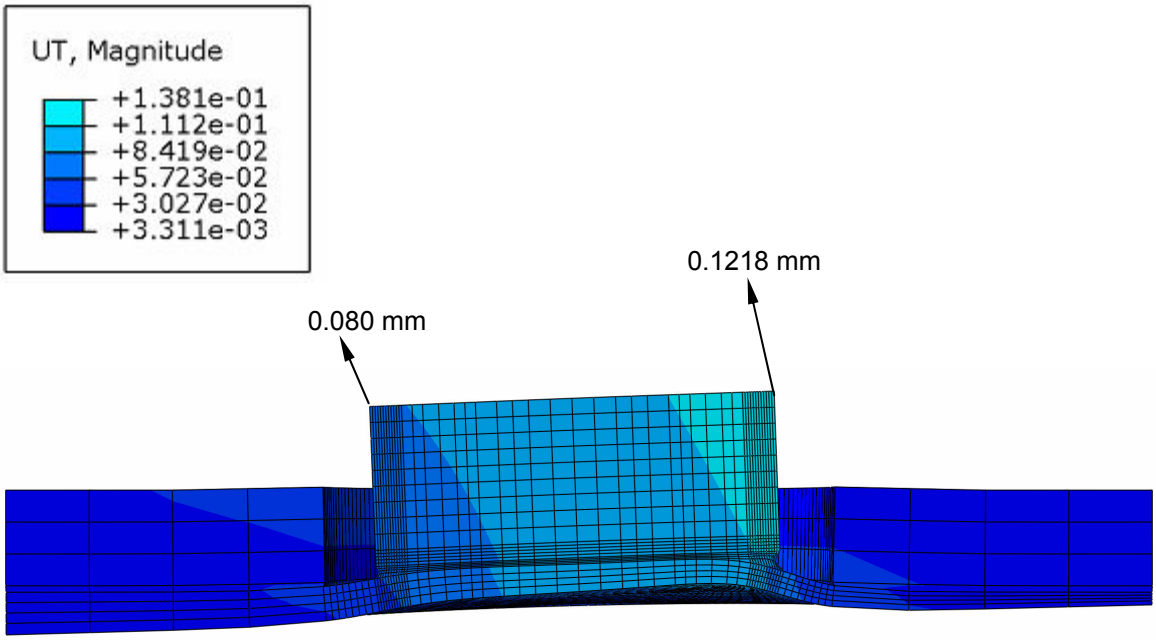

(a)

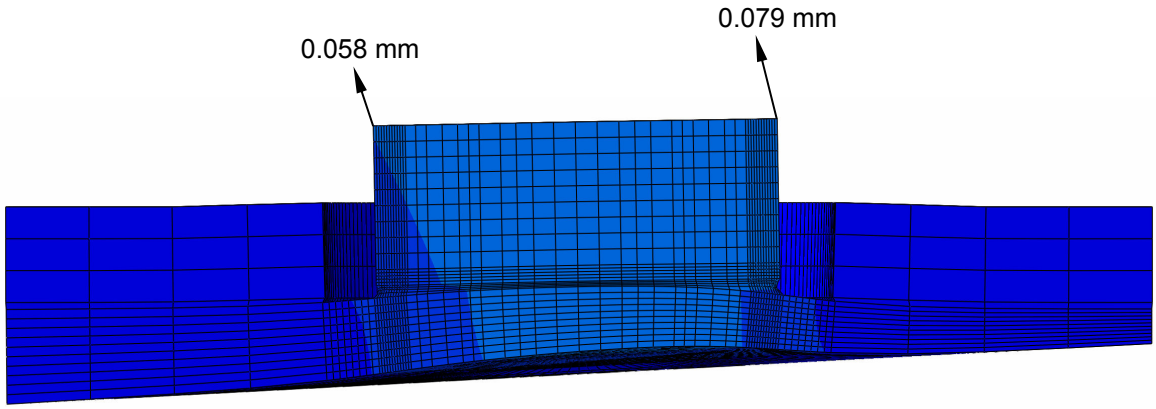

(b)

Figure 7-12: Comparison between the difference in deflection at the *'thin'* and *'thick'* regions for the a) 0.7 mm and b) 1.7 mm tapered edge panel. (Deformation in figures have been scaled by 10× for ease of visualisation)

not significantly different from *'thick'* region. The smaller difference of deflection between the end regions reduces the peeling effect on the bond as shown in Figure 7-12b. The difference between the deflections was reduced to 26% for the 1.7 mm tapered panel model.

Consequently, the strain becomes more evenly distributed along the edges of the bond as shown in Figure 7-11b and the loading on the bond become more akin to the uniform panel of the same thickness. As a result, pull-test on thick tapered edge panel produces cohesive fracture surfaces as shown in Figure 4-8b.

The good correlation between the FE predictions and the experimental data does not propose that the adhesive shear strength can be obtained from interfacial failure. The cohesive failures on the thick sections of the tapered edge panel show that the adhesion of the adhesive to the adherend is stronger than its cohesive strength. Consequently, the *"interfacial fracture areas"* observed on the thin sections of the panel could be considered as cohesive fracture because failure would occur along the same weak path in the same bonded panel. The following methodology to infer the adhesive shear strength in this thesis assumes that there is a very thin layer of adhesive (invisible to the naked eye) present on the exposed adherend interfaces and considers all PATTI tests to have failed by cohesion.

The strain distributions from the FE models compliments the experimental data presented in Figure 7-5 by showing that the underlying adherend thickness has a significant effect on the pull-off strengths measured from the PATTI tests. The intrinsic shear strength of the adhesive can be interpreted from the pull-test measurements by accounting for the effect of the adherend thickness. To this end, a scaling parameter, k, is defined as the ratio of the adhesive shear strength to the pull-off strength from the actual PATTI tests or the FE panel models.

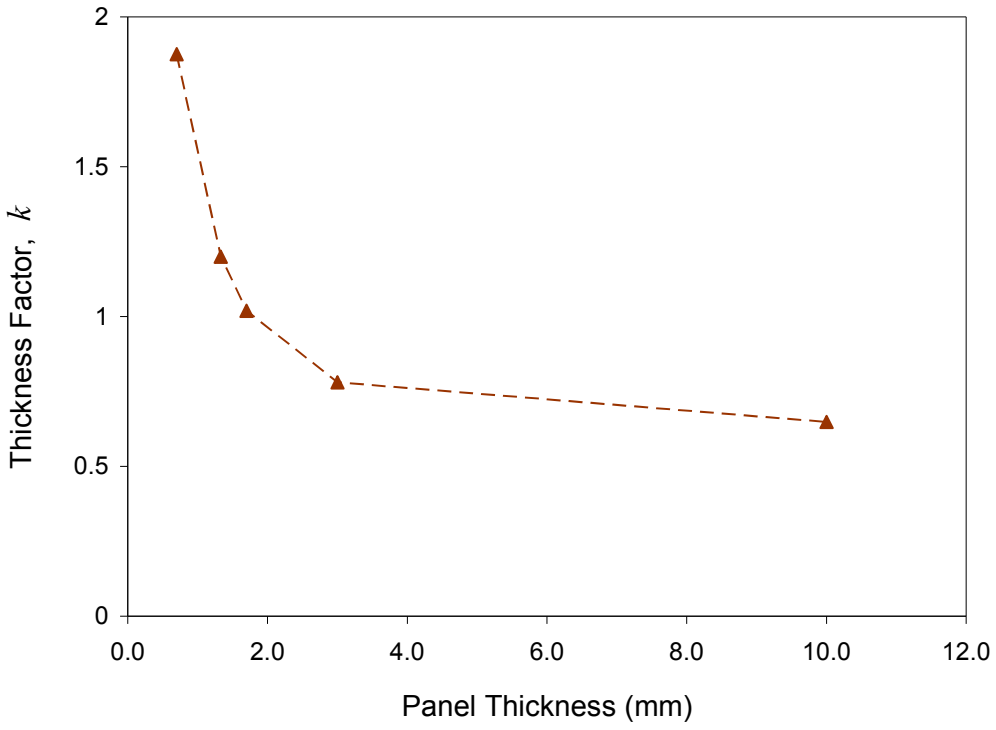

Figure 7-13: Scaling parameter, *k* for different panel thickness

In the following description, the scaling parameter, *k* was calculated for the specific adhesive-adherend configuration using the FE panel models incorporated with the modified Drücker-Prager/cap plasticity material. The *k* values for various panel thicknesses are presented in Figure 7-13. This shows the importance of establishing the constitutive characteristics of the adhesive bonds because it allows these scaling parameters to be derived from FE analyses instead of the actual pull-test. These FE analyses provide a simple, economical and efficient method to derive the scaling parameters for different pull-test configurations without the need to manufacture different panel configurations for testing.

The shear strength of the bond can be estimated by multiplying *k* to the experimentally measured PATTI pull-off strength, σ_{PATTI} according to Equation 7-7.

$$\tau = k\sigma_{PATTI} \qquad \text{Eqn. 7-7}$$

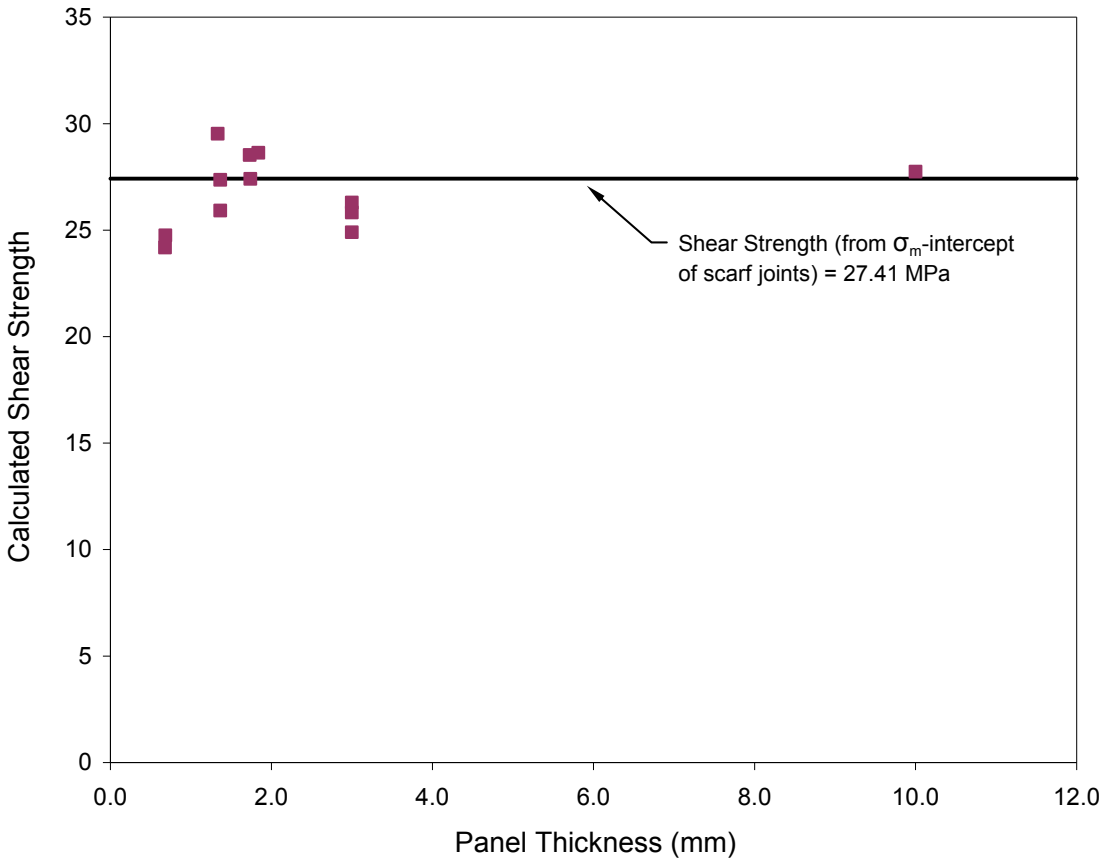

Figure 7-14: Comparison of calculated shear strengths for different panel thicknesses with adhesive shear strength.

The shear strength calculated from Equation 7-6 for different panel thicknesses is plotted in Figure 7-14 for comparison with the adhesive shear strength. The adhesive shear strength value is determined from the σ_{vm} -intercept of the dry scarf joints with surface preparation Method B plot in Figure 6-2

The shear strengths interpreted from the experimental pull-off strength off the panels range between ±10% of the shear yield strength of the adhesive. This shows that the method described in Equation 7-7 provides a novel technique to indirectly approximate the shear strength of the bond from the pull-test without the influence of the adherend thickness.

8 Cohesive Element Model

While using the modified Drücker-Prager/Cap Plasticity yield criterion in conjunction with the maximum principal strain failure criterion are found suitable for predicting the PATTI pull-off strengths on panel of different thickness, this method requires detailed calibration to determine the characteristic distance. An alternative approach is to model cohesive failure of bonded joints using cohesive elements. By incorporating fracture mechanics to describe the damage evolution as energy dissipated per unit area through a stress-displacement relationship [50], the cohesive element approach alleviates the problem of mesh dependency.

The built-in functions in ABAQUS describe the damage evolution of the cohesive elements as a linear or exponential profile. The tabular softening function allows the damage evolution to be described by any other types of profile.

This chapter first evaluates the strength predictions of PATTI tests on constant thickness panels with linear degradation model then compares the results to the predictions by the cap plasticity material model and the experimental data. Other degradation profiles are then implemented to determine the effect of cohesive law shape on the predicted strength.

8.1 Cohesive Element Formulation

8.1.1 Linear Damage Evolution

Detailed description of the cohesive element formulation can be found in the report by Davila and Camanho [54]. Among different traction-separation relationships, the linear cohesive model is commonly used due to its simplicity. The profile of a cohesive element

under pure mode loading is shown in Figure 8-1. The cohesive elements in ABAQUS are defined through the following material properties:

K = penalty stiffness for all modes of loading

N = Mode I Failure Strength (max. traction under Mode I)

S = T = Mode II and III Failure Strength (max. traction under Mode II and III)

G_{iC} , $_{i=I,II,III}$ = Mode I, II and III Fracture Toughness (area under the traction curve)

The FM300 adhesive was treated as an isotropic material with identical Mode II and Mode III properties.

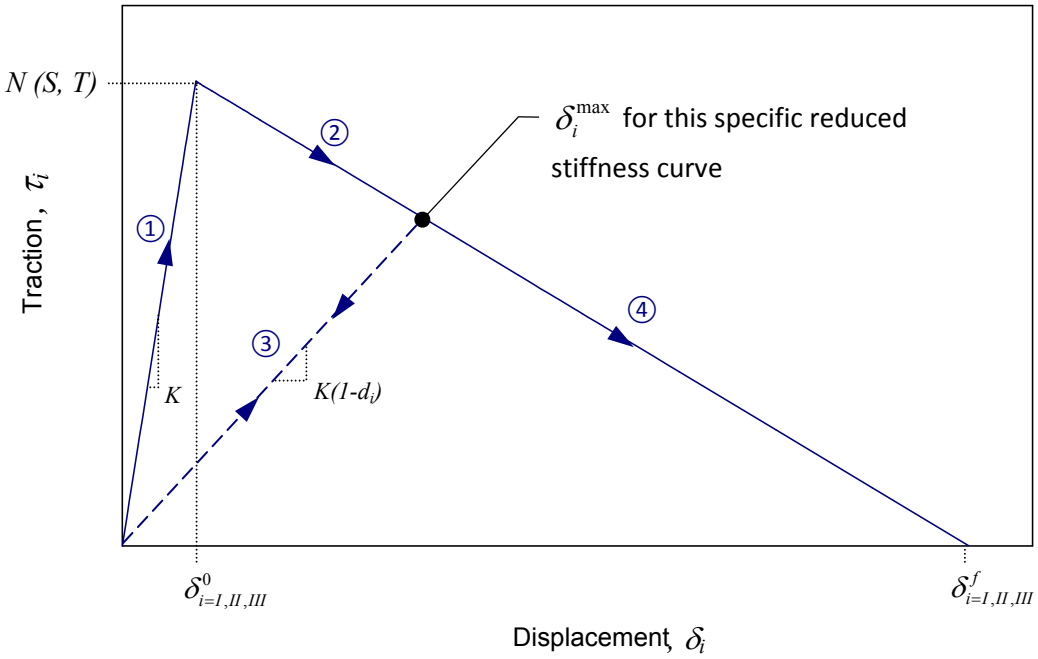

Figure 8-1: Typical loading behaviour of a cohesive element (*i=I, II, III; denotes the loading modes in pure normal, 2nd shear and 3rd shear respectively)*

A cohesive element will load and unload along the path marked ① until it reaches the maximum traction at the initial damage displacement, $\delta^0_{i=I,II,III}$. This point signifies the damage initiation for the element. The initial damage displacements for pure mode loading are calculated via Equation 8-1 and the tractions prior to damage initiation are calculated via Equation 8-2. The penalty stiffness, *K* was kept the same for all three loading modes.

$$\delta_I^0 = \frac{N}{K} \ , \ \delta_{II}^0 = \delta_{III}^0 = \frac{S}{K} = \frac{T}{K} \qquad \text{Eqn. 8-1}$$

$$\tau_i = K\delta_i \ , \ i = I, II, III \qquad \text{Eqn. 8-2}$$

After damage initiation, the evolution of the damaged element follows the path marked ② and ④ until the displacement at ultimate failure, $\delta_{i=I,II,III}^f$. Since the fracture toughness represents the entire triangular area underneath the curve, $\delta_{i=I,II,III}^f$ can be calculated through Equation 8-3.

$$\delta_I^f = \frac{2G_{IC}}{N} \ , \ \delta_{II}^f = \delta_{III}^f = \frac{2G_{IIC}}{S} = \frac{2G_{IIIC}}{T} \qquad \text{Eqn. 8-3}$$

However, if the load on the damaged element is removed prior to failure, the element will unload along the path marked ③ at a reduced stiffness, $K(1-d_i)$. The reduced stiffness is governed by the damaged scalar, d_i given in Equation 8-4. The maximum relative displacement, $\delta_i^{\max}$ signifies the largest displacement for that specific reduced stiffness curve and is a displacement point between $\delta_{i=I,II,III}^0$ and $\delta_{i=I,II,III}^f$ for the damage evolution path (marked ② and ④).

$$d_i = \frac{\delta_i^f \left(\delta_i^{\max} - \delta_i^0\right)}{\delta_i^{\max}\left(\delta_i^f - \delta_i^0\right)} \ , \ i = I, II, III \qquad \text{Eqn. 8-4}$$

When loaded again, the damaged element will have linear elastic behaviour along the same reduced stiffness curve marked ③ until it reaches $\delta_i^{\max}$ where the corresponding traction marks the maximum traction for the reduced stiffness curve. The traction along the entire damage evolution path and the reduced stiffness elastic curve is calculated via Equation 8-5 where $\delta_i^{\max}$ marks the upper limit for any specific reduced elastic curve. This describes the damage evolution as a linear degradation.

$$\tau_i = K(1-d_i)\delta_i \ , \ i = I, II, III \qquad \text{Eqn. 8-5}$$

The loading and damage responses described above for cohesive elements under pure mode loading also apply for mixed-mode loading. However failure criteria are required to determine the damage initiation and the ultimate failure of the cohesive elements under mixed-mode loading. The constitutive response of a cohesive element under mixed-mode loading is shown in Figure 8-2 where the shear response is treated to be isotropic.

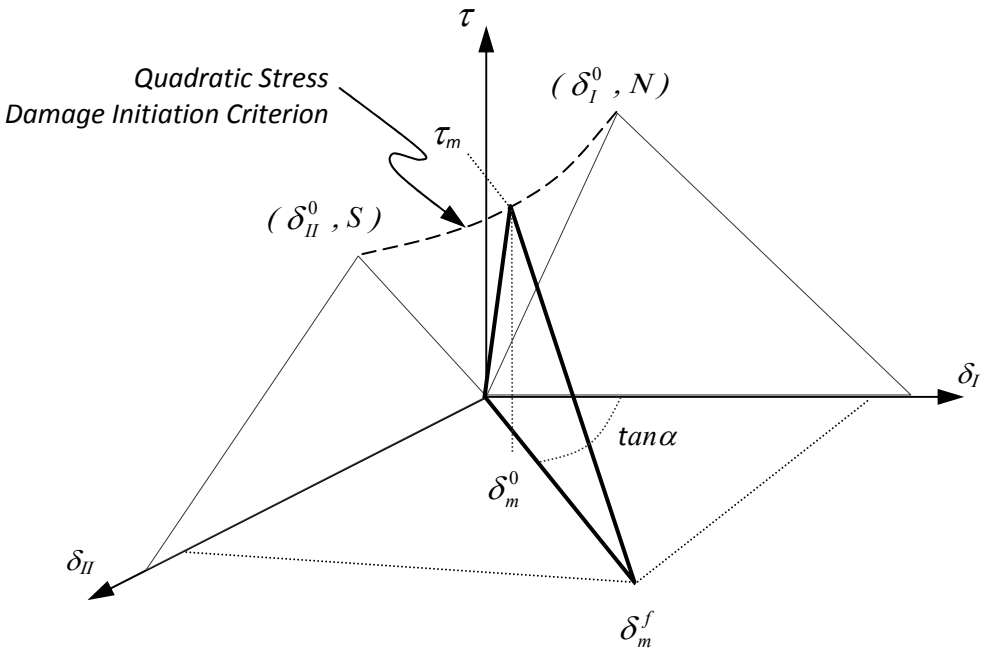

Figure 8-2: Constitutive response of a cohesive element under mixed-mode loading

The quadratic stress criterion given in Equation 8-6 was chosen [53] to determine the damage initiation stress for the mixed-mode loading of the cohesive elements in this chapter.

$$\left(\frac{\langle \tau_I \rangle}{N}\right)^2 + \left(\frac{\tau_{II}}{S}\right)^2 = 1 \qquad \text{Eqn. 8-6}$$

whereby τ_I and τ_{II} represent the pure mode tractions at the time of loading. Equation 8-6 describes an ellipse in the τ_{II}-τ_I plane shown in Figure 8-3. The maximum mixed-mode traction, τ_m is calculated according to Equation 8-7. In the case of the FM300 adhesive, the

magnitude of τ_m decreases along the elliptical curve from the normal traction, $N = 43$ MPa to the shear traction, $S = 27$ MPa.

$$\tau_m = \sqrt{(\tau_{I\,m})^2 + (\tau_{II\,m})^2} \qquad \text{Eqn. 8-7a}$$

$$= \sqrt{\frac{1 + \tan^2 \phi_1}{\left(\frac{1}{N^2}\right) + \frac{\tan^2 \phi_1}{S^2}}} \qquad \text{Eqn. 8-7b}$$

$$\phi_1 = \tan^{-1}\left(\frac{\tau_{II\,m}}{\tau_{I\,m}}\right) \qquad \text{Eqn. 8-7c}$$

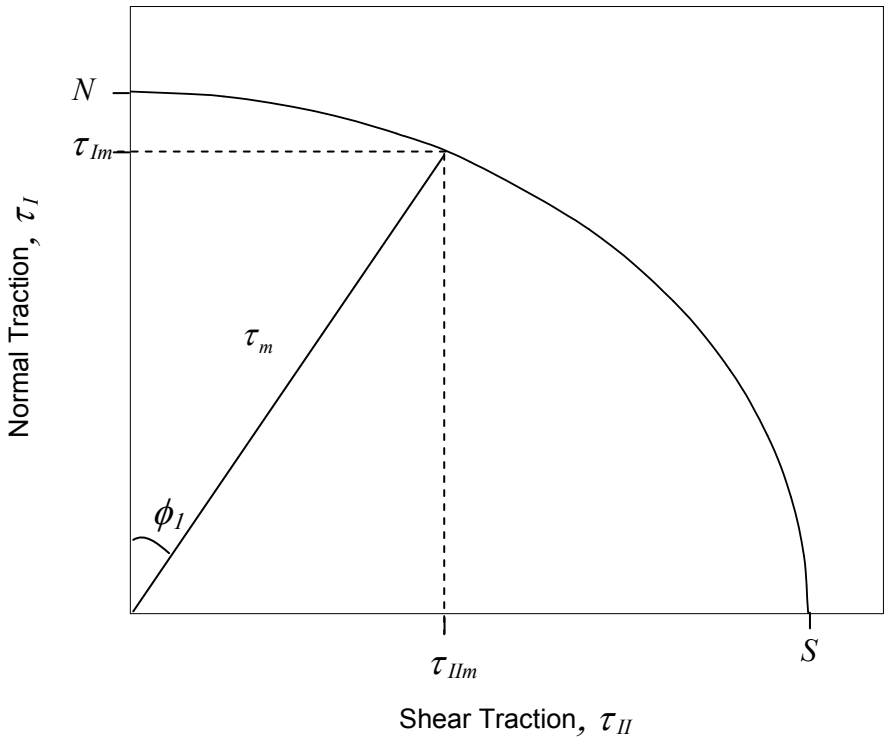

Figure 8-3: Elliptical curve describing the quadratic stress failure criterion for damage initiation

The mixed-mode displacement at damage initiation, δ_0^m can be calculated from the individual pure mode stress components and the mode-mix traction ratio, ϕ_1 according to Equation 8-8.

$$\delta_0^m = \sqrt{\left(\frac{\tau_{Im}}{K}\right)^2 + \left(\frac{\tau_{IIm}}{K}\right)^2} \qquad \text{Eqn. 8-8}$$

Alternatively, δ_0^m can also be calculated in terms of its individual pure mode initial displacements given in Equation 8-1 and the mode-mix displacement ratio, φ as given in Equation 8-9.

$$\delta_0^m = \delta_I^0 \delta_{II}^0 \sqrt{\frac{1+\varphi^2}{\left(\delta_{II}^0\right)^2 + \left(\varphi\delta_I^0\right)^2}} \qquad \text{Eqn. 8-9a}$$

$$\varphi = \frac{\delta_{II}}{\delta_I} \qquad \text{Eqn. 8-9b}$$

The mixed-mode fracture toughness of the material was determined through the power law criterion given in Equation 8-10 with $\alpha = 1$. From the power law equation, the mixed-mode displacement at failure, δ_f^m was calculated according to Equation 8-11.

$$\left(\frac{G_I}{G_C^I}\right)^\alpha + \left(\frac{G_{II}}{G_C^{II}}\right)^\alpha = 1 \ , \ \alpha = 1 \qquad \text{Eqn. 8-10}$$

$$\delta_f^m = \frac{2(1+\varphi^2)}{K\delta_m^0}\left[\left(\frac{1}{G_C^I}\right) + \left(\frac{\varphi^2}{G_C^{II}}\right)\right]^{-1} \qquad \text{Eqn. 8-11}$$

The cohesive material parameters for the FM300 adhesive are given in Table 8-1. The penalty stiffness was calculated by dividing the elastic modulus of the FM300 adhesive (666 MPa) by half the element thickness (0.05 mm). The damage initiation parameters were taken from the tensile and shear yield strength of the FM300 adhesive described in Section 6.2.1.

The damage evolution parameters were taken from the DCB and ENF results presented in Section 4.3.

Table 8-1: Material properties specified in ABAQUS for the cohesive elements with linear damage evolution

Stiffness	Damage Initiation (QUADS)		Damage Evolution	
K (MPa/mm)	N (MPa)	$S = T$ (MPa)	G_{IC} (N/mm)	$G_{IIC} = G_{IIIC}$ (N/mm)
13320	43	27	0.8	3.8

8.1.2 Non-Linear Damage Evolution

A method to change the damage evolution profile of the cohesive elements is by manipulating the softening index, n in the power softening law equation [52] previously given in Equation 2-7. When specified in terms of the cohesive element profile, the softening law then becomes Equation 8-12. The linear profile presented in Section 8.1 is produced when n = 1. The profiles resulting from non-unity n values are shown in Figure 8-4. In order for the intrinsic fracture strengths and energies of the FM300 adhesive to remain unchanged, the ultimate failure displacement of the cohesive element has to change to maintain the area underneath the damage evolution curve.

$$\tau_i = \tau_{\max}\left(1 - \frac{\delta_i - \delta_i^0}{\delta_i^f - \delta_i^0}\right)^n \qquad \text{Eqn. 8-12}$$

These evolution profiles were specified through their effective displacements in ABAQUS using a combination of the tabular softening and tabular mixed-mode functions. The parameters required for these functions are the damage variable d, the effective displacements $\left(\delta_i^f - \delta_i^0\right)$, the normalized mixed-mode ratio, ϕ_1 for the normal to total

effective shear traction and the normalised mixed-mode ratio, ϕ_2 for the first to second shear traction [74].

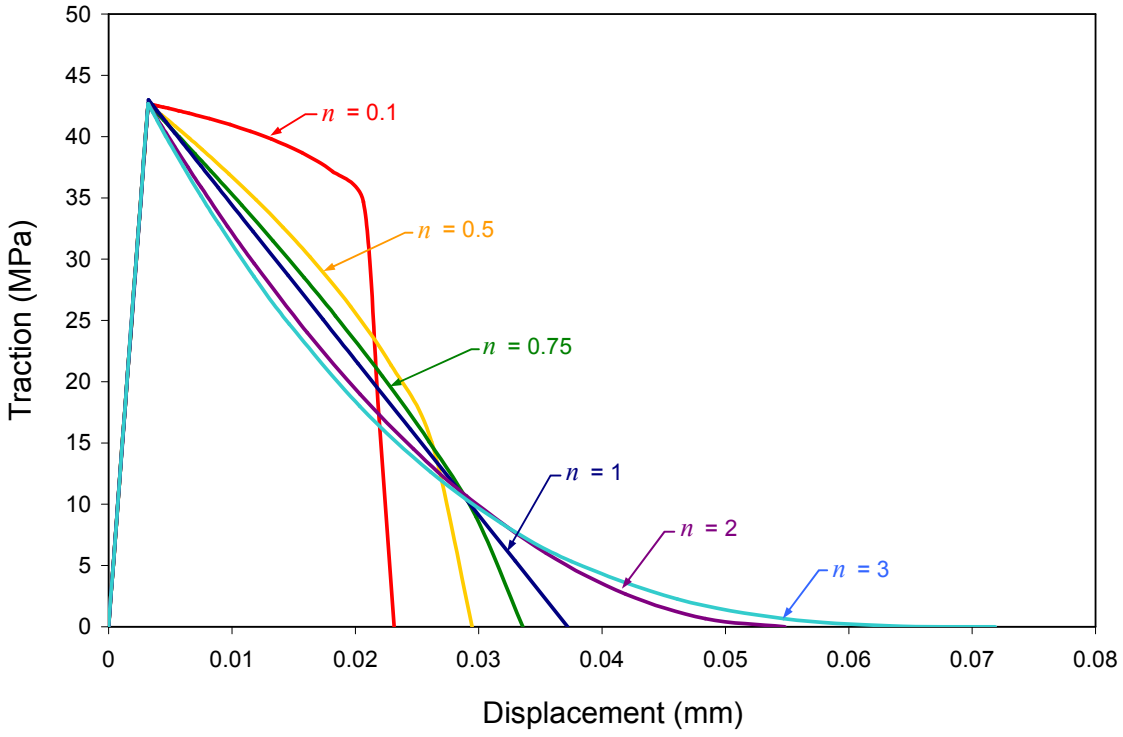

Figure 8-4: Comparison of damage evolution profiles produced by varying *n*

The graphical representation of the mixed-mode ratios is shown in Figure 8-5 and the values are normalised according to Equations 8-13 and 8-14. With the shear response of the FM300 adhesive set as isotropic, the radius of the curve within the $\tau_{II} - \tau_{III}$ plane is fixed at the maximum shear traction (= *S*). As such, the curve within the $\tau_I - \tau_{eff}$ is the same elliptical curve defined by the quadratic stress failure criterion in Figure 8-3 and remains the same for all angle of ϕ_2. Consequently, the remaining parameters d and $\left(\delta_i^f - \delta_i^0\right)$ had only to be tabulated in terms of ϕ_1.

$$\phi_1 = \left(\frac{2}{\pi}\right)\tan^{-1}\left(\frac{\tau_{II}}{\tau_I}\right) = \left(\frac{2}{\pi}\right)\tan^{-1}\phi_I' \qquad \text{Eqn. 8-13}$$

$$\phi_2 = \left(\frac{2}{\pi}\right)\tan^{-1}\left(\frac{\tau_{III}}{\tau_{II}}\right) \qquad \text{Eqn. 8-14}$$

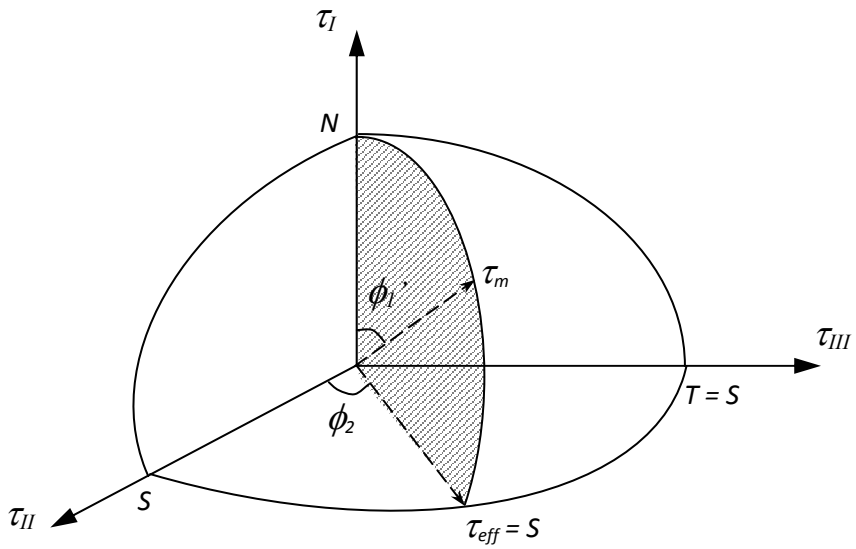

Figure 8-5: Graphical representation of the mixed-mode ratio ϕ_1 and ϕ_2

The previous Equations 8-9 and 8-11 use the displacement ratio, φ to calculate the initial and failure displacements for mixed-mode loadings. By specifying the same stiffness *K* for all the pure mode loadings, φ is shown to be equal to the traction ratio $\tan\phi_1$ by substituting Equations 8-2 into Equation 8-7c as shown in Equation 8-15.

$$\phi_1 = \tan^{-1}\left(\frac{K\delta^0_{II\,m}}{K\delta^0_{I\,m}}\right) \qquad \text{Eqn. 8-15}$$

$$\therefore \varphi = \tan\phi_1$$

The power softening law equation given in Equation 8-12 captures the softening tractions for different values of the index *n* in terms of the traction and opening displacement at damage initiation determined from the universal stiffness *K*. However, Equation 8-11 does not incorporate the index *n* in the calculation for the displacement at failure and only

calculates the displacements for n = 1. The degradation profile when n = 1 is a linear curve and the area beneath the curve is calculated through the formula for the area of triangle.

When $n \neq 1$, the size of the area under the evolution curve needs to be integrated from δ_i^0 to δ_i^f or summed as discrete trapezoidal segments as shown in Figure 8-6. For any values of n, the size of the area must remain constant as it represents the intrinsic fracture energy G_i^C of the material. In the following description, parameters with subscript 'i' belong to the intrinsic fracture energy.

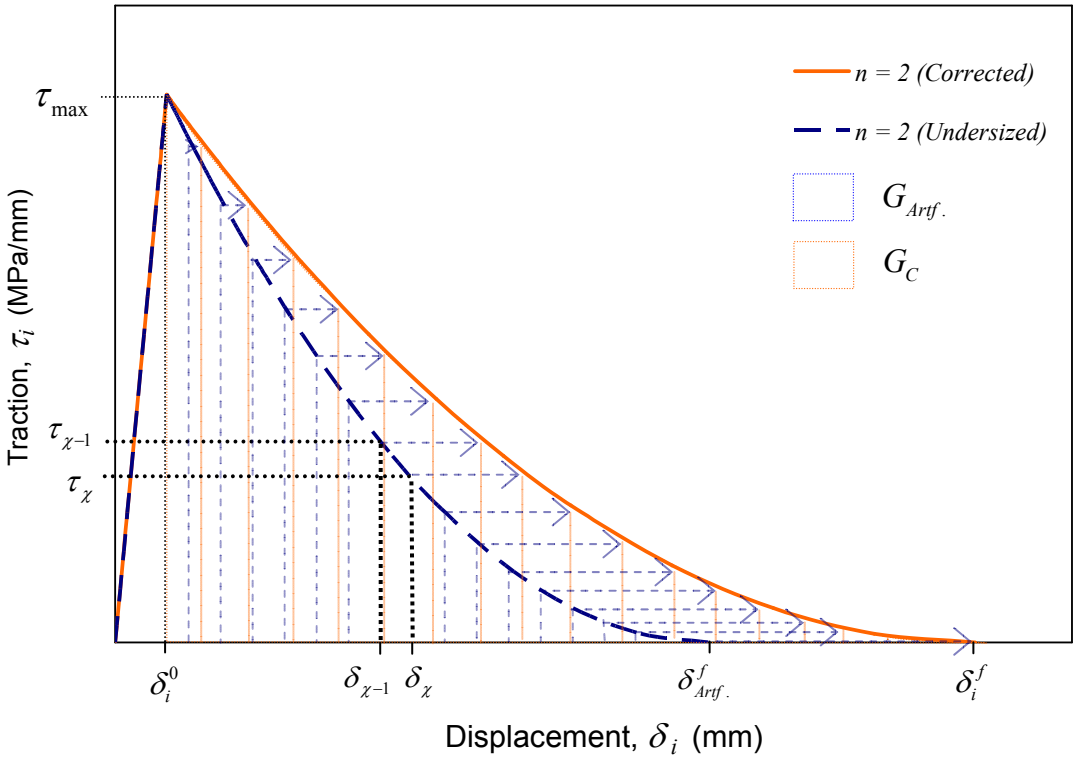

Figure 8-6: Maintaining G_C and calculating the effective displacement for all order of n

If Equation 8-11 is used with the softening law equation for any non-unity order of n, the area underneath the curve (dotted line) would deviate and result in an '*artificial*' fracture energy $G_{Artf.}^C$. The area of the '*artificial*' energy segment, $G_{Artf.}^{seg.}$ is calculated via Equation 8-16 where η represents the total number of segments and χ denotes the consecutive position

of the segment. The traction $\tau_{\max}$ and displacement δ_m^0 at damage initiation are used when $\chi = 0$.

$$G_{Artf} = \sum_{\chi=1}^{\chi=\eta} G_{Artf}^{seg.} \quad , \quad G_{Artf}^{seg.} = \frac{1}{2}\left(\tau_{\chi-1} + \tau_{\chi}\right)\left(\delta_{\chi} - \delta_{\chi-1}\right)$$

$$\chi = \frac{\delta_{Artf}^{f} - \delta_{i}^{0}}{\eta} \qquad \text{Eqn. 8-16}$$

In order to incorporate the effects of *n* into the failure displacements, a ratio γ of the intrinsic to '*artificial*' fracture energy is introduced in Equation 8-17.

$$\gamma = \frac{G_i^C}{G_{Artf.}^C} \qquad \text{Eqn. 8-17}$$

The individual discrete segments forming the '*artificial*' fracture energy is then multiplied by γ to scale the position of the displacements and produce the area segments for the intrinsic energy, $G_i^{seg.}$. The displacements for the intrinsic energy segments, $\delta_{\chi'}$ are calculated by rearranging Equation 8-16 to give Equation 8-18.

$$\delta_{\chi'} = \frac{2G_i^{seg.}}{\left(\tau_{\chi'-1} + \tau_{\chi'}\right)} + \delta_{\chi'-1}$$

$$\chi' = \frac{\gamma(\delta_{Artf.}^{f} - \delta_{m.}^{0})}{\eta} \qquad \text{Eqn. 8-18}$$

It should be noted that the tractions for the '*artificial*' and intrinsic energies are the same. The effective displacement $\left(\delta_i^f - \delta_i^0\right)$ for the tabular softening function in ABAQUS is obtained by subtracting δ_i^0 from $\delta_{\chi'}$. The critical failure displacement for the intrinsic energy curve is obtained from the displacement of the last segment, δ_η when the corresponding traction is zero.

Finally, the damage variable d_i to tabulate the softening table is determined according to Equation 8-19 where τ_i is calculated from the traction softening function given in Equation 8-12 and $\delta_{\chi'}$ from Equation 8-18.

$$d_i = 1 - \frac{\tau_i}{K\delta_{\chi'}} \qquad \text{Eqn. 8-19}$$

The tabulated data were generated for n = 0.1, 0.5, 0.75, 2 and 3. For each table, five sets of data with the same damage variables, effective displacements and ϕ_1 were specified for equal intervals of ϕ_2. Within each of these five sets, 19 angles of ϕ_1 at equal intervals were used to determine the damage variable and effective displacements. For each angle of ϕ_1, 20 pairs of damage variable and effect displacement were used to describe the damage evolution for that particular mixed-mode loading. An example of the tabulated data is shown in Appendix II.

8.2 Panel Strength Prediction

8.2.1 Linear Damage Evolution Profile

Unlike the cap plasticity material model that uses the maximum strain at a characteristic distance to predict the fracture load of the FE models, the cohesive element approach predicts the load-displacement response with the maximum load representing the fracture strength. The damage evolution of the cohesive elements allows them to fail after sufficient energy has been supplied such that when sufficient number of elements has failed, the ability of the model to carry load drops abruptly. This is comparable to the sudden

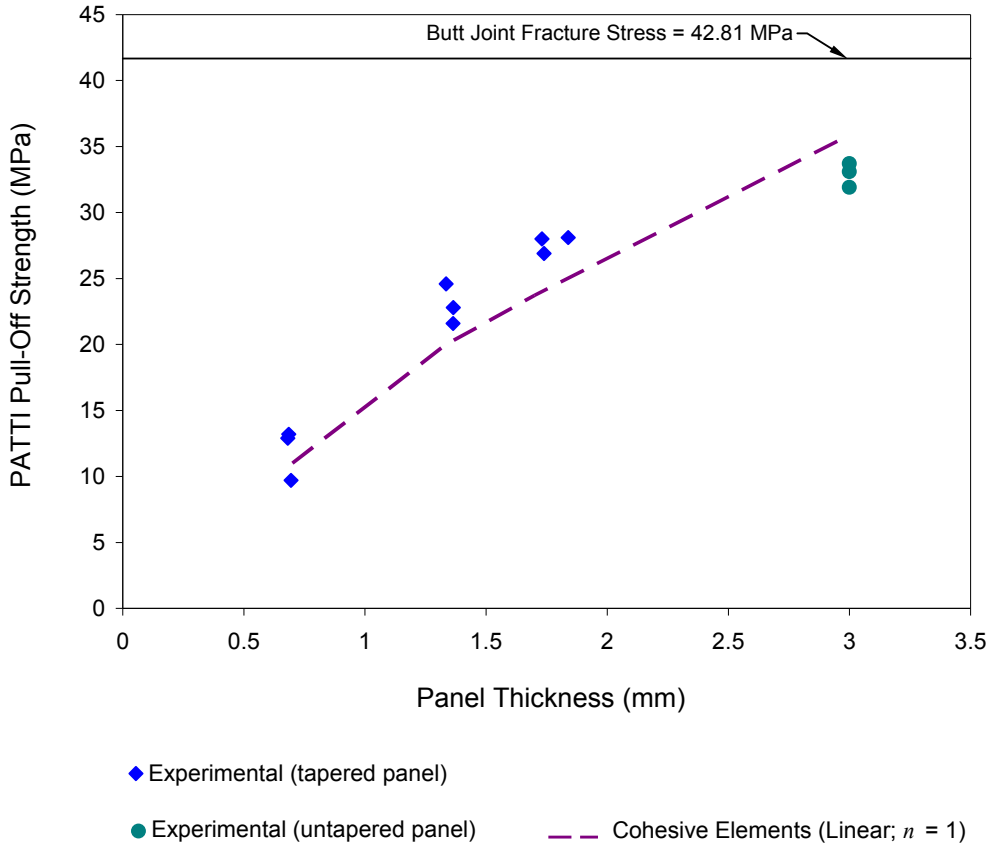

Figure 8-7: Strength prediction from uniform panel FE models with linear degradation cohesive elements

fracture of the bonds in the actual pull-tests after sufficient load has been applied to the reaction plate of the PATTI tester.

The strengths predicted from the uniform models with cohesive elements (n = 1) are plotted in Figure 8-7. The predicted strengths are up to 25% lower than the experimental data with the largest difference at the 1.7 mm panel thickness. The damage progression of the cohesive elements is monitored by the damage scalar variable, d_i which represents the ability of the elements to carry load.

The damage localizations within the adhesive section of the models just before fracture are shown in Figure 8-8. The damage scalar in the models does not diffuse through the thickness of the adhesive with increasing panel thickness like the strain distribution in the cap plasticity models. The length of the damage zone increases with the panel thickness. This

length is measured across cohesive elements that have exceeded the damage initiation point and whose strength has started to degenerate along the damage evolution profile as shown in Figure 8-9. The peak stresses in the gradients correspond to the maximum traction at damage initiation and the elements beyond are at advanced stages of degradation.

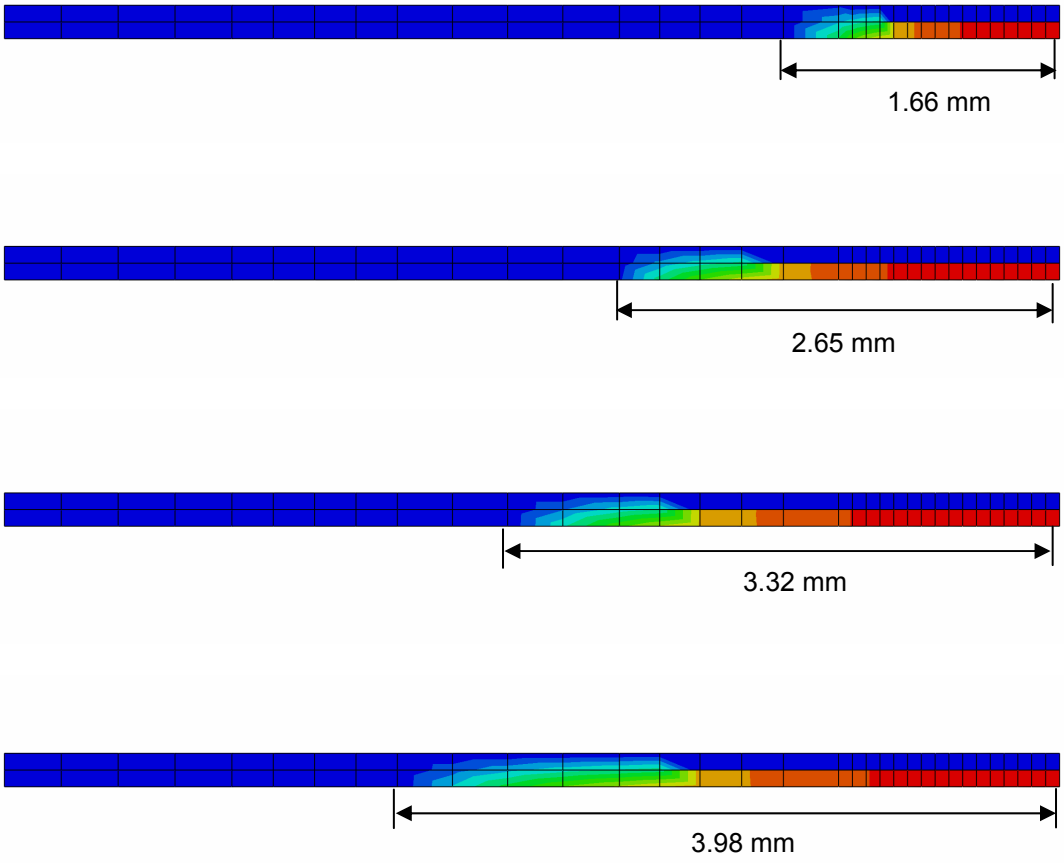

Figure 8-8: Length of damage zone at failure for a) 0.7 mm b) 1.33 mm c) 1.7 mm and d) 3.0 mm panel thickness

Using cohesive elements with linear damage evolution to model the FM300 adhesive underpredicts the fracture strength of the panels. Another method to improve the prediction is to change the damage evolution profile of the cohesive elements.

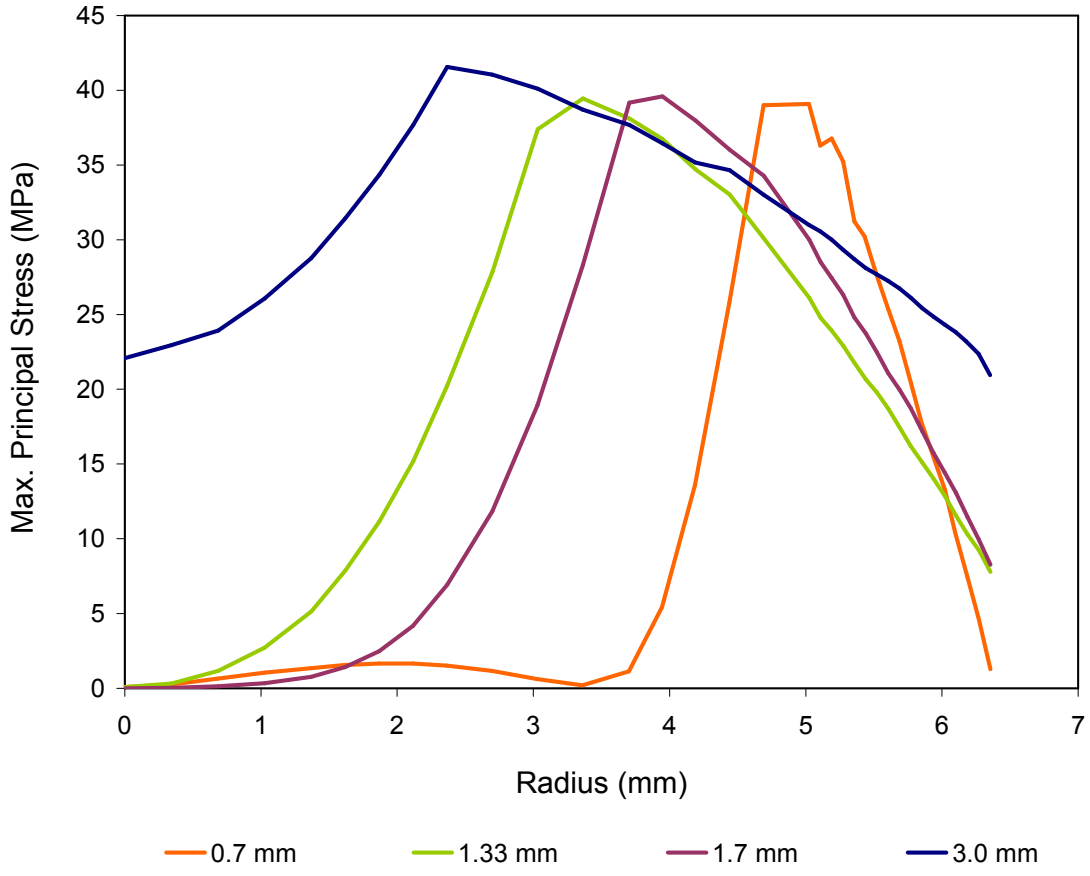

Figure 8-9: Stress gradient along radius of the model for each panel thickness

8.2.2 Non-Linear Damage Evolution Profile

The strengths of the uniform panels predicted with the cohesive element properties defined through the tabulated data are plotted in Figure 8-10. The damage profile where n = 0.1 showed the largest increase in strength from the predictions with the linear evolution profile (n = 1). As n increases from 0.1 to 3, the predictions showed a steady reduction in strength although the model using n = 1 gave a slight increase in strength. In fact, the predicted strength with n = 2 were very close to the predictions with n = 0.75. The same trend is observed for all panel thicknesses as shown in Figure 8-11.

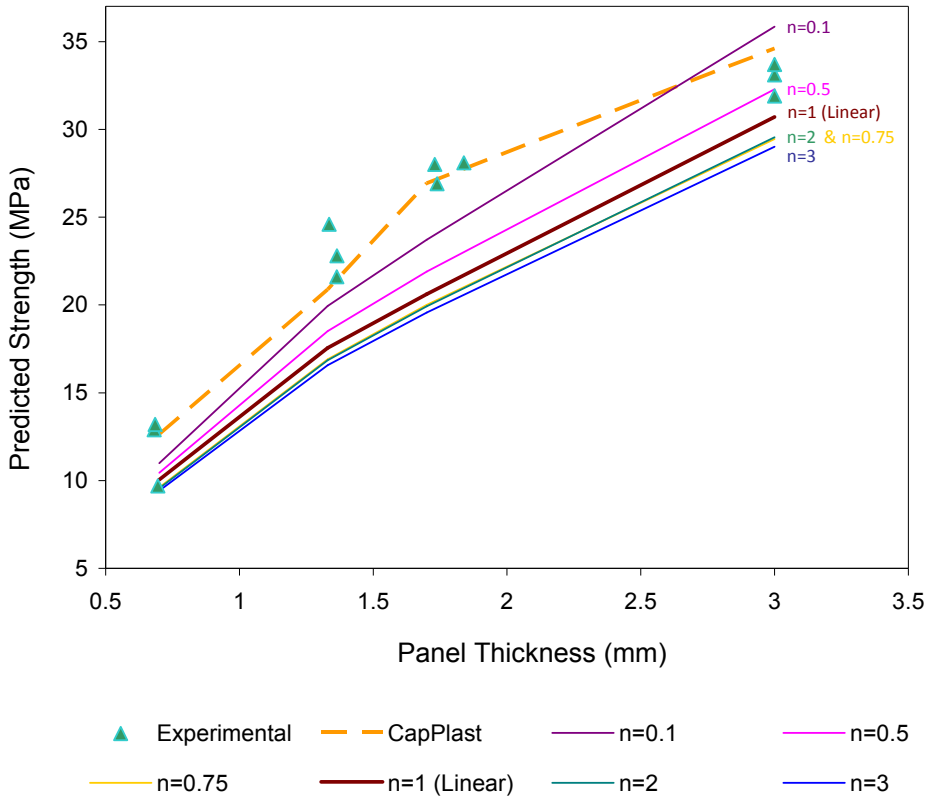

Figure 8-10: Strength predictions for uniform panel models using cohesive elements with non-linear damage evolution profiles

The trend of the damage zone length when the models attain maximum load are shown in Figure 8-12. The 0.7 mm model had the largest damage zone length range from 1.08 mm to 3.32 mm. The damage zone lengths trends for the 1.33 mm and 1.7 mm models ranges between 1.91 mm to 3.32 mm. The damage lengths for the 3.0 mm models were mostly constant within 3.65 mm to 4.23 mm.

The trends of the damage zone lengths do not show exact correlation with the predicted strengths in Figure 8-11. With the exception of the 3.0 mm panel, the damage zone length rises with increasing n which relates to the general decrease in predicted strength. It is observed that the smallest damage zone lengths for these three panels corresponds to their highest predicted strengths when n = 0.1. The damage zone lengths of the 3.0 mm panel are relatively constant in comparison with the other panels.

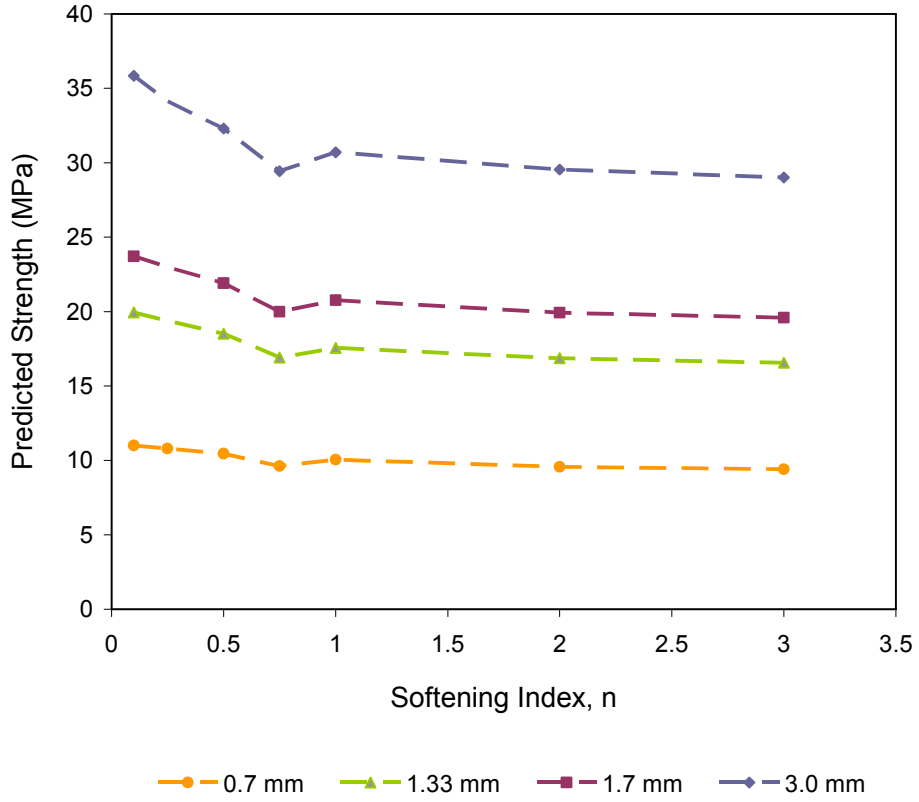

Figure 8-11: Variation in predicted strength for each panel thickness

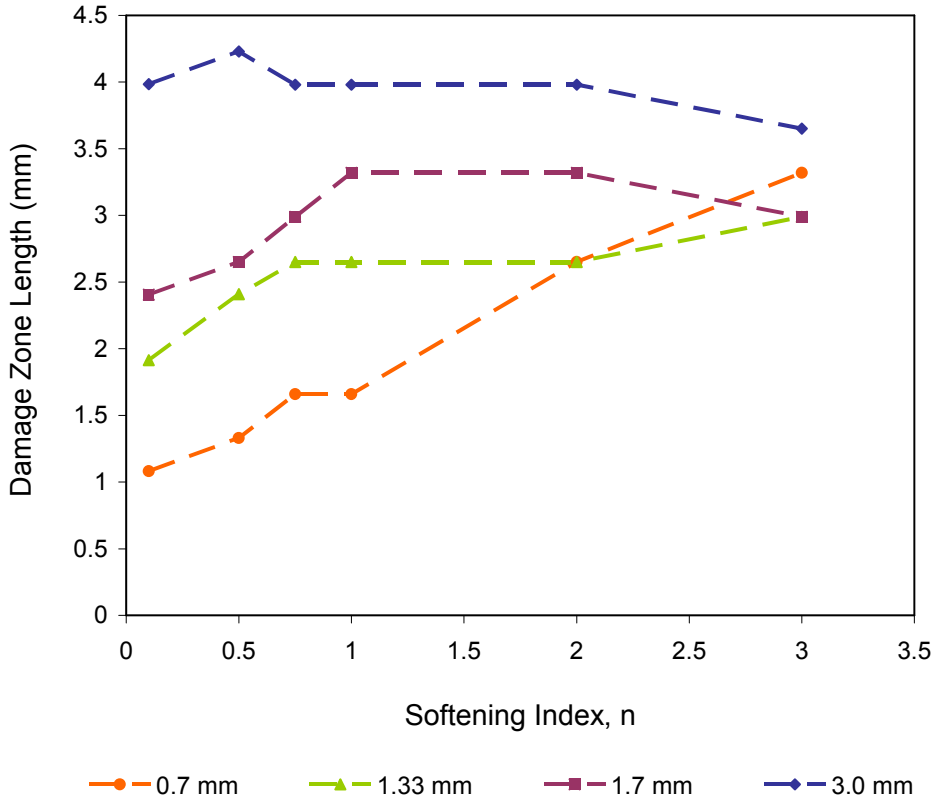

Figure 8-12: Variation in damage zone length for each panel thickness

From the different damage evolution profiles shown in Figure 8-4, the displacement at failure increases with *n* although the ability for the cohesive element to carry load decreases rapidly. This explains the longer damage zone for n ≥ 1 since the material allows the elements at the edge to degrade rapidly and yet not fail. On the other hand, as *n* approaches zero (displaying more elastic-perfectly plastic behaviour), the cohesive element is able to sustain

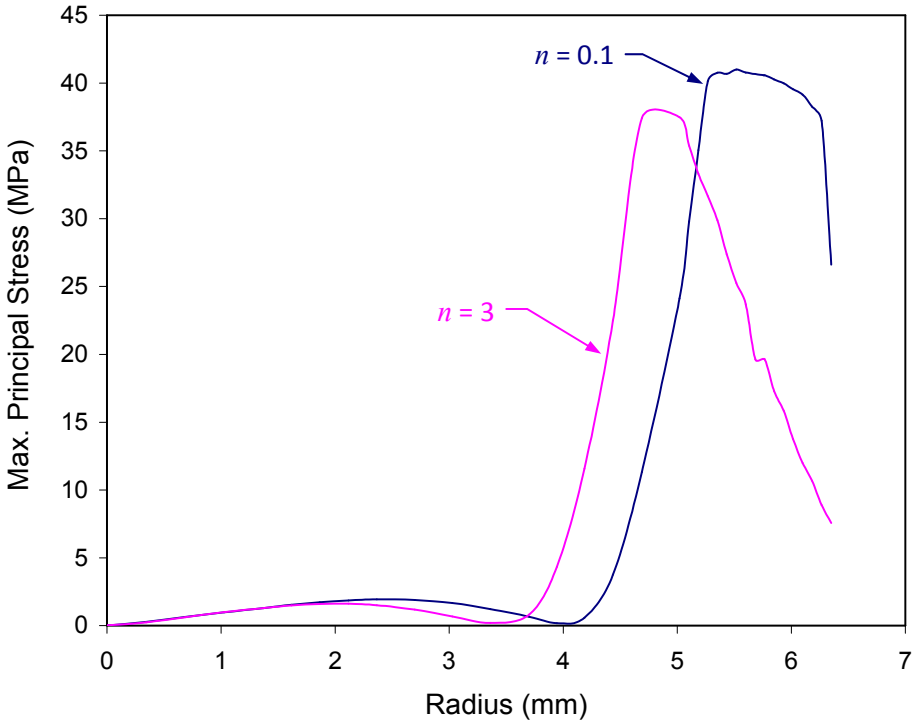

Figure 8-13: Comparison of stress gradient across the radius of cohesive elements with $n = 0.1$ and $n = 3$ for the 0.7 mm model

a higher percentage of its fracture load before it ruptures suddenly. As such, the damage zone for $n = 0.1$ was the smallest because the highly stressed elements at the radial edge of the adhesive are now able to withstand the loading upon them and do not need to distribute to as many elements at the edge. The load carrying ability of the elements for the two extreme cases of *n* is shown in Figure 8-13.

The stresses in the 0.7 mm model concentrate towards the edge of the adhesive while the centre region is hardly stressed. This stress gradient is caused by the flexing of the thinner panel which lowers the stresses in the centre region. The difference in the peak stress values is

the effect of the different mixed-mode loading on the panel. The change in mode-mixity is caused by the effect of *n* on the flexure of the panel.

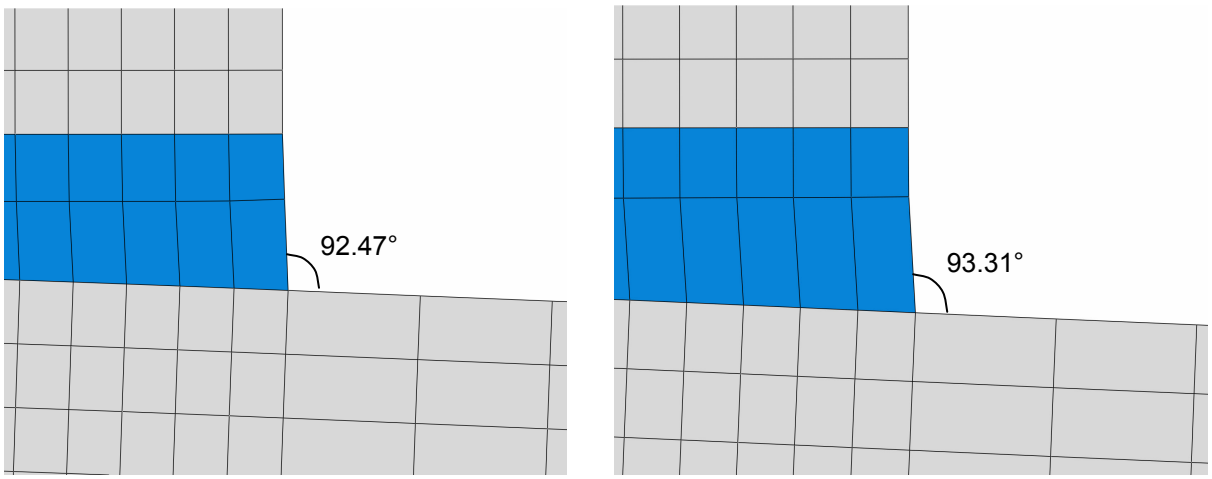

(a) (b)

Figure 8-14: Effects of a) $n = 0.1$ and b) $n = 3$ on the flexure of the 0.7 mm panel

The flexural deformation of the panel increases when the cohesive elements are specified with $n = 0.1$. When the cohesive elements are able to sustain load without significant deformation, higher load is transferred to flex the underlying panel and increase its deflection as shown in Figure 8-14a. In comparison, cohesive elements with $n = 3$ lose their strength rapidly and undergo large deformations which allows them to be stretched between the adherends as shown in Figure 8-14b. This results in lower load being transferred to the underlying panel.

The relative ease of softening for the $n = 3$ elements enables them to experience more Mode II shearing load compared to cohesive elements specified with $n = 0.1$. Consequently, the adhesive layers specified with the $n = 3$ evolution profile have a lower peak stress because they undergo a larger mode-mixity compared to the adhesive specified with $n = 0.1$ profile as shown in Figure 8-13.

Unlike the thinner panel, the central region of the 3.0 mm model is stressed due to the inability of the underlying panel to flex. This is shown in Figure 8-15 where the stresses

before the damage zone length do not reduce to zero. The positions of the peak stress for both cases of n = 0.1 and n = 3 are almost similar as previously shown in Figure 8-12. Due to higher bending stiffness of the thicker panel, the nature of the cohesive elements defined through n has little effect on the flexure of the panel. The angles formed between the deformed adhesive elements with the flexing adherend elements are now 91.64° for n = 0.1 and 91.52° for n = 3. As such, the mode-mixity in both cases of n remains similar.

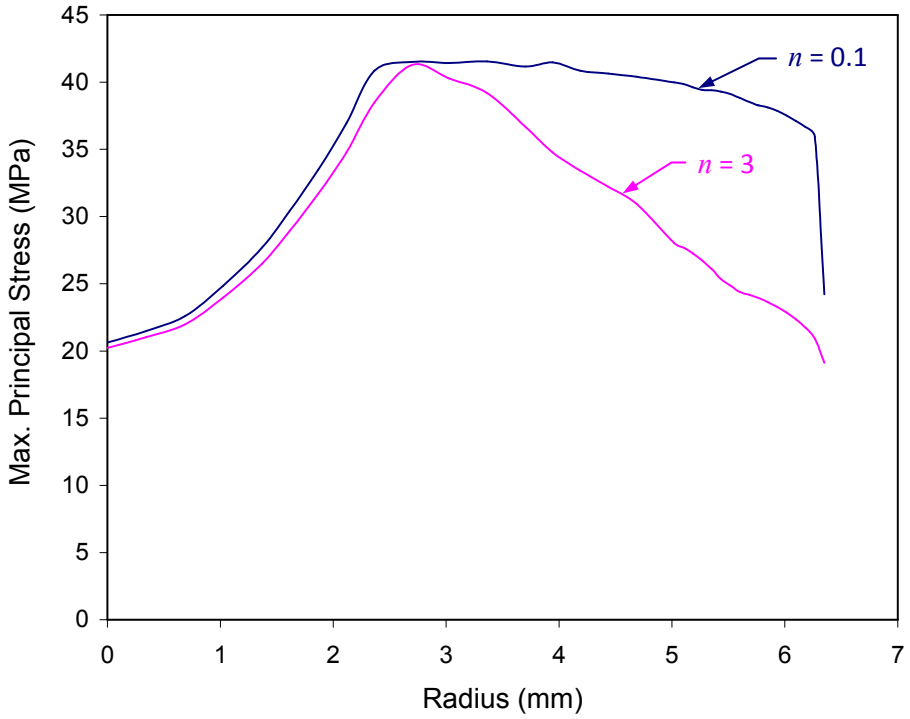

Figure 8-15: Comparison of stress gradient across the radius of cohesive elements with n = 0.1 and 3 for the 3.0 mm model

In conclusion, the best predictions were resulted when the cohesive elements were modelled with n = 0.1.The strengths predicted by these cohesive models only differed by 12% from the experimental data. The stress distributions across the adhesive are shown in Figure 8-16 and the damage zone lengths correspond to those presented in Figure 8-12 for n = 0.1.

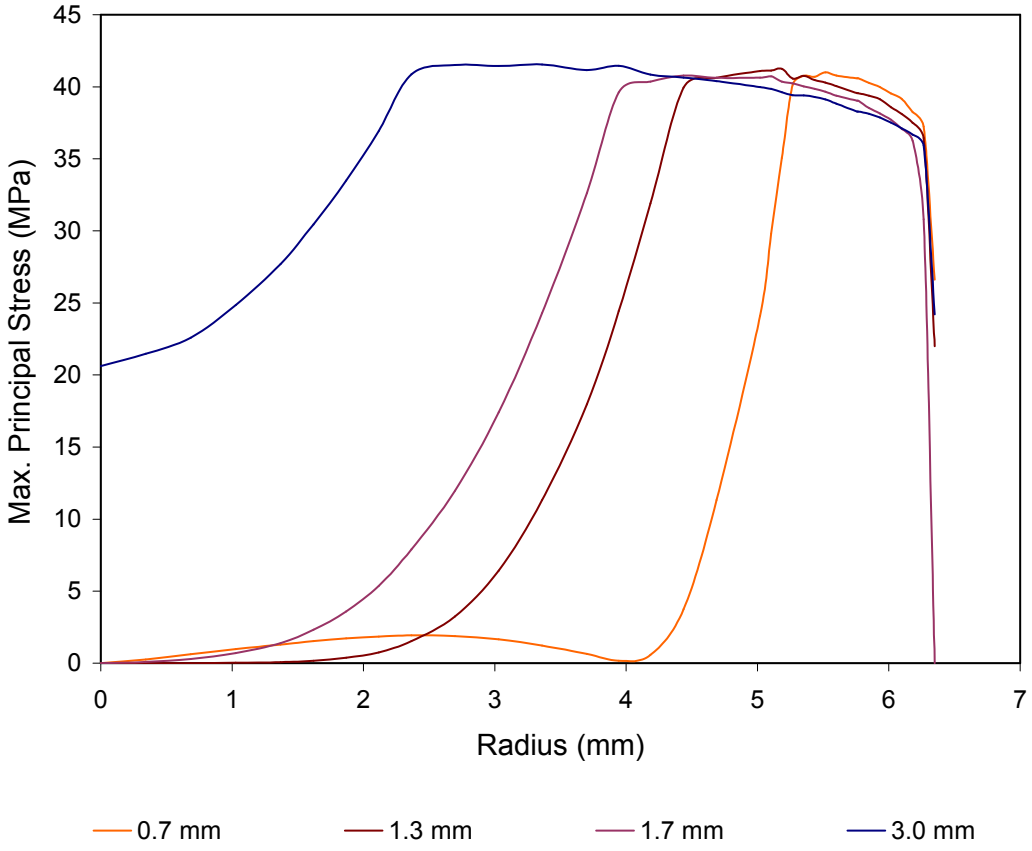

Figure 8-16: Maximum principal stress distribution across the adhesive when modelled with cohesive elements (n = 0.1)

9 Discussion

9.1 Predicting Pull-Strength for Panels with Non-Optimum Bond

In practice, it is not be possible to quantify all the field practices and service conditions that could affect the strength of bonded repairs. This means that it is not practical to generate individual linear Drücker-Prager curves for every conceivable surface preparation method and environmental condition representative of those field conditions that could have affected the strength of the bond. However, from the good correlation between the predictions in Section 7.3.3 and the experimental pull-off strength of panels prepared with one specific surface preparation method, the predictive model provides a means to quantify potential bond strength degradation. This is can be achieved by comparing pull-off strengths with predicted strengths using degraded properties (following environmental conditioning) pertinent to surface treatment methods. For example, if the measured pull-off strength is equal to the predicted strength of standard surface treatment, it can be concluded that correct surface preparation has been applied to install that repair. If the pull-off strengths are lower than the predictions, strength degradation has occurred, and the level of degradation can be determined by comparing the experimental value with predictions pertinent to a certain surface treatment.

By predicting the panel pull-off strength with different yield envelopes, a schematic strength threshold chart as shown in Figure 9-1 could be generated to allow the approximate surface preparation technique and the level of bond degradation to be established. For example, when the pull-strength of an actual PATTI test falls within the yellow or the blue-hashed region, it can be assumed that the bond was prepared with proper surface preparation

technique and has not suffered significant bond degradation. Subsequently, the shear strength of the panel can be inferred from the relevant linear Drücker-Prager curve (corresponding to the properties of the adhesive used to generate the strength threshold) when the hydrostatic pressure component is zero.

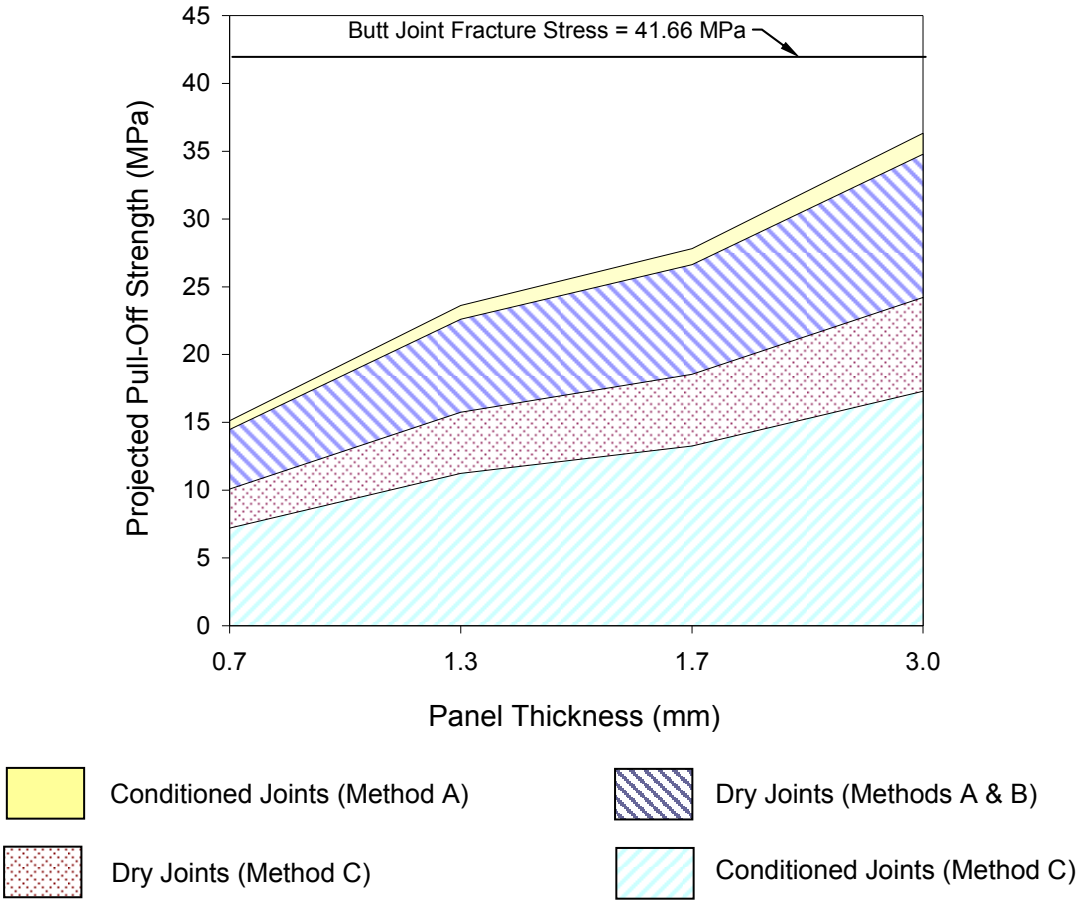

Figure 9-1: Strength threshold for generated from the yield envelopes of joints with different surface preparation methods and environmental conditioning

In reference [75], predictions made using the property for surface preparation Method A were found to correlate well the experimental results from panels prepared using method B. New predictions in Chapter 7, which have been carried out using properties for surface preparation method B, are also in good agreement with the experimental results. There is a little noticeable difference between predictions using properties from surface preparation methods A and B. From this, it is reasonable to expect that predictions based on properties

corresponding to surface preparation method C will correlate with pull-off strength of panels prepared using this same surface treatment method. Further research is required to substantiate this postulation.

For future work, additional pull-off tests on bonded panel prepared to Method C, either dry or after subjecting to similar hot-wet environmental conditioning could be performed to validate this postulation. If the bonded panel are to be subjected to hot-wet environmental conditioning, the circular grooves as shown in Figure 1-1b should be created before the panel is subjected to the environmental conditioning as this will allows moisture ingress into the adhesive underneath the test-disc at a similar rate to the conditioned scarf and lap-shear joints.

9.2 Generating Interfacial Fracture Modes

One of the aims of this research is to generate three types of fracture modes to investigate their effect on the fracture strength of the joints bonded with the FM300 adhesive. While it is known that the strength of joints failing through interfacial failure could range from a very small value (close to zero) to a large value (exceeding the cohesive strength of the adhesive; otherwise all joints would fail at the interface), it was of interest to quantify the interfacial strength as this would allow the additional behaviour at the interface to be represented in the FE models.

For example, if the behaviour of a poor interface is included into the adhesive section that has been described by the constitutive behaviour of the adhesive, the predicted pull-off strength for the 0.7 mm panel could be even lower because failure could then occur at the interface instead of the highly strained adhesive layer adjacent to the interface. This method of prediction would still require prior knowledge of the surface preparation method used on the bonding surfaces or the degree of degradation the interface had undergone; although it would then allow the two distinct features of the bond to be individually modelled through the

constitutive properties of the adhesive and the adhesion strength of the joint instead of using the yield envelopes to represent the general behaviour of the bond.

So far, the scarf and lap-shear experiments had generated pure cohesive and mixed cohesive-interfacial failure, but no pure interfacial failure. The appearance of interfacial failure in pull-tests on thin panel sections might actually be due to failure close to the adhesive-adherend interface within the adhesive layer so they were treated as cohesive failure when inferring the shear strength of the bond. This knowledge makes it possible for future work to measure the interfacial fracture strength of adhesive bonds by performing pull-tests on thin panels. The bonding surfaces of the thin panel could be prepared to different surface preparation techniques to measure the how the various preparation techniques affect the interfacial strength. Alternatively, the bonded stub and thin panel could be subjected to environmental conditioning to understand how different levels of bond degradation affect the interfacial strength.

9.3 Comparison between using the Cap Plasticity material and the Cohesive Models

The panel strengths predicted from using cohesive elements (n = 0.1) are plotted along with the experimental data and the predictions by the cap plasticity material model for comparison in Figure 9-2. The best predictions by the cohesive models were produced when the elements were modelled to behave closely to an elastic-perfectly plastic material. The predicted strengths by these cohesive models are also 12% difference from the prediction by the cap plasticity material. While varying the softening index n of the cohesive elements do affect the prediction, it does not capture the increase in strength for the 1.7 mm panel as the modified Drücker-Prager/cap plasticity material. The cap plasticity models capture the change in the strength gradient at the 1.33 mm thickness. This difference is suspected to be caused by

the inability of the current cohesive models to capture hydrostatic-sensitivity of the FM300 adhesive.

The FM300 adhesive was assumed to fail upon yielding according to the linear Drücker-Prager criterion described in Chapter 6.2. It should be noted that this '*yielding*' corresponds to the fracture strength of the material instead of the end of the linear elastic region. The linear Drücker-Prager criterion reflects the mode-mixity of the applied loading through the angle of friction for the material, $\tan\beta$. The tensile yield point of the cap

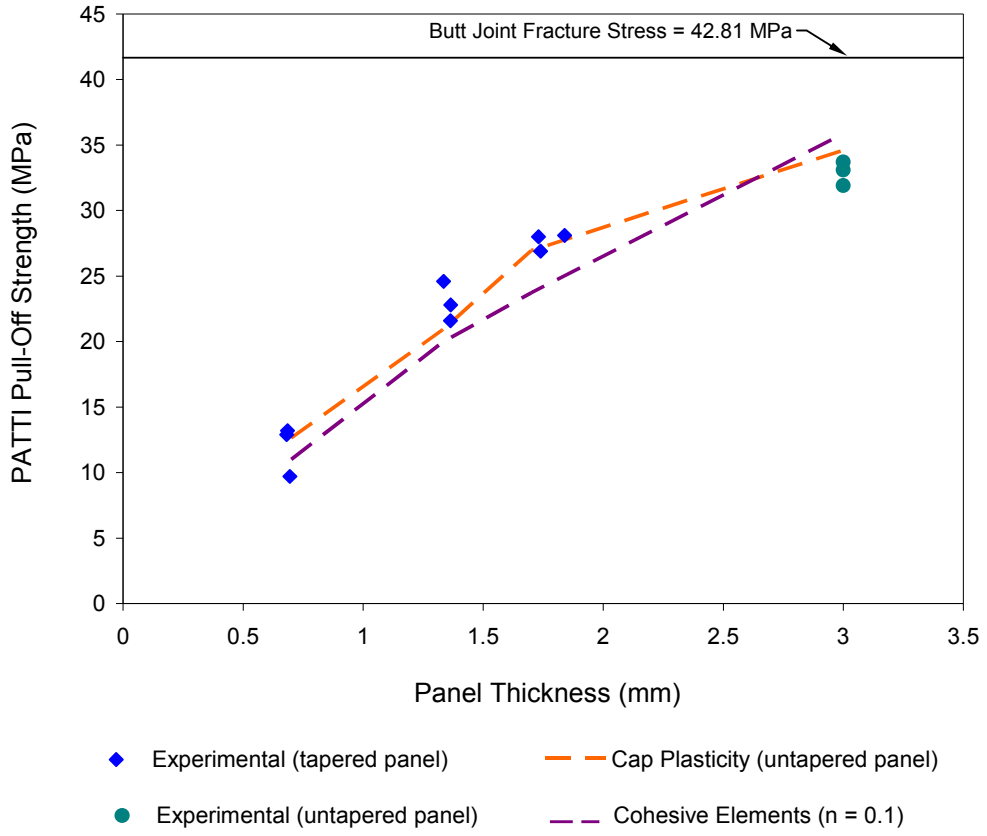

Figure 9-2: Comparison between the prediction by the modified Drücker-Prager/cap plasticity material and cohesive elements

plasticity material corresponds to the maximum traction value at damage initiation in the cohesive models. The cohesive models reflect the mode-mixity of the applied loading at damage initiation through the quadratic stress criterion given in Equation 8-6. However, this stress criterion does not capture the hydrostatic-sensitivity of the adhesive. It is hypothesized

that expressing the mode-mixity of the maximum traction as the linear Drücker-Prager criterion might account for this difference.

The characteristic length calibrated for the cap plasticity material does not relate to the damage zone length of the cohesive models. However, the stress distribution (expressed through the maximum principal stress) across the damage zone lengths of the cohesive models are quite similar to the stress distributions when the adhesive was modelled with the cap plasticity material as shown in Figure 9-3.

The formulation for the cohesive elements does not allow them to capture the compressive response of the material to avoid interpenetration of the cracked surfaces. This causes the maximum principal stresses from the adhesive layers of the cohesive models to

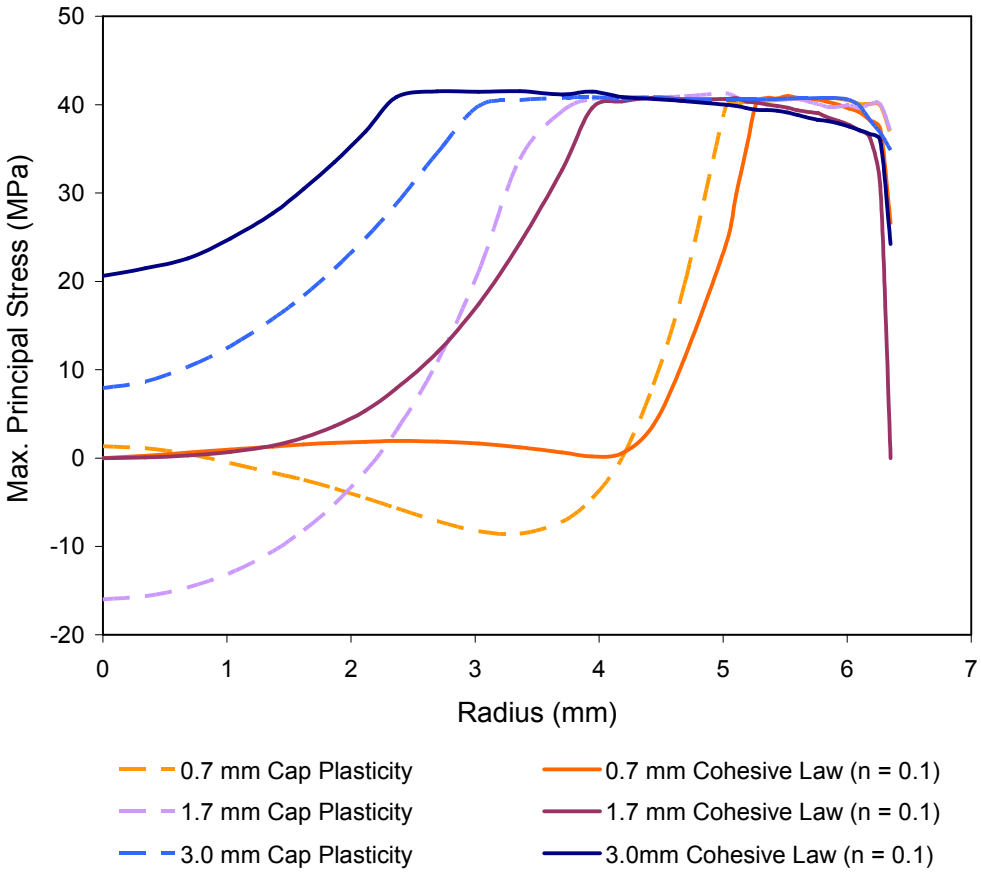

Figure 9-3: Comparison of stress distribution across the damage zone lengths of the cohesive models with $n = 0.1$ and across the adhesive when modelled by the cap plasticity material

exist within the tensile region only. As a result, the cohesive models are unable to capture the compressive stresses generated within the adhesive like the cap plasticity material.

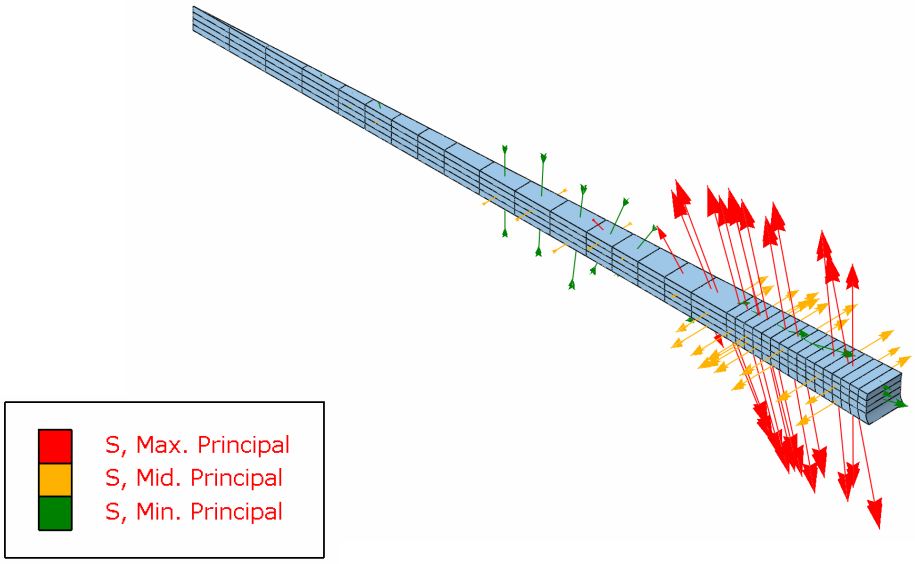

(a)

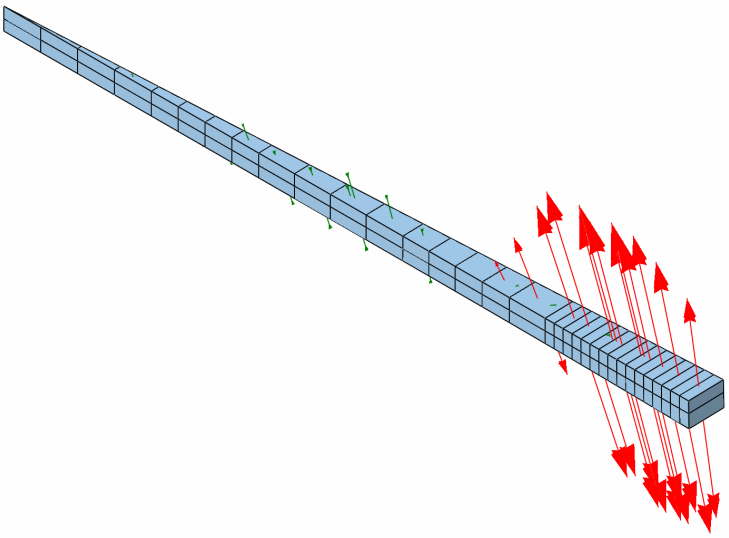

(b)

Figure 9-4: Vectors of the principal stresses within the adhesive layers of the 0.7 mm uniform panel model with a) cap plasticity material and b) cohesive model with $n = 0.1$

The cap plasticity material shows that compressive stresses are generated towards the central region of the adhesive due to the flexing of the underlying panel as shown in Figure

9-4a. These compressive stresses are reflected as shearing stresses in the cohesive model of n = 0.1 as shown in Figure 9-4b. The cap plasticity material also captures the hoop stresses at the edges caused by Poisson's effect which is not accounted by the cohesive model.

However, the predicted strength of the models is namely dominated by the maximum principal stresses. In both models, the maximum principal stresses are the same and concentrate at the edges. As such, cohesive elements can be used to model the adhesive layers of these FE panels if they are made to behave closely to an elastic-perfectly plastic material.

10 Conclusion

The following points were concluded from the work of this research:

1. The plastic yielding behavior of FM300 adhesive exhibits a strong sensitivity to hydrostatic pressure, which can be described by the linear Drücker-Prager yield criterion.
2. The pressure sensitivity increases with the level of interfacial failure. When subjected to environmental conditioning (hot/wet condition), joints prepared without γ-organosilane have been found to have a greater sensitive to hydrostatic pressure, with the yield curve having a steeper slope.
3. The shear strength of the joints can be inferred from the y-intercept of the yield curves (i.e. when the hydrostatic pressure is zero). The yield envelopes generated from different surface treatments and environmental degradation show that the shear strength of joints bonded with the FM300 adhesive are not as susceptible to the effects of surface treatment and environmental degradation as the tensile strength. This is reflected through the hydrostatic pressure sensitivity of the joints. Consequently a low pull-off strength does not necessarily imply that the joint has a low shear strength.
4. The use of the cap plasticity material in conjunction with the maximum principal strain failure criterion at a characteristic distance gives accurate prediction for the strength of joints and PATTI pull-off tests.
5. The shape of the cohesive law affects the predicted strength of PATTI pull-off tests. With a non-softening cohesive law (stress-strain curve is similar to elastic-perfectly plastic), the computational model produces the best correlation with the experimental results.

6. The angle of off-normal loading affects the pull-off strengths of the PATTI tests. This behaviour of the adhesive was captured by the cap plasticity material, which predicts a similar trend in strength reduction with the initial increase of scarf angles. The reduction in pull-off strength due to this phenomenon should not be mistaken for a deficiency in bond durability. An empirical method has been proposed to determine the shear strength of a joint subjected to off-normal loading.

7. The thickness of adherend over which the PATTI pull-tests are performed have been found to significantly affect the strength values and fracture modes of the bond. Due to the reduced flexural rigidity of thin panels, the PATTI pull-off strength decreases as adherend thickness decreases.

8. The two predictive models, a strain-based failure and a cohesive element approach, have been developed and validated against the experimental results. These models can quantify the effect of adherent thickness and taper on the PATTI pull-off strengths.

References

[1] Regulations F.A., Damage tolerance and fatigue evaluation of structure, FAR Part 23.573, 2013.

[2] Baker A.A., A Proposed Approach for Certification of Bonded Composite Repairs to Flight-Critical Airframe Structure, Applied Composite Materials, (2010) 1-33.

[3] Baker A., Structural Health Monitoring of a Bonded Composite Patch Repair on a Fatigue-Cracked F-111C Wing, Defence Science and Technology Organisation, Fishermans Bend, Victoria, 2008.

[4] Wang C.H., Gunnion A.J., Orifici A.C., Rider A., Residual strength of composite laminates containing scarfed and straight-sided holes, Composites Part A: Applied Science and Manufacturing, 42 (2011) 1951-61.

[5] McBroom G.P., Method of forming and indirect testing of a bond of or in an aircraft component, United States Patent, Airbus Operations Limited, Bristol (GB), United States, 2010.

[6] Baker A., Britton D., Wang J., Development of a proof test for through-life monitoring of bond integrity in adhesive bonded repairs to aircraft structure, Intl. J. Adhesion & Adhesives, 36 (2012) 65 - 76.

[7] Callus P.J., Chang P., Dellios D., Nicholson K.J., Rider A., Stoyanovski I., et al., F-111 Adhesive Bonded Repair Assessment Program (FABRAP) - Phase I Testing, Preliminary Results, Defence Science and Technology Organisation, Fishermans Bend, Victoria, 2011.

[8] ASTM, ASTM D4541 - 09e1 Standard Test Method for Pull-Off Strength of Coatings Using Portable Adhesion Testers, Adhesives, American Society for Testing and Materials, 2010.

[9] FM 73 Epoxy Film Adhesive - Technical Data Sheet, www.cytec.com, Cytec Engineering Materials, 2011.

[10] Adams R.D., Coppendale J., Peppiatt N.A., Stress Analysis of Axisymmetric Butt Joints Loaded in Torsion and Tension, Journal of Strain Analysis for Engineering Design, 13 (1978) 1-10.

[11] Alwar R.S., Nagaraja Y.R., Elastic Analysis of Adhesive Butt Joints, Journal of Adhesion, 7 (1976) 279-87.

[12] Öchsner A., Gracio J., An evaluation of the elastic properties of an adhesive layer using the tensile-butt-joint test: Procedures and error estimates, Intl. J. Adhesion & Adhesives, 27 (2007) 129 - 35.

[13] Wang C.H., Chalkley P., Plastic yielding of a film adhesive under multiaxial stresses, International Journal of Adhesion and Adhesives, 20 (2000) 155 - 64.

[14] Lesser A.J., Kody R.S., Crawford E.D., Yield Envelopes of Micro-Voided Epoxies, in: Pearson R.A., Sue H.-J., Yee A.F. (Eds.), Toughening of Plastics, American Chemical Society, 2000, pp. 159 - 70.

[15] Rider A.N., Olsson-Jacques C.L., Arnott D.R., Influence of adherend surface preparation on bond durability, Surf. Interface Anal., 27 (1999) 1055 - 63

[16] Rider A.N., Surface treatments for field level bonded repairs to Aluminium and Titanium structure, Defence Science and Technology Organisation, Fishermans Bend, Victoria, 2008.

[17] Sawa T., Temma K., Ishikawa H., Three-dimensional stress analysis of adhesive butt joints of solid cylinders subjected to external tensile loads, J. of Adhesion, 31 (1989) 33-43.

[18] Buchman A., Weinstein F., Hönigsberg I., Holdengraber Y., Dodiuk H., Stress analysis and testing of parallel and tapered adhesive butt joints, Journal of Adhesion Science and Technology, 7 (1993) 385-97.

[19] Bonk R.B., Ostendorf J.F., Pettenger B.L., Ambrosio A.M., Methods for evaluation adhesive systems and adhesion, U.S. Army Armament Research, Development and Engineering Center, Picatinny Arsenal, New Jersey, 1996.

[20] Hart-Smith L.J., Adhesive-bonded single-lap joints, National Aeronautics and Space Administration, Hampton, Virginia, 1973.

[21] Cooper P.A., Sawyer J.W., A critical examination of stresses in an elastic single lap joint, National Aeronautics and Space Administration, Hampton, Virginia, 1979.

[22] ASTM, ASTM D5656 - 10 Standard Test Method for Thick-Adherend Metal Lap-Shear Joints for Determination of the Stress-Strain Behavior of Adhesives in Shear by Tension Loading, American Society for Testing and Materials, 2010.

[23] ASTM, ASTM D1002 Standard Test Method for Apparent Shear Strength of Single-Lap-Joint Adhesively Bonded Metal Specimens by Tension Loading (Metal-to-Metal), Adhesives, ASTM, 2005.

[24] Adams R.D., Comyn J., Wake W.C., Structural Adhesive Joints in Engineering, 2nd ed., Chapman & Hall, 1997.

[25] Wang C.H., Fracture of Interface Cracks Under Combined Loading, Engineering Fracture Mechanics, 56 (1997) 77 - 86.

[26] Liechti K.M., Freda T., On the Use of Laminated Beams for the Determination of Pure and Mixed-Mode Fracture Properties of Structural Adhesives, The Journal of Adhesion, 28 (1989) 145-69.

[27] ABAQUS, Modified Drucker-Prager/Cap model, Abaqus 6.10 Documentation - Analysis User's Manual, 2012.

[28] Brewis D.M., J. C., Cope B.C., Moloney A.C., Effect of carriers on the performance of aluminium alloy joints bonded with an epoxide-polyamide adhesive, Polymer, 21 (1980) 344-51.

[29] Pearce P.J., Arnott D.R., Camilleri A., Kindermann M.R., Mathys G.I., Wilson A.R., Cause and effect of void formation during vacuum bag curing of epoxy film adhesives, J. Adh. Sci. Tech., 12 (1998) 567 - 84.

[30] Arnott D.R., Pearce P.J., Wilson A.R., Chester R.J., Camilleri A., Berg J.V.D., The effect on mechanical properties of void formation during vacuum bag processing of epoxy film adhesives, PICAST 2 - AAC 6, Melbourne, 1995, pp. 811 - 6.

[31] Chester R.J., Roberts J.D., Void Minimization in Adhesive Joints, International Journal of Adhesion and Adhesives, 9 (1989) 129 - 38.

[32] Rider A.N., Arnott D.R., Wilson A.R., Vargas O., Influence of simple surface treatments on the durability of bonded aluminium alloy plates, Material Science Forum, 189 - 190 (1995) 235 - 40.

[33] Liljedahl C.D.M., Crocrombe A.D., Wahab M.A., Ashcroft I.A., Modelling the environmental degradation of the interface in adhesively bonded joints using a cohesive zone approach, J. Adhesion, 82 (2006) 1061 - 89.

[34] LaPlante G., Lee-Sullivan P., Moisture effects on FM300 structural film adhesive: Stress relaxation, fracture toughness, and dynamic mechanical analysis, Journal of Applied Polymer Science, 95 (2005) 1285-94.

[35] Lin Y.C., Chen X., Moisture sorption-desorption-resorption characteristics and its effect on the mechanical behaviour of the epoxy system, Polymer, 46 (2005) 11994 - 2003.

[36] Rider A., The Durability of Metal-Honeycomb Sandwich Structure Exposed to High Humidity Conditions, Defence Science and Technology Organisation, 2002.

[37] Zhou J., Lucas J.P., The effects of a water environment on anomalous absorption behaviour in graphite/epoxy composites, Composites Sci. & Tech. , 53 (1995) 57 - 64.

[38] Vanlandingham M.R., Eduljee R.F., Gillespie J.W., Moisture Diffusion in Epoxy System, J. Applied Polymer Sci., 71 (1999) 787 - 98.

[39] Adamson M.J., Thermal expansion and swelling of cured epoxy resin used in graphite/eposy composite materials, J. of Mat. Sci., 15 (1980) 1736 - 45.

[40] Loh W.K., Crocombe A.D., Wahab M.M.A., Ashcroft I.A., Modelling interfacial degradation using interfacial rupture elements, J. of Adhesion, 79 (2003) 1135 - 60.

[41] Shirangi M.H., Fan X.J., Michel B., Mechanism of moisture diffusion, hygroscopic swelling and adhesion degradation in epoxy mold compounds, Intl. Symp. on Microelectronics, 41 (2008) 1082 - 9.

[42] Weitsman Y., Moisture in Composites: Sorption and Damage, in: Reifsnider K.L. (Ed.), Fatigue of composite materials, Elsevier, 1991, Amsterdam; New York, , 1990, pp. 385 - 429.

[43] Rider A.N., Arnott D.R., Durability of bonds formed between epoxy adhesive and aluminium alloy treated with phosphonate inhibitors, Surface & Interface Anal., 24 (1996) 583 - 90.

[44] Hohman A.E., Standard C.M., Durability of Adhesive Bonded Structure, LTV Aerospace & Defense Company, Dallas, Texas, 1992.

[45] Placette M.D., Fan X., Zhao J.H., Edwards D., A Dual Stage Model of Anomalous Moisture Diffusion and Desorption in Epoxy Mold Compounds, 12th. Intl. Conf. on Therm, Mech. & Multiphysics Sim. and Exp. in Microelectronics & Microsystems, 2011, pp. 1 - 8.

[46] Loh W.K., Crocombe A.D., Wahab M.M.A., Ashcroft I.A., Modelling anomalous moisture uptake, swelling and thermal characteristics of a rubber toughened epoxy adhesive, Intl. J. Adhesion & Adhesives, 25 (2005) 1 - 12.

[47] Mubashar A., Ashcroft I.A., Critchlow G.W., Crocombe A.D., Moisture absorption-desorption effects in addhesive joints, Intl. J. Adhesion & Adhesives, 29 (2009) 751 - 60.

[48] Brewis D.M., J. C., Moloney A.C., J.L. T., The use of isotopically labelled water to monitor the ingress of water into adhesive joints, EU Polymer J., 17 (1980) 127-30.

[49] Broughton W.R., Crocker L.E., Urquhart J.M., Strength of Adhesive Joints: A Parametric Study, NPL Materials Centre, Teddington, Middlesex, UK, 2001.

[50] ABAQUS, Progressive Damage and Failure - Mesh Dependency, ABAQUS Documentation - Analysis User's Manual, 2012.

[51] Vogler M., Kolling S., Rolfes R., Transversely isotropic plasticity with application to fiber-reinforced plastics, DYNAmore GmbH, LS-DYNA Anwenderforum, Frankenthal 2007, 2007, pp. D-11-66.

[52] Foote R.M.L., Mai Y.-W., Cotterell B., Crack Growth Resistance Curves in Strain-Softening Materials, J. Mech. Phy. Solids, 34 (1986) 593 - 607.

[53] Brewer J.C., Lagace P.A., Quadratic stress criterion for initiation of delamination, J. of Composite Materials, 22 (1988) 1141 - 55.

[54] Camanho P.P., Davila C.G., Mixed-Mode Decohesion Finite Elements for the Simulation of Delamination in Composite Materials, National Aerounautics and Space Administration, 2002.

[55] Bowden P.B., Jukes J.A., The plastic flow of isotropic polymers, J. of Mat. Sci., 7 (1972) 52 - 63.

[56] FM300 High-Shear Strength Modified Epoxy Film Adhesive, in: Materials C.E. (Ed.), Havre de Grace.

[57] ASTM, ASTM D3433-99 Standard Test Method for Fracture Strength in Cleavage of Adhesives in Bonded Metal Joints, Adhesives, American Society for Testing and Materials, 1999.

[58] Rider A.N., Arnott D.R., Boiling water and silane pre-treatment of aluminium alloys for durable adhesive bonding, Intl. J. Adhesion & Adhesives, 20 (2000) 209 - 20.

[59] ASTM, ASTM D3762-03(2010) Standard Test Method for Adhesive Bonded Surface Durability of Aluminium (Wedge Test), Adhesives, American Society for Testing and Materials, 2010.

[60] Davies P., Protocols for Interlaminar Fracture Testing of Composites, European Structural Integrity Society Polymers & Composites Task Group, 1993.

[61] Kim M.K., Impact resistance of composite scarf joints under load, School of Aerospace, Mechanical and Manufacturing Engineering, RMIT University, Melbourne, 2010, p. 126.

[62] Allen K.W., Stevens M.G., The Structure of Films of Silane Primers on Aluminium Substrates, The Journal of Adhesion, 14 (1982) 137-44.

[63] Tenchev R.T., Falzon B.G., Experimental and numerical study of debonding in composite adhesive joints, 16th International Conference on Composite Materials, Kyoto, Japan, 2007.

[64] Kim M.K., Elder D.J., Wang C.H., Feih S., Interaction of laminate damage and adhesive disbonding in composite scarf joints subjected to combined in-plane loading and impact, Composite Structures, 94 (2012) 945 - 53.

[65] Dalsteel, Aluminium Alloy 6060 - T5~T595, 2011.

[66] ASM, Aluminum 2024-T3, Aerospace Specification Metals Inc. , 2001.

[67] ASM, Aluminum 7075-T6; 7075-T651, Aerospace Specification Metals Inc. , 2001.

[68] Lee C.C., Crosky A., Kelly D., Determination of the Mechanical Properties of Adhesives for Use in Design of Bonded Joints in Composite Structures, ICCM-10, Whistler, B.C., Canada, 1995, pp. 511-8.

[69] Wang C.H., Gunnion A.J., On the design methodology of scarf repairs to composite laminates, Composites Science and Technology, 68 (2008) 35-46.

[70] Hysol EA 9309.3NA Epoxy Paste Adhesive, in: Group H.C.A. (Ed.), Bay Point, CA, USA.

[71] ABAQUS, Mises Yield Surfaces, Metal Plasticity - Classical Metal Plasticity, Abaqus Analysis User's Manual, 2012.

[72] Wang C.H., Rose L.R.F., Compact solutions for the corner singularity in bonded lap joints, International Journal of Adhesion and Adhesives, 20 (2000) 145-54.

[73] Karachalios E.F., Adams R.D., Silva L.F.M.d., Single lap joints loaded in tension with high strength steel adherends, International Journal of Adhesion and Adhesives, 43 (2013) 81-95.

[74] ABAQUS, Defining the constitutive response of cohesive elements using a traction-separation description, Cohesive elements, ABAQUS Analysis User's Manual, 2012.

[75] Lee M., Wang C.H., Yeo E., Janardhana M., Effects of Adherend Thickness on the Bond Strength Measurement of Adhesive Bonded Repairs, in: Kotousov A. (Ed.), 7th Australasian Congress on Applied Mechanics, Adelaide, 2012.

Appendix I – DSTO Gritblast Silane Process for Aluminium Substrates

1) Solvent degrease the bonding surfaces
    a) Using (lanolin and lint free) tissues wetted with MEK, wipe unidirectionally, first in 0° direction, then 90° direction
    b) Scotchbrite abrade using MEK (in 0° then 90° directions)
    c) Wipe clean using solvent-wetted tissues
    d) Scotchbrite abrade using distilled/deionised water
    e) Clean with distilled/deionised water-wetted tissues
    f) Perform water break test – thoroughly wet the surface by spraying/squirting, using distilled/deionised water. Observe if water breaks from the surface in any region – if so, this indicates contaminants on the surface. Dry using a hot air gun, again observing for water break regions.
    g) Dry in an oven at 110°C for 5 minutes.
2) Grit blast with 50 μm aluminium oxide grit, using 350 kPa dry nitrogen
3) Apply silane solution to bonding surfaces.
    a) Prepare organo-silane coupling agent (1 vol% γ-glycidoxypropyl-trimethoxysilane (γ-GPS) in distilled/deionised water). Stir for at least 1 hour before use.
    b) Apply solution for 10-15 minutes, taking care not to allow the surface to dry (air drying tends to deposit a silane layer that is too thick). Typical application methods include dipping (for small parts) or brushing with soaked tissues.
    c) Remove excess solution (a heat gun can be used), dry in an oven at 110°C for 1 hour
    d) Upon removal from oven, allow to cool, then proceed with adhesive bonding process without delay (contaminants in the air will deposit on your cleaned, chemically active surface).

Bonding Notes: Ensure adhesive is fully thawed before opening packet, otherwise moisture from air will condense on the adhesive. A single-sheet packet of film adhesive requires roughly 1 hour to thaw.

Appendix II – Alternative Surface Preparation Techniques for Aluminium Substrates (Methods B and C)

Method B

1) Solvent degrease the bonding surfaces

   <Refer to Step 1 (a) to (g) of Appendix I>

2) Abrade bonding surfaces with 180 grit alumina paper, first in 0° direction, then 90° direction.

3) Clean with distilled/deionised water-wetted tissues.

4) Apply silane solution to bonding surfaces.

   <Refer to Step 3 (a) to (d) of Appendix I>

Method C

1) Solvent degrease the bonding surfaces.

   a) Using (lanolin and lint free) tissues wetted with MEK, wipe unidirectionally, first in 0° direction and then 90° direction.

   b) Clean with distilled/deionised water-wetted tissues (in 0° then 90° directions).

   c) Perform water break test – thoroughly wet the surface by spraying/squirting, using distilled/deionised water. Observe if water breaks from the surface in any region – if so, this indicates contaminants on the surface. Dry using a hot air gun, again observing for water break regions.

2) Abrade bonding surfaces with 180 grit alumina paper, first in 0° direction and then 90° direction.

3) Clean with distilled/deionised water-wetted tissues.

4) Dry in an oven at 110°C for 5 minutes.

Appendix III – Curing Procedures for Bonded Joints

1) Place vacuum-bagged specimens into oven at room temperature.
2) Attach vacuum line to vacuum bag and decrease pressure in vacuum bag to 68 kPa or more.
3) Increase oven temperature at of 3°C / min ramp rate.
4) When oven temperature reaches 80°C, increase pressure in vacuum bag to 34 kPa.
5) Continue to increase oven temperature to 177°C at of 3°C / min ramp rate.
6) When oven temperature reaches 177°C, maintain temperature for 90 minutes.
7) Allow oven temperature to decrease below 80°C before moving specimens.

Appendix IV – Example of Tabular Data in ABAQUS CAE

The following table shows the typical format of data specified for the tabular softening and tabular mixed-mode functions in ABAQUS CAE. The data for $n = 3$ are shown below.

d_i	$\left(\delta_i^f - \delta_i^0\right)$	ϕ_1	ϕ_2
0	0	0	0
0.008684567	4.39255E-005	0	0
0.017369133	8.78511E-005	0	0
0.034264958	0.000175702	0	0
0.066710532	0.000351404	0	0
0.126683248	0.000702809	0	0
0.230053505	0.001405617	0	0
0.388196636	0.002811235	0	0
0.502997842	0.004216852	0	0
0.589675885	0.005622469	0	0
0.710714221	0.008433704	0	0
0.789896296	0.011244939	0	0
0.883830839	0.016867408	0	0
0.934284064	0.022489877	0	0
0.963145567	0.028112346	0	0
0.980041881	0.033734816	0	0
0.993041943	0.04216852	0	0
0.998243331	0.050602224	0	0
0.999808713	0.059035927	0	0
1	0.067469631	0	0
0	0	0.055555556	0
0.00881382	4.45214E-005	0.055555556	0
0.01762764	8.90428E-005	0.055555556	0
⋮	⋮	0.055555556	0
1	0.068384871	0.055555556	0
0	0	0.111111111	0
⋮	⋮	⋮	0
⋮	⋮	*<19-off ϕ_1 at equal*	0
⋮	⋮	*intervals in total>*	0
⋮	⋮	⋮	0
1	0.538118525	0.944444444	0
0	0	1	0
⋮	⋮	1	0
1	0.554858536	1	0

To be continued in the next page

d_i	$\left(\delta_i^f - \delta_i^0\right)$	ϕ_1	ϕ_2
0	0	0	0.2
0.008684567	4.39255E-005	0	0.2
0.017369133	8.78511E-005	0	0.2
0.034264958	0.000175702	0	0.2
0.066710532	0.000351404	0	0.2
0.126683248	0.000702809	0	0.2
0.230053505	0.001405617	0	0.2
0.388196636	0.002811235	0	0.2
0.502997842	0.004216852	0	0.2
0.589675885	0.005622469	0	0.2
0.710714221	0.008433704	0	0.2
0.789896296	0.011244939	0	0.2
0.883830839	0.016867408	0	0.2
0.934284064	0.022489877	0	0.2
0.963145567	0.028112346	0	0.2
0.980041881	0.033734816	0	0.2
0.993041943	0.04216852	0	0.2
0.998243331	0.050602224	0	0.2
0.999808713	0.059035927	0	0.2
1	0.067469631	0	0.2
0	0	0.055555556	0.2
0.00881382	4.45214E-005	0.055555556	0.2
0.01762764	8.90428E-005	0.055555556	0.2
0.034766174	0.000178086	0.055555556	0.2
⋮	⋮	⋮	0.2
⋮	*< Same values as ϕ_2 =0 >*	⋮	0.2
⋮	⋮	⋮	0.2
1	0.554858536	1	0.2
0	0	0	0.4
⋮	⋮	⋮	⋮
⋮	⋮	⋮	*<5-off ϕ_2 at equal intervals in total>*
⋮	⋮	⋮	⋮
1	0.554858536	1	0.8
0	0	0	1.0
⋮	⋮	⋮	⋮
1	0.554858536	1	1.0